

# Aspects of precision grinding : part roughness, form accuracy and a basic study of the brittle to ductile removal transition

**Citation for published version (APA):**

Franse, J. (1991). *Aspects of precision grinding : part roughness, form accuracy and a basic study of the brittle to ductile removal transition*. [Phd Thesis 1 (Research TU/e / Graduation TU/e), Mechanical Engineering]. Technische Universiteit Eindhoven. <https://doi.org/10.6100/IR355196>

**DOI:**

[10.6100/IR355196](https://doi.org/10.6100/IR355196)

**Document status and date:**

Published: 01/01/1991

**Document Version:**

Publisher's PDF, also known as Version of Record (includes final page, issue and volume numbers)

**Please check the document version of this publication:**

- A submitted manuscript is the version of the article upon submission and before peer-review. There can be important differences between the submitted version and the official published version of record. People interested in the research are advised to contact the author for the final version of the publication, or visit the DOI to the publisher's website.
- The final author version and the galley proof are versions of the publication after peer review.
- The final published version features the final layout of the paper including the volume, issue and page numbers.

[Link to publication](#)

**General rights**

Copyright and moral rights for the publications made accessible in the public portal are retained by the authors and/or other copyright owners and it is a condition of accessing publications that users recognise and abide by the legal requirements associated with these rights.

- Users may download and print one copy of any publication from the public portal for the purpose of private study or research.
- You may not further distribute the material or use it for any profit-making activity or commercial gain
- You may freely distribute the URL identifying the publication in the public portal.

If the publication is distributed under the terms of Article 25fa of the Dutch Copyright Act, indicated by the "Taverne" license above, please follow below link for the End User Agreement:

[www.tue.nl/taverne](http://www.tue.nl/taverne)

**Take down policy**

If you believe that this document breaches copyright please contact us at:

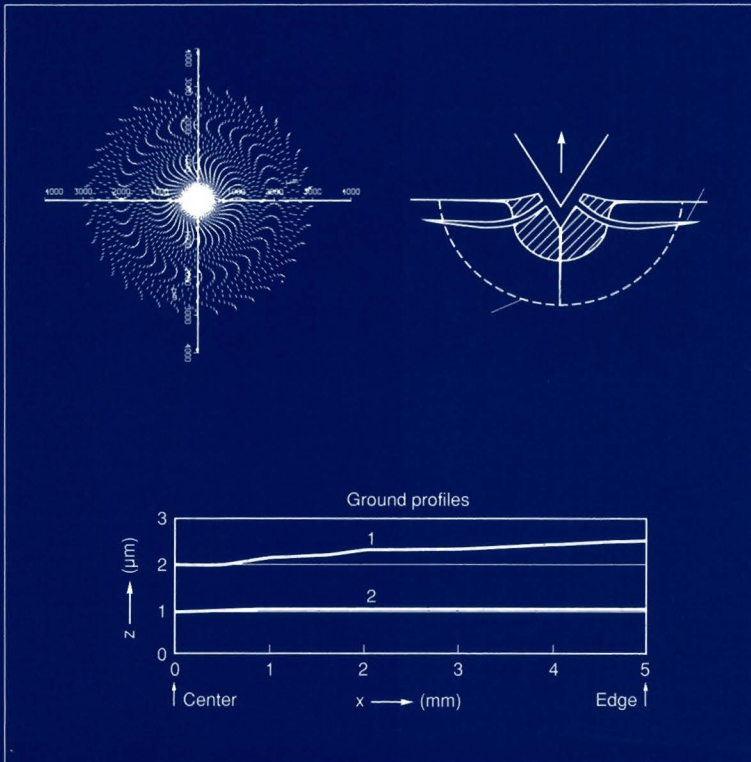
[openaccess@tue.nl](mailto:openaccess@tue.nl)

providing details and we will investigate your claim.

# Aspects of Precision Grinding

(Part roughness, form accuracy and a basic study  
of the brittle to ductile removal transition)

Jelm Franse



On the cover: A simulated roughness pattern (chapter 2), a crack pattern as observed in indentation tests (chapter 3) and profiles ground during the investigation of form accuracy in precision contour grinding (chapter 4).

The work described in this thesis has been carried out at the Philips Research Laboratories Eindhoven as part of the Philips programme.

# **Aspects of Precision Grinding**

**(Part roughness, form accuracy and a basic study of the brittle to ductile removal transition)**

**PROEFSCHRIFT**

ter verkrijging van de graad van doctor aan de  
Technische Universiteit Eindhoven, op gezag van de  
Rector Magnificus, prof. dr. J.H. van Lint, voor een  
commissie aangewezen door het College van Dekanen  
in het openbaar te verdedigen  
op vrijdag 5 juli 1991 te 16.00 uur

door

**Jelm Franse**  
geboren te Djakarta

Dit proefschrift is goedgekeurd door  
de promotoren

prof. dr. ir. E.A. Muijderman

en

prof. dr. ir. J.D. Janssen

Deze thesis wil ik opdragen  
Aan mijn ouders,  
die mij leerden naar reden en achtergronden te vragen.  
Aan Monique,  
die mij de ruimte gaf kennis na te blijven jagen,  
zonder haar steun had deze promotie nooit kunnen slagen.  
Aan Daphne,  
op wie ik wat van mijn nieuwsgierigheid hoop over te dragen.

Veldhoven, 26 maart 1991.

---

## Samenvatting

In hoofdstuk 1 wordt het slijpproces geïntroduceerd als een methode om complexe vormen te vervaardigen in materialen als staal, keramiek en glas, met sub-micron vormnauwkeurigheid en ruwheid in de orde van nanometers.

De slijpbewerking wordt beschreven als een systeem, bestaande uit de bewerkingsmachine en het slijpproces. Ingangsvariabelen van het systeem zijn de procesvariabelen. Uitgangsgrootheden zijn kwaliteitskenmerken van het bewerkte onderdeel zoals oppervlakteruwheid, vormnauwkeurigheid en integriteit van het bewerkte materiaal.

De aspecten van het machinegedrag en het slijpproces welke van belang zijn voor de bereikbare oppervlaktekwaliteit worden besproken en de bewerkingsmachines die voor slijpexperimenten zijn gebruikt worden beschreven.

In hoofdstuk 2 wordt onderzoek beschreven aangaande de invloed van de procesvariabelen op de ruwheid van geslepen oppervlakken (ruwheidsprofielen en patronen). Experimentele bevindingen komen goed overeen met de verwachtingen op basis van de theorie en een methode om het ontstaan van ruwheidspatronen tegen te gaan wordt aangegeven.

Het is al enige tijd bekend dat elk materiaal, ongeacht hoe bros, kan worden verspaand op een duktiele manier (zonder brosse scheurvorming), mits de verspaningscondities goed gekozen en beheerst worden. In hoofdstuk 3 worden de resultaten van een fundamentele studie gepresenteerd welke tot doel had na te gaan welke grootheden van belang zijn voor de overgang van het duktiele naar het brosse verspaningsregime. De resultaten van numerieke berekeningen worden vergeleken met indrukproeven op glas. Er wordt aangetoond dat een linear-elastisch breuk-mechanisch model bruikbaar is om de kritische belasting, waarbij scheurvorming optreedt, met redelijke nauwkeurigheid te voorspellen.

In hoofdstuk 4 worden de invloeden van dominante machine eigenschappen en procesvariabelen op de vormnauwkeurigheid bij het contourslijpen besproken. Een model wordt gepresenteerd waarmee voor gegeven machine eigenschappen en process parameters de haalbare vormnauwkeurigheid kan worden voorspeld. De theoretische uitkomsten stemmen goed overeen met experimentele resultaten.

De theorie geeft aan hoe de bewerkingsnauwkeurigheid kan worden verhoogd. Experimentele resultaten tonen de effectiviteit van de voorgestelde methode aan.

---

## Summary

The results of investigations into various aspects of precision grinding are reported.

The first chapter introduces precision contour grinding as a method to produce complex shapes in steel, ceramics and glass with sub-micron form accuracy and with roughness in the nanometer range. The grinding operation is described as a system, consisting of the machine and the material removal process. Inputs of the system are the process variables, the outputs are part features such as roughness, surface integrity and form accuracy.

The machine and process aspects, relevant for surface quality, are discussed and an overview of the equipment used for the grinding experiments is given.

In chapter 2, the emphasis is on theoretical and experimental work regarding the influence of the process variables on the surface roughness profiles measured and roughness patterns observed on ground parts. A good correlation exists between the theoretical predictions and the experimental findings and a technique to avoid roughness patterns on ground surfaces is presented.

It is generally known that even the most brittle materials can be cut in a ductile fashion under well controlled conditions (ductile regime grinding). In chapter 3 of the thesis, a fundamental investigation of the conditions that determine the transition from ductile deformation to cracking is presented.

Simulations are compared with the results of indentation experiments on glass. A fracture mechanics approach in conjunction with finite element calculations is shown to predict the threshold load for indentation cracking with reasonable accuracy.

In chapter 4, the influence of the dominant machine properties and process variables upon the form accuracy of ground parts is discussed. A model is used to study the influence of various parameters. The simulations are compared with experimental results.

The theory developed makes it possible to determine how accurate the cutting edge will follow the intended slide motion for an arbitrary machine and grinding process.

The theory also indicates possibilities to enhance the accuracy of the precision contour grinding operation. Experimental evidence of the effectiveness of the proposed method is presented.



---

## Table of contents.

1. Precision contour grinding, a systems approach .....	1
1.1. Introduction to the thesis. ....	1
1.2. Thesis scope. ....	2
1.3. Contour grinding compared to other techniques. ....	3
1.4. The grinding operation as a dynamic system .....	5
1.5. Quality aspects of precision ground parts for optical applications. . .	9
1.5.1. Form accuracy and aberrations of optics. ....	9
1.5.2. Roughness of optical components. ....	11
1.5.3. Surface integrity. ....	12
1.6. Experimental grinding facilities. ....	13
1.7. Conclusion. ....	16
References for chapter 1. ....	16
2. Generation of roughness profiles and patterns in precision grinding of small steel moulds. ....	19
2.1. Introduction to investigation of roughness generation. ....	19
2.2. Description of grinding experiments. ....	21
2.3. Experimental results. ....	21
2.4. Kinematic simulation techniques. ....	26
2.4.1. Single-grain simulation of roughness patterns .....	27
2.4.2. Multi-grain simulation of roughness profiles. ....	31
2.5. Comparison of simulations and experiments. ....	36
2.6. Conclusions. ....	41
References for chapter 2. ....	43

3. Mechanical model of the ductile to brittle transition. . . . .	45
3.1. Introduction, the cracking threshold load concept. . . . .	45
3.2. Survey of literature on indentation induced cracking of glass. . . . .	47
3.2.1. Sequence of cracking with blunt indenters. . . . .	47
3.2.2. The size effect in indentation. . . . .	48
3.2.3. Crack formation with sharp indenters. . . . .	51
3.2.4. Elastic-plastic stress field under conical indenters. . . . .	53
3.2.5. Failure criteria for cracking. . . . .	57
3.2.6. Conclusions from the literature studied and remaining problems. . . . .	61
3.3. Indentation experiments. . . . .	62
3.4. Finite element calculations. . . . .	68
3.5. Stress intensity factor ( $K_I$ ) calculations. . . . .	73
3.5.1. $K_I$ calculation method used in this study. . . . .	73
3.5.2. Stress intensity factors calculated from FE results. . . . .	75
3.6. Comparison of simulated and experimental results. . . . .	76
3.7. Conclusions . . . . .	78
 References for chapter 3 . . . . .	 80
 Appendix 3.1 : Discussion of stress intensity factor calculations. . . . .	 83

4. Form accuracy in precision contour grinding. . . . .	89
4.1. Problem description, method of investigation. . . . .	89
4.2. Random form errors in contour grinding. . . . .	93
4.2.1. Environmental effects. . . . .	93
4.2.2. Surface of the grinding wheel after conditioning. . . . .	95
4.3. Reproducible form error contributions. . . . .	95
4.4. Qualitative discussion of influences, nominal parameter values in contour grinding. . . . .	96
4.5. Grinding experiments. . . . .	98
4.5.1. Description of grinding experiments. . . . .	98
4.5.2. Results of grinding experiments. . . . .	102
4.6. Theory, non-linear model and simulation of profile grinding. . . . .	111
4.6.1. Physics and mechanics of the model. . . . .	111
Machine compliance. . . . .	111
Immersed area of the grinding wheel. . . . .	111
Material removal and grinding force. . . . .	115
Grinding wheel deflection. . . . .	117
4.6.2. Simulation of profile grinding. . . . .	122
4.6.3. Results and discussion of simulations. . . . .	124
4.7. Analytic model of contour grinding and cutting. . . . .	130
4.7.1. Linear process model. . . . .	130
4.7.2. Experimental determination of $p$ . . . . .	134
4.7.3. Implications and practical use of the linear theory. . . . .	136
4.8. Conclusions. . . . .	142
References for chapter 4. . . . .	143
Appendix 4.1. Geometry of the contact area. . . . .	146
Appendix 4.2. Summary of variables and equations used in simulations and linear process model. . . . .	149
List of variables used. . . . .	149
Set of equations used in the simulations. . . . .	150
Equations for the linear model. . . . .	152
Curriculum Vitae . . . . .	154
Dankwoord. . . . .	155

## **1. Precision contour grinding, a systems approach<sup>1</sup>.**

### **1.1. Introduction to the thesis.**

Precision contour grinding is used to manufacture complex shaped surfaces with sub-micron tolerances on dimension and form features, and with surface roughness in the nanometer regime. Brittle materials such as glasses, ferrites and structural ceramics can be ground in a ductile regime, where these materials are cut much like metals. In this ductile regime, little or no damage is introduced in the material, resulting in specular surfaces and good surface integrity (section 1.5.3).

To obtain routinely the accuracy described (and to strive for even better parts), requires a good understanding and control of all aspects of the machine, the material removal process and their interaction.

Precision engineering and machining has been practiced and improved at Philips Research Laboratories for decades. In the last decennium, the work had been mainly of an empirical nature. About 1985, the improvements implemented by the pragmatic and ingenious craftsmen in our laboratory had resulted in machines and diamond turning and grinding processes that could produce parts with accuracies in the 1  $\mu\text{m}$  range routinely, and even 0.2  $\mu\text{m}$  with special care.

However, the operations lacked reproducibility and the optical designers were asking for even more accurate aspherical surfaces (0.1  $\mu\text{m}$  profile accuracy in 1985, 10 nm in 1990).

It was felt that to meet these demands, the precision machining operations should be analyzed in depth to find out which aspects of the machines and processes would have to be improved; the more obvious dominant error sources were exhausted.

In 1985 a research program was started at the Philips Research Laboratories to investigate the diamond turning and grinding operations. The aim was to obtain generic knowledge about the precision machining processes and machine tools, to

---

<sup>1</sup> Much of the material in this chapter is based on a recently published review article (Franse 1990).

make higher accuracy feasible and to transform the nature of precision diamond turning and grinding from an empirical art-form to an engineering science.

The chapters of this thesis are about those parts of the research program dealing with precision contour grinding. In the first chapter, the precision grinding operation is described as a system, consisting of a machine and a material removal process. Together, these subsystems determine the surface quality of a ground part.

The quality of ground surfaces can be characterized in many ways, depending upon the application. Roughness patterns, surface integrity and form accuracy are very distinct aspects of surface quality.

In the sections of this chapter, the background of the main problems encountered in precision contour grinding are discussed and the problems treated in following chapters are put in an overall context.

In subsequent chapters of the thesis, the results of theoretical and experimental work concerning each of these aspects of surface quality (roughness, surface integrity and form accuracy) are reported.

## **1.2. Thesis scope.**

If the limits of achievable accuracy are to be identified and subsequently shifted, the limitations imposed by the machine tool, process induced errors and problems arising from the combination of process variables and the machine tool must be explored.

The accuracy of a machine tool is determined by the errors in the linear and rotary motions, the (closed loop controlled) machine stiffness, the layout of the measurement and control system and the thermal susceptibility of the machine structure. These machine tool characteristics and the overall machine tool accuracy were determined both theoretically and experimentally for our experimental facility (section 1.6).

The process variables (for instance spindle speeds, feed rate, depth of cut, grinding wheel size and type) determine the roughness generated on ground surfaces. In chapter 2 of the thesis, results of theoretical and experimental investigations regarding the roughness generated on the surfaces of steel moulds are reported.

For brittle materials, process variables can be chosen such that material is removed in a ductile mode. However, a transition from a ductile to a brittle

removal mode is observed, but not fully understood. In chapter 3, a fracture mechanics based model is presented for the action of a single grit (indenter) penetrating a glass surface. This model explains the phenomena observed in grinding and provides a basis to predict a threshold load for grinding that should not be exceeded to ensure ductile regime grinding.

Form errors of ground parts are due to the combination of process variables and machine characteristics (section 1.4). In chapter 4, the results of theoretical and experimental work in this field are reported for glass grinding.

Deflections due to the compliances of the machine structure and the cutting edge of the grinding wheel were found to be the dominant sources of form errors. The theory developed makes it possible to determine how accurate the cutting edge will follow the intended slide motion (motion copying ability) for an arbitrary machine and grinding process. Based on the theory, a correction method was found that makes it possible to achieve higher form accuracy, even with resilient grinding wheels.

### 1.3. Contour grinding compared to other techniques.

Stowers (1988) presented an overview of the characteristics of various precision fabrication processes in terms of removal rates and achievable accuracy. In an overview article by Franse (1990), the main characteristics of a wide range of processes are discussed. When it comes to manufacturing parts with complex profiled surfaces such as aspheric optical components, the main "competitors" of the grinding process are diamond turning and polishing.

With *diamond turning*, slide motions are controlled, and the tool should ideally follow the slide motions completely (Gijsbers 1980). Forces due to the tool-part motion are uncontrolled. Material removal is by direct mechanical action, thermal and chemical effects are of secondary importance. The accuracy is determined by that of the lathe and the diamond tool used. The tool-part interaction takes place in a very small contact area, so vastly different amounts of material can be removed from adjacent regions of the part.

In *polishing*, the load used to press the lap and part together is the controlled variable. Lap and part are moved relative to each other with an abrasive slurry between them. The abrasive action takes place in a relatively large area between the

lap and the part. The material removal depends on the action of many particles in contact, averaged over a relatively long time span (dwell time). The material removal rate is orders of magnitude lower than with diamond turning. Material removal is by combined mechanical and chemical effects. Large differences in removal rate over small areas are difficult to realize. Since the load is adjusted instead of the cutting depth, polishers need not be rigid like diamond turning machines. The relative resilience of polishers ensures that high peak loads cannot occur, and due to the low removal rate, polishing is much more subtle and forgiving than diamond turning. Polishing is the traditional technique used to manufacture spherical components and flats (Fynn 1988) and for these "simple" geometries, the form accuracy achieved by polishing is very hard to match.

*Precision contour grinding* ranks in between diamond turning and polishing in many respects. The machine tool motions are controlled.

Compared to diamond turning, the position of the cutting edge of the tool is less certain. At any time, any number between just one and a large number of grains can be in contact with the part. Grinding wheels tend to be compliant and wear (Shaw 1972), which makes it more difficult to achieve the desired form accuracy with grinding than with diamond turning.

Besides these disadvantages, there are some notable advantages of precision grinding over diamond turning. Using small wheels and small depths of cut, brittle materials can be cut in a ductile fashion with material removal being accomplished by shearing much like in metal cutting (Bifano 1988). Surface finish can be so good that polishing becomes unnecessary. The grinding process has the advantage over polishing of a much higher removal rate and has the ability to remove vastly different amounts of material from small areas. This makes it possible to manufacture complex shapes with high accuracy.

Concluding, it can be stated that precision contour grinding is especially suited to produce small complex shapes in materials that cannot be diamond turned.

For larger optics, ductile regime contour grinding can be used to produce optics more economically than by fracture mode grinding followed by polishing.

Other potentially interesting applications could be found in areas where current practice is to grind and subsequently polish or lap to remove subsurface damage, as in the fabrication of heads for magnetic recording.

#### 1.4. The grinding operation as a dynamic system

The precision grinding operation can be seen as a complex dynamic system (Franse 1990), in which the machine tool and the process are major subsystems (Fig. 1.1).

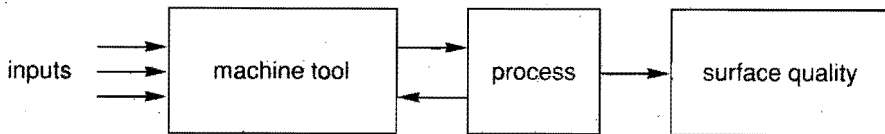


**Fig. 1.1** *The machining operation as a closed loop dynamic system with the machine tool and cutting process as subsystems.*

The precision and surface quality that can be achieved with a particular combination of machine tool and process variables depend on the dynamic characteristics of both the machine and the tool-workpiece interaction.

Machine tools have mechanical and thermal dynamic characteristics. Quantities such as movements or forces are measured and controlled at particular locations in the machine structure using sensors with certain sensitivities and accuracies. The characteristics of a machine tool are fixed in the design and installation stage of the machine tool.

Process variables that affect the tool-part interaction are chosen by the operator, and during the grinding operation external disturbances also act upon the system.

The machine behaviour and the tool-part interaction phenomena influence one another mutually and together they determine the surface quality of a part.



The systems approach can be illustrated for the grinding operation depicted in Fig. 1.2 by looking at the dynamics in the most critical direction of motion (the  $z$  direction, perpendicular to the part surface for nearly flat parts).

The inputs of the overall system (machine+process) are the values of the controlled variables (slide and spindle speeds); the overall output is the part.

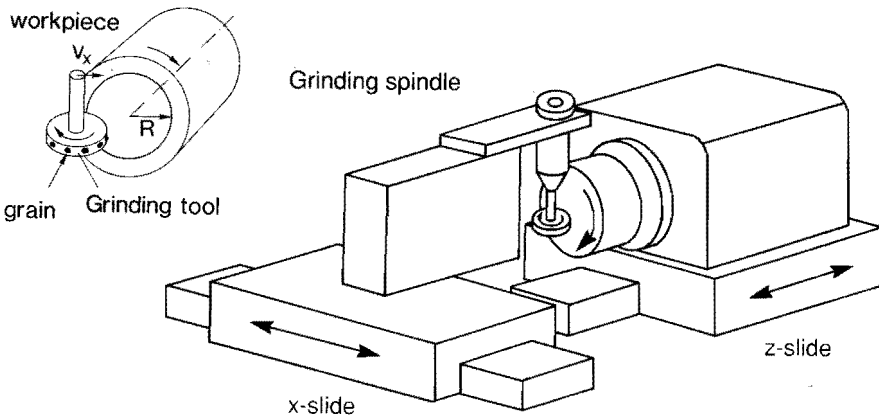


**Fig. 1.2** *Simplified contour grinding operation illustrating the dominant features of the machine+process dynamic system and the movements during grinding.*

If the dynamic behaviour of both the machine and the cutting process is linear, the system dynamics can be described in the Laplace domain using the block diagram in Fig. 1.3.

Assuming that the material removal process behaves like a simple spring (cutting stiffness  $k_c$ ), a machine infeed ( $z_s(s)$ ) results in a cutting force ( $F(s)$ ),

$$F(s) = k_c \cdot z_s(s) \quad \{1.1\}$$

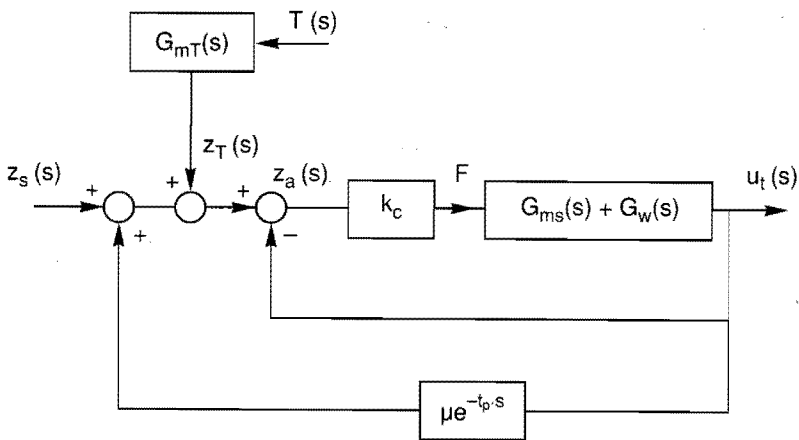
The transfer function of the structural loop of the machine tool ( $G_{ms}(s)$ ) and the dynamic compliance of the grinding wheel ( $G_w(s)$ ) determine the total deflection of the machine and cutting edge ( $u_t(s)$ ) due to this grinding force.

The actual depth of cut ( $z_a(s)$ ) becomes the infeed  $z_s(s)$ , minus the sum of the machine and grinding wheel deflection  $u_t(s)$

$$z_a(s) = z_s(s) - u_t(s) \tag{1.2}$$

Suppose a thermal disturbance  $T(s)$  acts upon the machine and (filtered by the thermal response  $G_{mT}(s)$ ) causes a deformation of the machine tool  $z_T(s)$ .

If such a thermal error motion is not observed by the control loop, it acts as a disturbance that is not rejected.



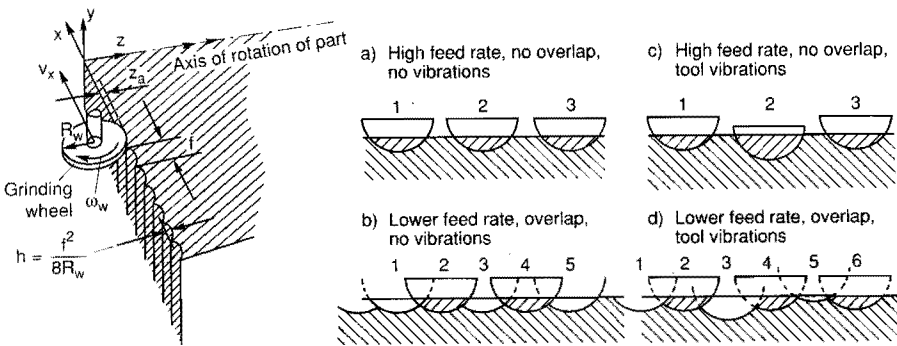
$z_s$ = Machine infeed	$z_a$ = Actual depth of cut	$k_c$ = Cutting stiffness
$G_{ms}$ = Machine structure dynamic compliance	$u_t$ = Total deflection	$\mu$ = Overlap ratio ( $0 < \mu < 1$ )
$G_w$ = Grinding wheel dynamic compliance	$T$ = Temperature	$G_{mT}$ = Machine thermal transfer function
$F$ = Grinding force	$t_p$ = Period of part revolution	$z_T$ = Thermal deformation

Fig. 1.3 Block diagram for the grinding operation of Fig. 1.2. Feedback paths are caused by machine dynamics and the overlap between the wheel-work contact area in successive revolutions of the part.

With a realistic machine tool, the structural flexibility of a machine tool  $G_{ms}(s)$  will vary with the position of the tool with respect to the part (Tlustý 1981).

Furthermore, the excitation of the machine tool by the process forces will result in vibrations and the depth of the spiral-like groove ground may become undulated in the tangential direction of the part (Kondo 1981, Takasu 1985). Since the feed rate ( $v_x$ ) is low, there is a partial overlap between the grooves cut in successive revolutions of the part (Fig. 1.4, the groove depth ( $h$ ), and the groove spacing ( $f$ ) are indicated as well). During the next revolution of the part (after a time delay  $t_p$ , corresponding to one revolution of the headstock spindle) the tool encounters more or less material depending on the phase of the machine tool vibration during the former revolution of the headstock spindle, thus there is a regenerative effect.

The variations in contact pressure due to the vibrations may also cause waviness around the circumference of the grinding wheel (Sexton 1982), that in itself may also amplify the machine tool vibration level. This regenerative effect is represented in the block diagram by the extra feedback loop that expresses the time delay ( $t_p$ ) associated with the headstock spindle speed and the amount of overlap ( $0 < \mu < 1$ ) between grooves cut in successive revolutions of the headstock spindle.



**Fig. 1.4** Grooves ground in successive revolutions of the part generally overlap one another. The instantaneous depth of cut therefore depends on the tool vibrations and the groove ground in the former revolution.

By analysis of the denominator of the overall transfer function of the closed loop system, combinations of feed rate, spindle speed and nominal depth of cut can be found at which the system is stable (Merrit 1965).

If the limit of stability is reached, self generated harmonic movements of the machine tool will occur and chatter marks become visible on the part surface.

In general, stiffer, well damped machine tools are less susceptible to chatter, and designers are always trying to improve these aspects of machine tools.

The generation of the waviness patterns discussed in chapter 2 is a practical example of the interaction between the machine dynamics and the cutting process.

The form errors (deviations of a desired profile) discussed in chapter 4 are also due to the interaction of the machine characteristics (compliance, thermal expansion) and the cutting stiffness that, for a practical grinding wheel, often has a non-linear character due to the contact geometry.

## **1.5. Quality aspects of precision ground parts for optical applications.**

For a more detailed discussion of the distinction between accuracy of dimension, form features and roughness of a part and how these are measured, the reader is referred to the extensive literature on this subject (Franse 1990, section 2 and references listed there in). Here, a brief description will be given of the importance of form accuracy, roughness and surface integrity for optical components.

Lenses in general give rise to imperfect images because of two broad classes of errors: geometrical aberrations and diffraction effects.

### **1.5.1. Form accuracy and aberrations of optics.**

*Form errors* of optics (and material inhomogeneities in transmissive optics) cause geometrical distortions (aberrations) of the image. Some common errors (power and coma) can be minimized in the fabrication stage, but often the optical system allows one to correct these errors by alignment of the optics. There are however, geometrical errors, such as spherical aberrations, that cannot be corrected in this way. Spherical aberrations can be minimized by using more lenses that correct each others errors. More elegant (fewer components) is to use lenses with surfaces that deviate from an exact spherical form (aspheres) (Braat 1983).

To limit the geometrical errors of the imaging system, the optical designer specifies the desired forms of the lens surfaces. This is done using a description of the surface as a polynomial. The allowable deviations of the coefficients of the polynomial terms determine the allowable form errors of the part. The geometrical quality of a lens is optically quantified in terms of the amount of phase distortion it causes when imaging a particular type of wavefront of monochromatic light. If the wavefront distortion caused by a lens due to geometrical errors is below one quarter of the light wavelength, the lens is said to be diffraction limited, since diffraction effects now limit the image quality. The required form tolerances are inversely proportional to the smallest wavelength of light the lens has to image. The tolerances of optical systems in general become more stringent for optical systems with a larger numerical aperture (NA).

The numerical aperture of a lens is defined as

$$NA = n \cdot \sin(u) \quad \{1.3\}$$

where  $u$  is the angle defined in Fig. 1.5 and  $n$  is the refractive index of the medium between the lens and object.

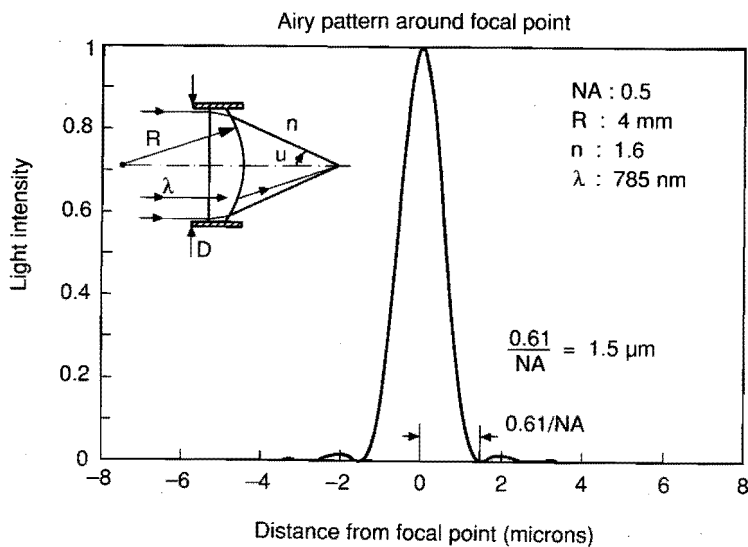


**Fig. 1.5** The light intensity distribution around a focal spot, known as the Airy pattern. This diffraction pattern is caused by the finite aperture of the lens.

Diffraction due to the finite aperture of even a geometrically perfect lens causes a light intensity distribution around the focal spot (Malacara 1988) known as the Airy pattern (Fig. 1.5). It consists of alternating light and dark circles around the focal point.

The smaller the distance between the focal spot and the first dark ring, the higher the resolution (or information density) that can be reached with the optical system. The resolution depends on the wavelength of light used and on the numerical aperture of the lens. The formula in Fig. 1.5 is for a circular lens with diameter  $D$ .

The optical wavefront distortion caused by form errors of the lens can be assessed rigorously by ray tracing techniques. Analytical translation of an error contribution of a particular error source in the fabrication process to an optical error is only possible for a limited number of cases (Braat 1990). Therefore, optical specifications are often handed over to the manufacturing engineer in the form of an allowable peak to valley deviation of the ideal surface profile. The manufacturing engineer can then decide on appropriate equipment and a machining sequence that keeps the combination of all errors stemming from the machine and cutting process within the allowable error band.

As stated in section 1.4, this requires knowledge about the machine accuracy (section 1.6) and the errors introduced by the combination of machine and tool workpiece interaction, which is the subject treated in chapter 4 of this thesis.

## 1.5.2. Roughness of optical components.

*Roughness* on the surfaces of optics scatters light in all directions, leading to loss of contrast between the light and the dark rings of the Airy pattern. To keep the diffraction effects within acceptable bounds, the designer will specify a maximum allowable rms (root mean square) value for the roughness of the lens. If, for a particular surface,  $S$  denotes the acceptable fraction of specular intensity loss by scattering, and the roughness amplitude is assumed to be normally distributed, the acceptable rms roughness for a lens used in transmission can be estimated from (Braat 1990)

$$\sigma = \frac{\sqrt{S} \cdot \lambda}{2 \cdot \pi \cdot \Delta n} \quad \{1.4\}$$

( $\lambda$  is the wavelength of light used,  $\Delta n$  is the difference in refractive indices between lens material and its environment).

The manufacturing engineer will have to choose his grinding variables so as to generate a scratch pattern that is dense enough and with scratches shallow enough to realize this demand everywhere on the surface. This is the subject of the study regarding the roughness of ground steel moulds for replication of Compact Disc lenses reported in chapter 2 of this thesis.

### 1.5.3. Surface integrity.

Many applications besides optical ones demand that some physical property of the material under the machined surface is not degraded by the machining operation. A first example concerns the magnetic properties of ferrites used in recording heads. Glass lenses used in applications in which powerful laser beams hit the surfaces have to be free of cracks and other defects to avoid damage from the stress cycling associated with the thermal gradients in the material during a laser pulse (Marion 1986).

If small (up to 10 mm diameter) aspheric glass lenses have to be manufactured, this can be done best by precision contour grinding (section 1.3 for a comparison to other techniques). Conventionally, glass removal is by brittle fracture, and after grinding, the lens surface is left with cracks (typically 10-20  $\mu\text{m}$  depth). These have to be removed by subsequent polishing. For small aspheric components, this is very difficult, since the form accuracy is easily degraded. Using small depth of cuts (order 0.1  $\mu\text{m}$ ) and low grinding forces, most glasses, ceramics and also silicon and germanium can be cut in a ductile fashion, much like metals (Broese van Groenou 1978).

This transition from brittle to ductile material removal has been attributed to mechanical, chemical and thermal effects. In conventional glass grinding, conditions can be such that the heat generated in the contact zone may lead to thermal softening or even melting of the glass (Schinker 1984). In precision contour grinding, thermal effects are less prominent (Bifano 1988) and the transition is more determined by mechanical effects (the "competition" of fracture and plastic flow phenomena).

If grinding is performed in the ductile regime, no cracks are introduced in the glass and specular surfaces are produced that need not be polished afterwards.

An economic benefit of this procedure is that polishing, usually an operation that takes considerable time, is eliminated, which generally reduces the price of the component.

The conditions under which material removal in glass grinding is by shearing (ductile regime) are commonly determined experimentally. To enhance the fundamental insight into the influence of parameters such as the grain geometry, material properties and process variables, a basic study was performed regarding the cracking of glass in indentation (chapter 3).

## 1.6. Experimental grinding facilities.

Experiments were initially carried out on a machine known as the Kolatje (Fig. 1.6, Fig. 1.7), named after the Colath production facility used at our laboratory.

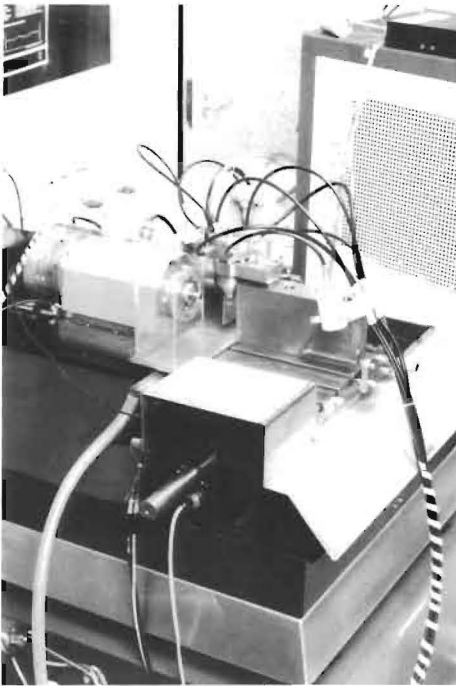


**Fig. 1.6**  
*Overview of the first experimental facility, the so called Kolatje.*



**Fig. 1.7**  
*Detail of the Kolatje, showing the specimen, the grinding spindle and the dress facility.*



It consisted of two hydrostatic slides mounted orthogonally ( $x$ - $z$  configuration) on a vibration isolated granite base. On the slides, air bearing spindles were mounted containing the grinding wheel and the part to be ground. An extra  $y$ -axis was used to be able to move a dress spindle (similar to the grinding spindle) up and down so the cutting edge of the grinding wheel could be contoured and trued. The movements of the  $x$  and  $z$  slides were measured using inductive LVDT (Linear Variable Displacement Transducer) probes.

Initial experiments showed that because of irreproducible behaviour, mainly due to lack of thermal stability, the machine was unsuited to study the form accuracy achievable with precision grinding.

The Kolatje facility could be (and was) used with success to perform experiments for the roughness generation study reported in chapter 2 of this thesis.



**Fig. 1.8** *The experimental diamond turning and grinding facility ESDO built as part of the research programme.*

It was decided to build a new experimental facility to study diamond turning and grinding, fully compatible with the Colath production facilities (ESDO, Fig. 1.8).

During the construction phase of this machine, numerous measurements and analyses were performed on it to establish a complete error budget (Donaldson 1980) of the machine. This enabled us to distinguish between limits imposed by the machine and by the combination of the machine and the process variables. It also served to identify the weak spots in the machine that need to be improved to enhance the machining accuracy towards the 10 nm precision level. The ESDO consists of two orthogonal hydrostatic slides mounted on a vibration isolated granite table. The slides are driven by friction drives, and motion feedback is provided by laser interferometer measurement systems (8 nm resolution). The machine was placed in a well controlled environment (0.04 °C P-V deviation around 20 °C) to improve the thermal stability. The error budget of the machine lists 85 error contributions, 10 of which proved to contribute significantly to the overall contouring accuracy of the machine.

Error source	Error (nm)	% of $E_{tot}$
x-slide motions	3.3	1.20
z-slide motions	3.8	1.38
Headstock run-out	20.0	7.29
Reference mirror	0.5	0.18
Slide compliances	0.5	0.18
Headstock compliance	0.4	0.15
Laser resolution	10.0	3.64
Thermal errors	30.0	10.93
Laser errors (refr.index)	6	2.19
Grinding spindle compliance	200	72.86
Total (worst case) error $E_{tot}$	274.50	100

**Table 1.1** Form error budget (z-direction) of ESDO, for a 5 mm diameter ground mould.

The main contributions for a typical diamond ground aspheric mould of 5 mm diameter are listed in Table 1.1.

The total error ( $E_{tot}$ ) has been calculated here by addition of the absolute peak values of all the contributing errors. In general, this worst case approach is too conservative, since not all errors occur simultaneously, and with the same sign. Some reproducible error contributions can be corrected for, so the accuracy achieved in practice can be considerably better than  $E_{tot}$ . A grinding force in z direction of 0.2 N has been assumed (determined experimentally) in the error calculations. The error due to the compliance of the grinding spindle is seen to be by far the largest single error contribution.

These machine characteristics are important for a good understanding of the theoretical and experimental results reported in chapter 4 of the thesis.

## 1.7. Conclusion.

In this chapter, the precision grinding operation has been introduced as a complex dynamic system. The specific advantages and problems of precision contour grinding compared to other techniques have been discussed. Various quality aspects of precision ground parts that are investigated in detail in the following chapters of the thesis have been introduced. This introduction also provides the reader with a framework to put the investigations into these different aspects of precision grinding (roughness generation, cracking of glass and form accuracy in contour grinding) in an overall perspective.

Since the results of grinding experiments always depend on both the process variables and the machine used, the main characteristics of the experimental facilities used have been presented.

In the next chapter, the results of theoretical and experimental work regarding the generation of roughness on precision ground parts will be presented.

## References for chapter 1.

Bifano T.G., 1988, "Ductile regime grinding of brittle materials", PhD Thesis, North Carolina State University, Raleigh, NC.

---

Braat J.J.M., 1983, Philips Techn. Tijdschrift, "Asferische Oppervlakken: het ontwerp en de optische voordelen", Vol.41, No.10, pp. 289-295.

Braat J.J.M., 1990, Personal communication.

Broese van Groenou A., Maan N. and Veldkamp J.B.D. 1978, Proc. 2<sup>nd</sup> Int. Symp. Science of Ceramic Machining, Gaithersburg MD: NBS, pp. 43-60.

Donaldson R.R., 1980, "Error budgets", Rep. Machine Tool Task Force, Vol.5, UCRL-52960-5.

Franse J., 1990, "Manufacturing Techniques for Complex Shapes", Rep. Progress in Physics, Vol. 53, pp. 1049-1095.

Fynn G.W. and Powell W.J.A., 1988, "Cutting and Polishing Optical and Electronic Materials", Bristol, Adam Hilgers.

Gijsbers T.G., 1980, "Colath, a Numerically Controlled Lathe for Very High Precision", Philips Techn. Rev., Vol.39, No.9, pp. 229-234.

Kondo Y., Kawano O. and Sato H., 1981, "Behavior of Self-Excited Chatter Due to Multiple Regenerative Effect", Trans. ASME, J. Eng. Ind., Vol. 103, pp. 324-329.

Malacara D., 1988, Chapter 2, "Diffraction and Scattering" in Physical Optics and Light Measurements, New York, Academic, pp. 49-105.

Marion J.T., 1985, "Strengthened Solid-State Laser Materials", Appl. Phys. Letters Vol.47, No.7, pp. 694-696.

Merrit H.E., 1965, "Theory of Self Excited Machine Tool Chatter", Trans. ASME, J. Eng. Ind. Vol.87, pp. 447-454.

Schinker M.G. and Doll W., 1984, "Untersuchung der Abtragsvorgange und -Mechanismen bei der Bearbeitung optischer Glaser mit Diamantwerkzeugen", Industrie Diamant Rundschau. No.4, pp. 234-239.

---

Sexton J.S., Howe T.D. and Stone B.S., 1982, "The Use of Increased Wheel Flexibility to Improve Chatter Performance in Grinding", Proc. Int. Mech. Eng. Vol.196, pp. 291-300.

Shaw M.C., 1972, "New Developments in Grinding", Pittsburg Pa, Carnegie.

Stowers I.F., 1988, "Review of Precision Surface Generating Processes and their Potential Application to the Fabrication of Large Optical Components", SPIE 966, pp. 62-73.

Takasu S., Masuda M. and Nishiguchi T., 1985, "Influence of Study Vibration with Small Amplitude upon the Surface Roughness in Diamond Machining", Ann. CIRP, 34/1, pp. 463-467.

Thusty J. and Ismail F., 1981, "Basic Non-Linearity in Machining Chatter". Ann. CIRP, 30/1, pp. 299-304.

---

## 2. Generation of roughness profiles and patterns in precision grinding of small steel moulds.<sup>2</sup>

### 2.1. Introduction to investigation of roughness generation.

Compact Disc lenses are produced by Philips using replica and injection moulding processes (Zwiers 1985, Andrea 1986). These processes require highly accurate dies, since diffraction limited optics (section 1.5.1) have to be produced. The moulds have an axi-symmetrical, aspheric shape, and are typically less than 10 millimeters in diameter. Their form accuracy has to be within  $0.1 \mu\text{m}$  of the specified profile and their surface finish must be better than 20 nm Rms (laser wavelength 785 nm).

Since the mould material is a hardened steel, precision profile grinding is used for the mould production. The grinding operation is carried out using precision lathes such as the Colath and the ESDO, described in section 1.6.

As discussed in section 1.4, the surface quality in precision grinding depends both on the process variables chosen and on the machine tool behaviour. At the outset of our research, it was unclear whether roughness generation would be predictable from the process variables alone or whether the machine behaviour would be important as well.

Surface roughness in itself causes scattering of light, leading to loss of intensity in the point where the laser beam is focused and broadening of the light intensity distribution around the focal spot. If, however, the roughness shows distinct patterns, more serious optical errors can be expected.

In this chapter the results of grinding experiments and simulations developed to investigate the influence of the process parameters and the machine tool upon the surface finish of ground parts are presented.

There is a considerable amount of literature regarding the generation of roughness in cutting and grinding. The majority of the investigations into surface roughness of parts aim to condense the complex information in roughness profiles to one, or a few, statistical parameters, which should of course be relevant for the functioning of the part (Whitehouse 1978).

---

<sup>2</sup> Part of the results reported in this chapter were published by Franse and de Jong in 1987.

These parameters are then used to control the manufacturing process (accept/reject parts, monitor machine and tool condition).

For grinding, roughness parameters suggested in the literature to control the process are of a statistical nature, due to the inherent uncertainty regarding the number and the shape of the grains that contact the part during a grinding pass (Buttery and Hamed 1978, Scott and Baul 1979, Konig and Steffens 1982, Yossifon 1982).

The unit event in the contact area is the scratching of the part by one grain. In view of the uncertainty regarding the grain positions and sizes, it is a natural idea to try to simulate the grinding-wheel part interaction as a stochastic process and predict the part roughness (Pandit 1982, 1984, 1986, Matsui 1979, Hasegawa 1980, Steffens 1983).

If the shape of cross-sections of scratches (in other words the grain shape) would be completely random, and the scratch events could be considered to be totally independent, the central limit theorem predicts a normally distributed surface roughness height and an auto-correlation function that exponentially decays (provided the scratch density is high and uniform over the surface). Hamed et.al. (1978) showed that if the grain shape is similar in nature for all grains, this will be found back in the form of the auto-correlation function of the roughness profile. The characteristics of the grain-part interaction and the spatial distribution of grains over the wheel surface would also be reflected in the shape of this auto-correlation function (Whitehouse 1978, Chetwynd 1986).

In an actual grinding operation, conditions are usually such that one position of the part is scratched by many grains as the wheel traverses over that particular spot. That means that the final roughness profile is the envelope of all these scratches (Batheja 1977, Sayles and Thomas 1976).

The importance of the dressing and trueing procedure used has been emphasized by a number of investigators (Hasegawa 1980). Some have taken measured grinding wheel profiles as the basis for roughness generation simulations (Suto 1981).

Based on the literature mentioned above, roughness measurement and determination of profile statistics seemed to offer possibilities for better process control. It was decided to investigate this by experiments and simulations for the precision contour grinding process.

---

## 2.2. Description of grinding experiments.

The experiments reported here are carried out on the machine known as the Kolatje, described in section 1.6.

Typical spindle speeds were 40.000 rpm and 300 rpm respectively for the grinding and the headstock spindle.

Although our numerical control offers contouring facilities, we limited ourselves in these experiments to the grinding of flat surfaces since the interest is directed here at the effects of process parameters and high frequency machine tool behaviour upon surface finish.

The workpiece material is ferritic stainless steel, heat treated to a hardness of 50 Rockwell C. The cylindrical test piece has a diameter of 10 mm.

When grinding a real mould, the grinding operation consists of a program of consecutive passes of the grinding wheel over the surface. The machine infeed is diminished in successive passes, and the program is concluded by a number of passes in which no additional depth of cut is given (spark-out). The idea behind this procedure is to first ensure the correct shape of the part and then to diminish roughness while maintaining the form accuracy. Often, the form accuracy is realized using a grinding wheel with a relatively hard binder, and the fine finish is achieved subsequently with a much softer grade wheel.

Since the effects of various process parameters upon the surface finish easily become obscured by this procedure, we experimented not only using this procedure, but also one in which we first ground a flat with good surface finish using the procedure described before, or alternatively we used a polished flat to start with, and then made just one or a specified number of additional grinding passes with a certain machine infeed. Typical grinding wheels used consisted of resin bond wheels, 8 mm in diameter, containing natural diamond grains, with an average grain size of 7  $\mu\text{m}$ .

## 2.3. Experimental results.

Surface roughness can be measured and characterized in many ways (Thomas 1982). Optical and mechanical methods were tried in the current study. Both have their specific merits and shortcomings. The optical methods (Schlieren method, interferometric profilometry) are good at showing errors with spatial wavelengths



of about  $5\ \mu\text{m}$  and larger. Smaller details such as scratches made by individual grains, protruding typically 0.2-0.3 times their diameter above the wheel binder surface cannot, however, be seen. Therefore, stylus measurements were made using a Talystep measurement apparatus equipped with a special diamond tip having a tip radius of less than  $0.1\ \mu\text{m}$ . The stylus was positioned at an off-center position on the specimen and a (nearly) tangential profile was recorded (Fig. 2.1).

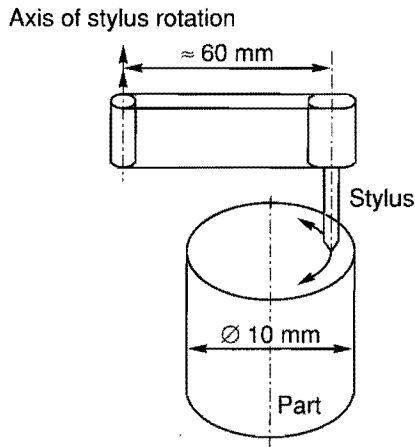


**Fig. 2.1** *The Talystep apparatus was used to record roughness profiles in tangential direction on precision ground parts.*

Fig. 2.2, Fig. 2.3 and Fig. 2.4 give examples of ground specimen as seen under a microscope.

The individual scratches (Fig. 2.3) form intricate patterns on the surface. These are regular and curved in some areas, and appear more random in other areas of a surface.

The optical measurements do not show these patterns clearly because they contain, in general, a lot of high spatial frequencies (small wavelengths).

It is evident that roughness profiles in the tangential direction can be expected to show different periodic features depending on the radial position at which the measurement is made. An example is given in Fig. 2.5.

This tangential profile (Fig. 2.5) shows undulations (waviness) of the surface in the coarser region of such a roughness pattern. On different ground surfaces, various types of roughness patterns were observed. These patterns will be discussed in detail in section 2.4.1.

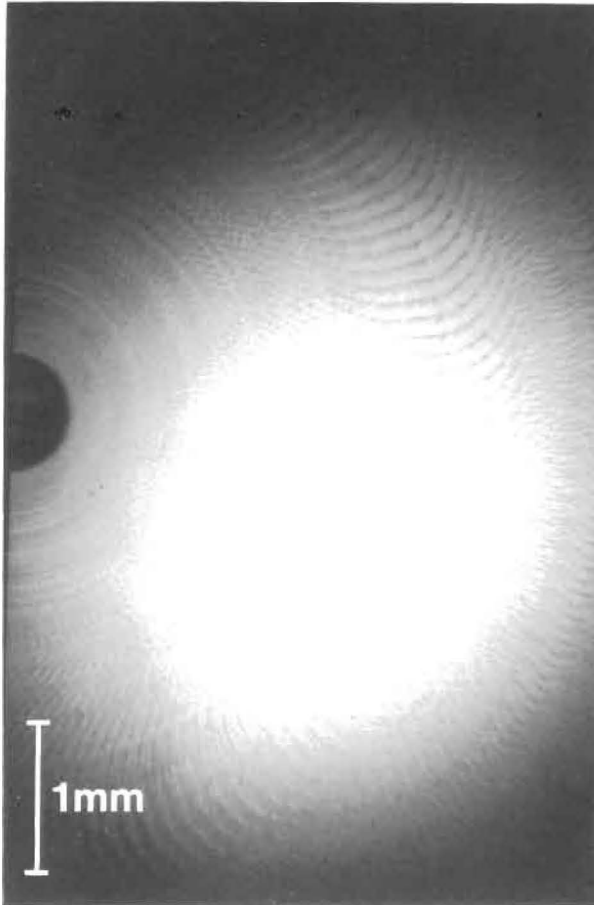


**Fig. 2.2** *Surface of a ground specimen. Individual scratches cannot be seen at this low magnification. The overall pattern they form is evident.*



**Fig. 2.3** *Surface of Fig. 2.2, at higher magnification. Individual scratches are visible. The uneven scratch distribution results in the roughness pattern observed in Fig. 2.2.*

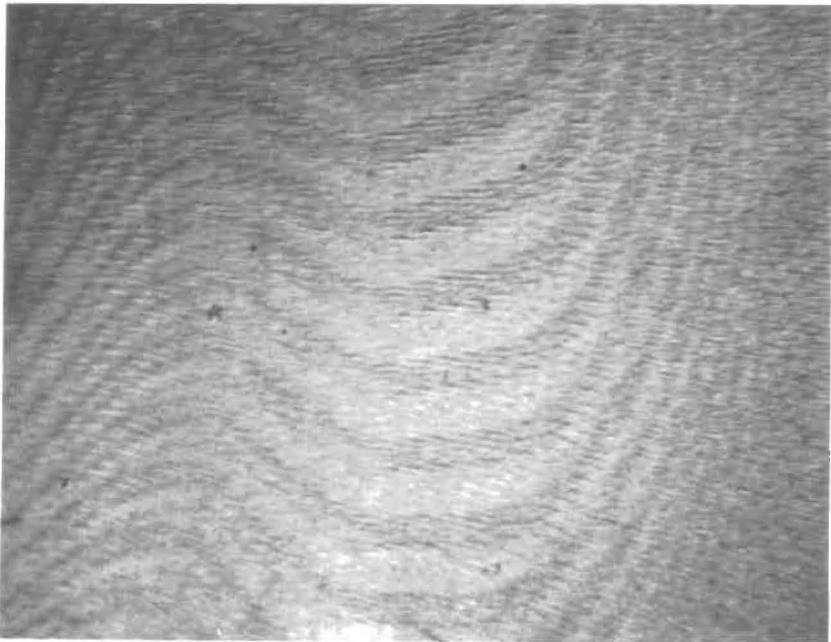


**Fig. 2.4** *Another surface at intermediate magnification, showing a different pattern. In experiments, identical machine settings would give different patterns.*

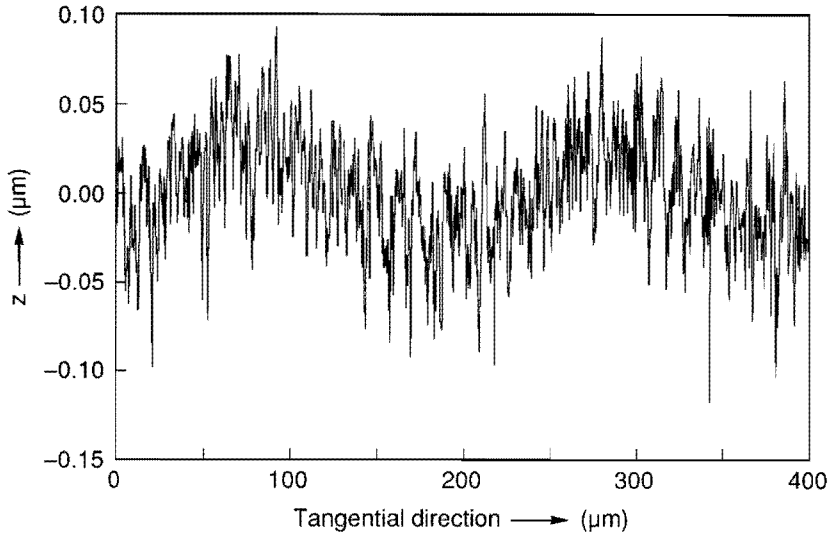


**Fig. 2.5** *Roughness profile in tangential direction over the surface of Fig. 2.2. The profile is made over a coarse part of the pattern in that figure.*

The information present in a roughness profile  $z(x)$  is often extracted in the form of statistical parameters such as the arithmetic or center-line average  $R_a$ , the root mean square average  $R_{ms}$ , the peak-to-valley height  $R_v$ , power spectral density  $G(\omega)$ , auto-correlation function  $R(\tau)$  and moments of the height distribution of the profile (Thomas 1982). We processed the measured data on a mainframe computer with software that enables us to calculate a variety of roughness parameters and offers good graphic facilities.

There is in our case no obvious parameter that stands out from the abundance of statistical properties that can be determined from a surface profile to try to link the process variables to the quality of a surface.

$R_a$ ,  $R_{ms}$  and  $R_v$  values can be compared for different specimen, if tangential profiles are measured at the same radial position, and provided the overall roughness pattern is similar in that region on those specimen.

The same holds true for statistical properties derived from the auto-correlation function or the power spectrum of a roughness profile.

It was decided that if the influence of grinding process parameters upon surface finish was to be understood, the first step should be to understand how the roughness patterns on the ground surfaces are generated.

#### **2.4. Kinematic simulation techniques.**

Fig. 1.2 shows schematically the movements during the grinding experiments. The unit event in the interaction between the grinding wheel and the workpiece surface is a single grain protruding from the circumference of the wheel, scratching the surface.

The surface finish of the part results from the convolution of these unit events as the interaction proceeds. Two types of simulations must be distinguished:

*A single-grain simulation* was developed to understand the generation of the experimentally observed roughness patterns on the surfaces.

In this simulation the positions of successive scratches made by one single grain protruding from the wheel surface are calculated. This simulation gives sufficient detail to look at the influence of kinematics on roughness patterns on the surface. Since the effect of only one grain is considered, this does not provide enough information to study the surface roughness at a particular spot on the surface.

*A multi-grain simulation* was used to investigate how the roughness in tangential direction at a certain radial position on the surface is generated. This simulation takes into account the effects of kinematics and all those grains that protrude enough to make contact with the surface as the wheel moves radially over the surface. These profiles can directly be compared with those measured experimentally.

### 2.4.1. Single-grain simulation of roughness patterns

Suppose there is only one grain on the wheel perimeter that scratches the surface. We assume the length of this scratch to be constant at every position on the surface. The grinding wheel rotates at a speed  $N_w$  and the part at a speed  $N_p$  (both in rpm).

The part will have rotated (clockwise) over an angle  $\phi$  in the time ( $t_w$ ) it takes the grinding wheel to complete one revolution and the single-grain comes in contact again.

$$t_w = \frac{60}{N_w} \quad \{2.1\}$$

$$\phi = \frac{2 \cdot \pi \cdot N_p}{N_w} \quad \{2.2\}$$

In this same time  $t_w$ , the grinding wheel has moved towards the center of the workpiece by an amount depending on the velocity of the slide (the feed rate  $v_x$ ). The relative positions on the part surface of successive scratches can thus be determined from kinematic considerations alone.

If the part has rotated once, the number of scratches made on it is calculated as the ratio of the angular velocities of wheel and workpiece. In general, this is not an integer number. Scratches made during the next revolution of the workpiece will therefore be shifted over an angle  $\beta$  (Fig. 2.6) with respect to those generated in the previous revolution (mod denotes the non-integer fraction of the speed ratios).

$$\beta = \text{mod} \left( \frac{N_w}{N_p} \right) \cdot \phi \quad \{2.3\}$$

A computer program was written to calculate the position of successive scratches for given angular velocities of wheel and workpiece and a given feed velocity of the wheel along the surface.

Fig. 2.6 shows a first example of a scratch pattern that was calculated in this manner, assuming constant values for the angular velocities of grinding wheel and part. It is noteworthy that the simulations are carried out using low values for the angular velocities of wheel and part. This limits the absolute number of scratches during a simulation to a reasonable amount.

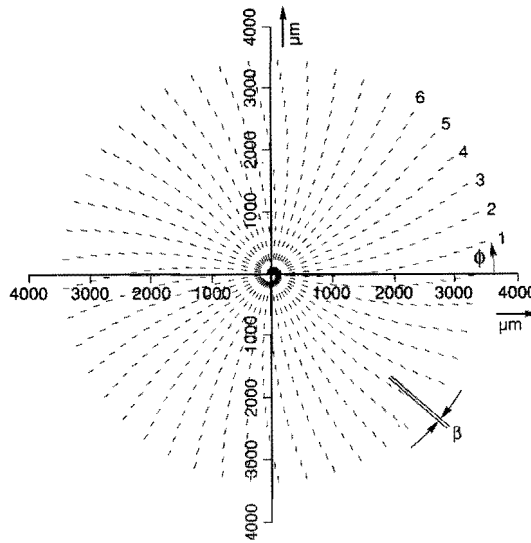


**Fig. 2.6** *Simulated roughness pattern. The part rotated at 2.7 rpm, the grinding wheel at 120 rpm. Both angular speeds were assumed constant. Feed rate  $v_x = 10 \mu\text{m/s}$ .*

The roughness patterns can still be studied with these low speeds, since for these it is the ratio of grinding wheel and part speed that is relevant.

After a number of revolutions of the workpiece  $n$ , given by,

$$N_w - n \cdot N_p \quad \{2.4\}$$

( $n$  is the smallest integer for which eq. {2.4} is valid), the scratches are positioned once more at the same  $\phi$  positions as  $n$  revolutions of the part before. Due to this geometrical effect, waviness of the part with a period  $\lambda_r$ ,

$$\lambda_r = n \cdot t_p \cdot v_x \quad \{2.5\}$$

can be expected in the radial direction if only one grain (or a small portion of the grinding wheel) is actively cutting the surface. This periodicity (wavelength) can be considerably longer than the "basic" period in radial direction ( $f$ ) caused by the combination of the feed rate  $v_x$  and the angular velocity of the part ( $N_p$ ).

$$f = v_x \cdot t_p = \frac{60 \cdot v_x}{N_p} \quad \{2.6\}$$

The simulated spiral pattern of Fig. 2.6 does not explain the curved patterns observed on the test specimens (Fig. 2.2 for example). During a number of experiments, the grinding forces were measured. A decrease in the grinding force  $F$  from typically 0.2 to 0.02 N was observed as the grinding wheel moves from the perimeter towards the center of the specimen (chapter 4). This implies a variation of the torque exerted on the grinding spindle and the specimen. It was decided to simulate the effect of small position-dependent variations in the speeds of the spindles with the simulation technique.

Fig. 2.7 and Fig. 2.8 show examples of simulated patterns that were obtained assuming linear changes in either the wheel or the workpiece angular velocity as a function of the radial position ( $x$ ) of the grinding wheel with respect to the part center. From these figures it is seen that the sign of the curvature of the patterns depends upon whether the angular velocity of wheel or workpiece changes, and whether the angular velocity increases or decreases with the radial position.

The "curvature" of the pattern depends on the rate of the spindle speed variations. The variety of patterns observed experimentally and the fact that on one surface the curvature may change sign very rapidly (rapid variations in the curvature of the pattern, Fig. 2.4) lead to the conclusion that in the experiments variations of the angular speed of either the wheel or the workpiece spindle (or both) must have occurred.

In a number of experiments the angular speed of the workpiece was measured and this was seen to fluctuate slowly about 1 rpm during a grinding pass. The rotational speeds of grinding wheel and workpiece are such that this is already enough to make the angle  $\beta$  fluctuate between 0 and  $\phi$  radians.

The nominal value of  $\beta$  between positions of scratches is determined by the ratio of the nominal angular velocities.

This implies that a very small variation of the workpiece spindle speed has the same effect on  $\beta$  as a much larger fluctuation in the angular velocity of the grinding spindle.

The simulations show that circumstances may easily arise in which the scratch density along a circle on the workpiece surface fluctuates.



A situation where the scratches made in successive revolutions of the wheel virtually coincide ( $\beta=0$ ) causes undulations on the workpiece, seen in some of the stylus measurements, for instance the tangential profile in Fig. 2.5.

Unbalance of the grinding spindle can cause a similar effect, but in this case, the undulations were absent on other areas on the same specimen surface. This kinematic effect also promotes vibration of machine tool components such as the grinding spindle (regenerative effect as discussed in section 1.4).

The remedy to this problem follows from the results presented: a slight change of the part (or grinding spindle) velocity can be enough to alter the value of  $\beta$  drastically, and this can be used to avoid the development of these undulations.

In practice, when the undulations start building up, the vibration level on the machine tool (monitored with an accelerometer on the grinding spindle) increases slightly. A minor adjustment of the headstock spindle speed by the operator proved to be enough to prevent the undulations in tangential direction from building up.

Another measure to achieve the same result automatically is to feed a small random signal to the headstock rotary drive mechanism so that the phase relation (the value of  $\beta$ ) between part and grinding tool constantly fluctuates.

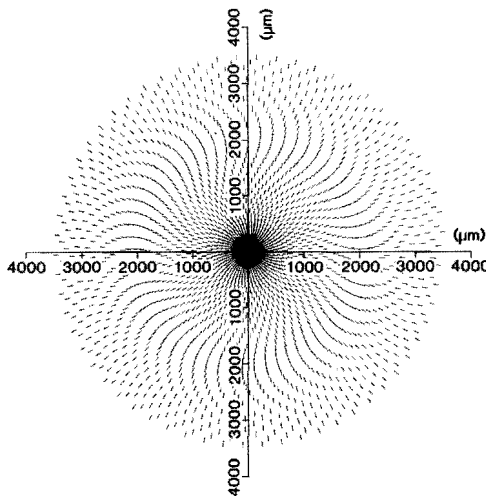


**Fig. 2.7** *Simulated scratch pattern. Constant part speed (2 rpm). The wheel speed decreased linear with the radial wheel position  $x$  ( $N_w=120-x$ ,  $x$  in mm). Feed rate  $v_x=3 \mu\text{m/s}$ .*

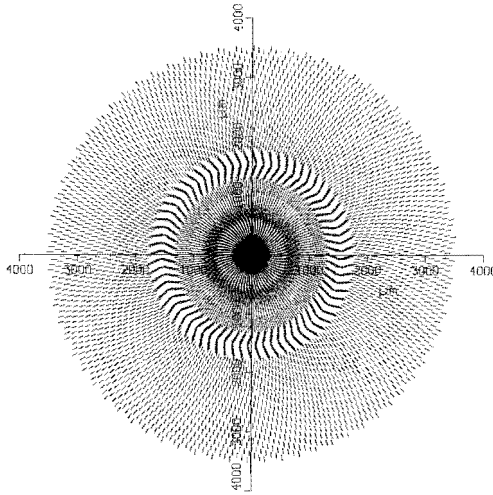


**Fig. 2.8** *Simulated roughness pattern. Wheel speed 120 rpm. Part velocity:  $N_p = 1.7$  rpm for  $x > 2$  mm,  $N_p = 1.7 - 0.02 \cdot x$  for  $x < 2$  mm. Feed rate  $v_x = 1$   $\mu\text{m/s}$ .*

The fact that the single-grain simulations show patterns that correspond very well with those experimentally observed indicates that in this type of grinding, a few highest grains along the wheel perimeter dominate the overall appearance of the surface.

#### 2.4.2. Multi-grain simulation of roughness profiles.

The multi-grain simulation provides information complementary to that obtained by the single-grain simulation (section 2.4.1). The single grain-simulation reveals overall roughness patterns on the surface; finer details of the surface roughness become apparent with the multi-grain profile simulation technique.

The aim of this simulation technique was to take into account the effects of as many of the process parameters as possible and to determine their relative importance for the roughness generated anywhere on the part. The situation during the grinding operation is represented in Fig. 2.9.

The part is, for the moment, assumed to be perfectly flat. Consider a circular track on the surface (radius  $R$ , its center coinciding with that of the part). If this track is unfolded we obtain a profile with a length ( $L$ )

$$L = 2 \cdot \pi \cdot R \quad \{2.7\}$$

This profile is represented in the computer as a numerical array. The value of the array elements represents the profile height ( $z$ ) at equidistant points along the profile, spaced  $0.1 \mu\text{m}$ .

An arbitrary grinding grain protruding from the circumference of the wheel may or may not come into contact with the surface during a revolution of the grinding wheel. Such a grain is characterized by its equivalent radius (Fig. 2.10), its protrusion height and its angular position on the wheel perimeter.

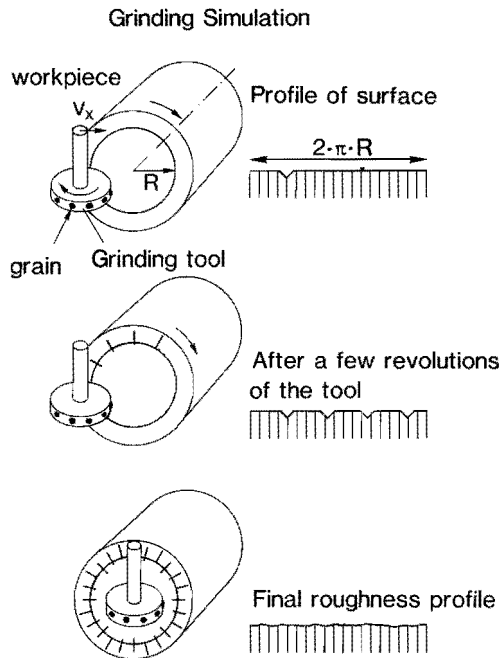


**Fig. 2.9** Schematic view of the movements during grinding and the development of a tangential roughness profile in the multi-grain simulation.

If a grain comes in contact, it will scratch the workpiece. The intersection of this scratch with the circular track on the workpiece will depend upon the depth of cut, the instantaneous value of the eccentricity of the spindle in its bearings due to unbalance of the wheel, the grain geometry and the position of the wheel with respect to the center of the piece.

The shape of this intersection is approximated as a triangular area as indicated in Fig. 2.10.

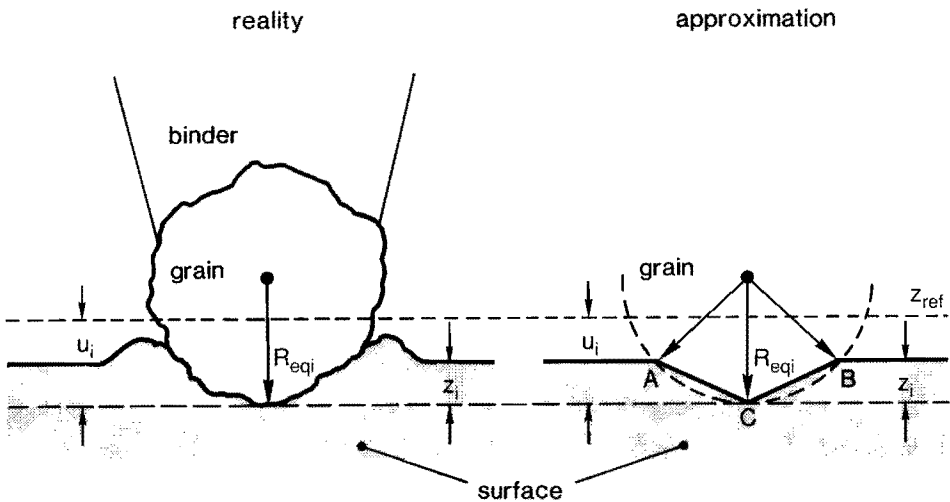


**Fig. 2.10** The intersection of a scratch and the simulated profile is calculated from the cutting depth  $z_i$  and the equivalent radius  $R_{eqi}$ .

The position of points A, B and C are calculated from the factors mentioned above. The reference height  $z_{ref}$  in Fig. 2.10 is determined from the actual depth of cut ( $z_a$ ) of the wheel, the initial average height of the surface profile ( $z_{avg}$ ) and the maximum protrusion height of grains along the grinding wheel perimeter ( $u_{max}$ ).

$$z_{ref} = z_{avg} + u_{max} - z_a \quad \{2.8\}$$

The protrusion height ( $u_i$ ) of a particular grain is calculated with respect to this reference height. Elastic effects and side flow of material are not taken into account in the simulation.

The scratches are accounted for in the profile by modifying the values of the appropriate array elements. If the workpiece has made one complete revolution, the same grinding grain comes in contact again and makes a new scratch. The position of this scratch relative to the former one is determined by the angular velocities of wheel and workpiece, and the radius of the circular track ( $R$ ) under consideration.

Until now, we have looked at the action of just one grain protruding from the grinding wheel perimeter. The multi-grain simulation takes into account the fact that there are more grains protruding from the perimeter. They will have different shapes and may wear as a result of the scratching action. In this manner a tangential profile of the surface is built up by the successive contacts between multiple grains and the workpiece.

A schematic overview of the simulation program is given in Fig. 2.11. Three stages can be distinguished during a simulation: *Input*, *Interaction* and *Output*.

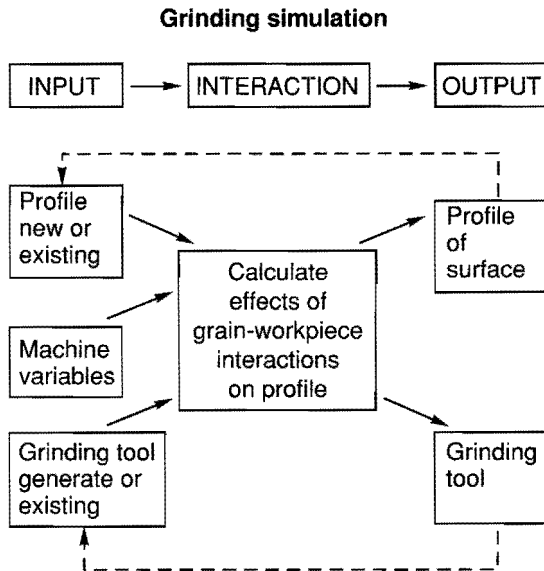


**Fig. 2.11** Schematic overview of the multi-grain simulation program to calculate tangential roughness profiles.

The program reads the initial part roughness profile from an input file. This enables the user to assume an initially perfect flat surface, or alternatively a profile that was created in a former simulation (to study the effect of fine grinding after rough grinding for instance).

The input file from which the profile data are being read has the same format as those of real profiles measured with the Talysurf and Talystep apparatus.

This enables the analyst to use the same software to calculate the statistical parameters of the simulated profiles. It also makes it feasible to incorporate a model for the compliance and dynamics of the system and study the effect of initial waviness and roughness. Process parameters such as the depth of cut, angular and feed velocities and also the shape (out of roundness, runout) and unbalance of the grinding wheel may be specified.

Initially, it was attempted to measure grinding wheel profiles (using both optical and mechanical methods) as a basis for the simulations. Unfortunately, the interpretation of the wheel profiles was very difficult, it was virtually impossible to distinguish between binder and grains.

Therefore, for the simulation, a grinding wheel profile is determined by looking at the wheel composition. The average and the variance of the equivalent radii of the grains, the weight percentages of grain, binder and porosity in the wheel and its diameter are specified. With these numbers the average distance between adjacent grains is calculated. In the next step, a file is created containing the position, shape and protrusion height of the grains which are assumed to lie on the circle of the wheel perimeter. This is done by drawing random numbers from the specified distributions of the grain radii (Gaussian, Raleigh or log normal) and determining their positions on the perimeter, assuming the distance between adjacent grains to be distributed normally around the calculated mean value. The effect of the dressing and trueing operation is taken into account by removing from the file all grains that protrude more than 0.4 times their equivalent diameter above the binder. The user may also specify a wear factor. In that case the protrusion height of the grains is diminished after successive contacts with the workpiece, while their equivalent diameter is kept constant (linear wear law). This effectively simulates the blunting of grains as grinding proceeds. Instead of generating a wheel in this manner, it is also possible to use a file representing an existing wheel surface.

This option is useful to simulate the particular effect of one process parameter with exactly the same grinding wheel, or to simulate the effect of particular aspects

of the wheel, such as one very large grain or evenly distributed, equal-sized grains etc.

Once the input is read in, the interaction phase of the simulation starts. The effects of successive contacts between protruding grains and the profile are calculated by the method discussed above.

In the output stage of the simulation, files are made of the resultant tangential surface roughness profile and of the wheel surface used in the simulation. Both can be used again as input for further simulations. The roughness profile can be studied in more detail with the software written for the characterization of surface roughness.

Notwithstanding the fact that a number of simplifications had to be introduced in the multi-grain simulation, the technique offers many possibilities to investigate the effects of various process parameters upon surface finish. It offers the opportunity to change one variable at a time and study its effect. This is seldom possible in real grinding experiments.

## 2.5. Comparison of simulations and experiments.

The examples of simulations presented here were chosen from a large number of simulations performed to investigate the effects of different process variables. These particular results were selected because they can be compared directly with the results of the grinding experiments. The results and conclusions of some other simulations and experiments will also be discussed briefly.

Fig. 2.12 shows the result of two simulations. In these, the same process parameters and grinding wheel were used in both simulations. The only difference between the two simulations was the radius  $R$  of the circular (tangential) track under consideration.

The simulated profile with the larger radius ( $R=0.2$  mm) in Fig. 2.12 clearly shows a deepest scratch, made by the grain that protrudes most from the grinding wheel surface. Next to that we see some more scratches produced by other active grains. After a distance

$$\lambda = \frac{2 \cdot \pi \cdot R \cdot N_p}{N_w} \quad \{2.9\}$$

the profile repeats. This is the distance  $\lambda$  which the workpiece moved in tangential direction during one revolution of the grinding wheel.

In the simulation using the smaller radius ( $R=0.1$  mm), the periodicity is a factor 2 smaller. Because of the lower tangential velocity of points on the part surface closer to the center, the scratches made by successive grains on the wheel perimeter are spaced closer and some have started to overlap. Precisely the same effect can be obtained if the radius  $R$  is kept constant and the angular velocity of the wheel is increased by a factor two.

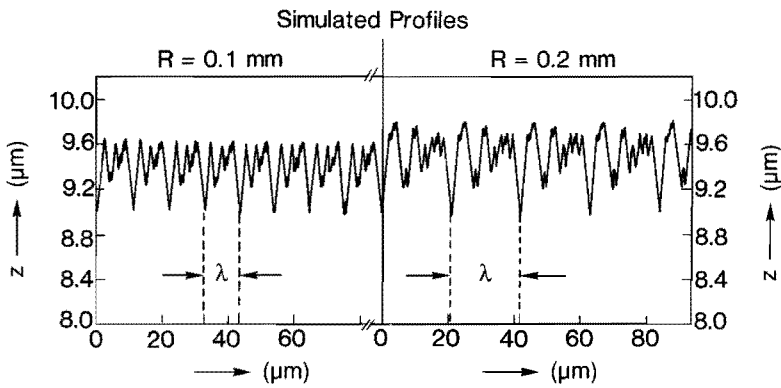


**Fig. 2.12** Two tangential profiles, simulated using the same "tool" and "machine settings". The radius ( $R$ ) of the circle on the part considered as profile was different.

A more abstract formulation of this conclusion is to say that the spectral content of the surface profiles constantly changes with the radial position of the profile.

This implies that for this particular way of grinding, the information contained in the spectrum and auto-correlation function of surface roughness profiles cannot be easily used to monitor the process and judge surface quality.



From these simulations yet another conclusion can be drawn. Increasing the angular velocity of the wheel, or moving closer to the center of the piece will result in a decrease of the number of visible scratches within the characteristic wavelength  $\lambda$ . In shop practice it is often heard that in precision grinding it is just one, or at most a few, of all the grains along the wheel perimeter which do all the work. The results of the simulations indicate that this is not so. Other grains are active as well and they do remove material. However, the final profile is the envelope of all these scratches, many of which overlap. Especially with high cutting speeds, and near the center of the piece, the only visible imprints left on the surface are those made by the few highest grains.

Fig. 2.13, Fig. 2.14, and Fig. 2.15 show results of stylus measurements in the tangential direction at various radial positions on a specimen. The periodicity in the profiles is indicated. The Talystep apparatus measures along a circular arc with a radius of 60 mm (Fig. 2.1), so the measurement deviates from the intended tangential profile. The deviations are largest in the beginning and at the end of the measured profiles. In these regions the periodicity of the profiles is therefore less prominent.

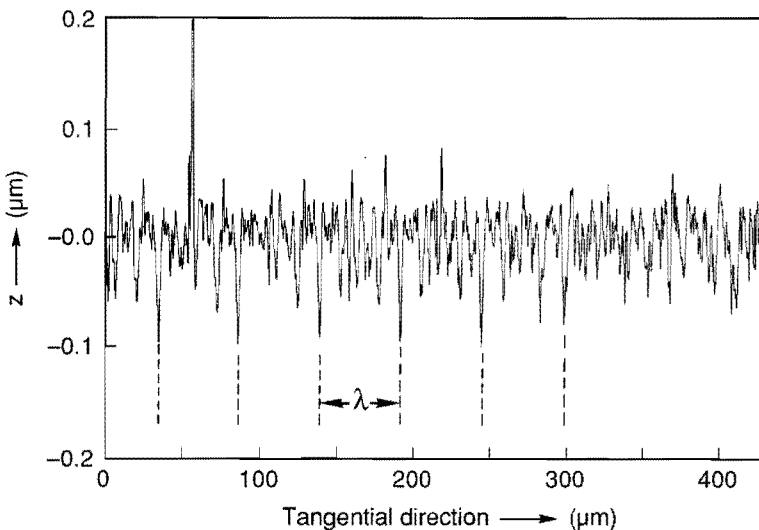


**Fig. 2.13** Talystep profile, measured in tangential direction,  $R=1$  mm, on ground surface of Fig. 2.2.

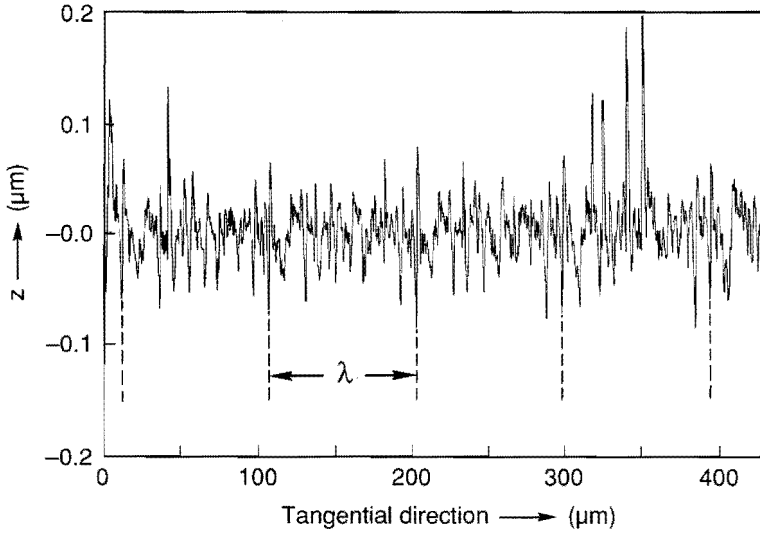


**Fig. 2.14** *Talystep profile, measured in tangential direction, R=2 mm, on ground surface of Fig. 2.2.*

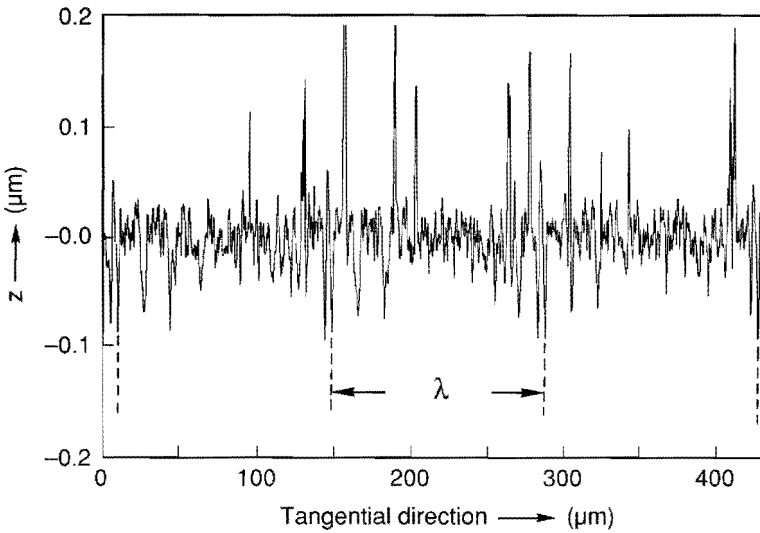


**Fig. 2.15** *Talystep profile, measured in tangential direction, R=3 mm, on ground surface of Fig. 2.2.*

The calculated (eq. {2.9}) and measured characteristic wavelengths ( $\lambda$ ) at different radial positions are given in Table 2.1. Within the experimental error bounds, the agreement between experimental and calculated values is good.

R (mm)	Calculated wavelength ( $\mu\text{m}$ )	Measured wavelength ( $\mu\text{m}$ )
1	47	52 +/- 7
2	95	96 +/- 8
3	142	139 +/- 10

**Table 2.1** *The calculated and measured values of the characteristic wavelength of tangential roughness profiles.*

The effect of grinding grain wear was simulated assuming a protrusion height that decreases linearly with the number of times a grain has contacted the part. The simulations predicted a gradual, steadily diminishing peak-to-valley roughness value  $R_t$ . In practice, a grinding wheel wears rapidly over a short time right after dressing/truing. After that, the wear rate is much lower for quite a while. Finally the wheel becomes so blunt that reconditioning is necessary.

During the initial run-in wear period, precision contour grinding is impossible since the wear affects the contour accuracy (chapter 4). In the following low-wear stage, the wear during one grinding pass does not have a noticeable influence on the roughness profiles at different locations on the part.

This conclusion regarding the small influence of grinding wheel wear in the stable wear regime does of course depend on the fact that we ground small diameter parts, and also on the wear resistance of the particular resin bond grinding wheel used.

The multi-grain simulation predicts a slight decrease in the peak-to-valley value of the tangential roughness profile as we move from the edge of the part towards the center.

Evaluation of the peak-to-valley roughness value ( $R_t$ ) of experimental profiles taken at various radial positions of the surface indeed did show a gradual decrease

as the center is approached, provided the roughness was not increased by machine tool vibrations during the pass.

All in all, the peak-to-valley roughness value  $R_t$  was found to be the most reliable indicator of the surface quality as a function of the process variables.

However, the peak-to-valley roughness value was found to be mainly determined by the largest difference in protrusion height of active grains. This illustrates a very important conclusion regarding this type of grinding: The peak-to-valley roughness of a ground surface very much depends on the run-out of the grinding wheel and the deviations in size and protrusion heights of active grains.

Thus, the conditioning of the wheel is extremely important. If there are a thousand active grains, the result is optimal if they all protrude the same amount from a perfectly round wheel. One single outlier however, and the peak-to-valley roughness value is severely increased, notwithstanding the other 999 optimal grains.

The peak-to-valley roughness value is therefore a very stringent quality indicator.

It is doubtful whether one periodic deep scratch severely degrades the optical quality of the surface, particularly in view of the small fraction of the total surface area involved (the deep scratches compared to the rest of the surface). Therefore, from a functional point of view, the peak-to-valley roughness is probably a too severe quality control criterion. However, a person inspecting a surface under the microscope is perceptive for, and attracted by, this kind of flaws on the surface.

Once the attention of the observer is "focussed" on these local defects, the inclination to grade the surface quality as insufficient becomes large.

## 2.6. Conclusions.

- A kinematic single-grain simulation method was used to study the surface roughness patterns experimentally observed on ground surfaces.
- With the single-grain simulation, the scratch density is too low to evaluate the surface roughness, but the technique was very successful in predicting the effect of (low frequency) spindle speed fluctuations on the shape of the overall roughness patterns observed on ground specimen.
- Experimentally, it was found that roughness patterns also promote machine tool vibrations. This leads to undulations in tangential direction on surfaces as a result of the patterns amplifying the machine tool vibration level.

- 
- These undulations can be avoided by deliberately introducing slight fluctuations of the headstock spindle speed. This disturbs the phase relation between the grinding wheel and the part.
  - Fine details of local surface roughness as a function of the process variables were studied using a multi-grain simulation technique to generate tangential roughness profiles.
  - For the grinding process investigated here, the surface speed of the part decreases while the grinding wheel moves towards the part center. This implies that the spectral content of tangential roughness profiles changes continuously.
  - This changing spectral content complicates the use of numerical parameters derived from the power spectrum and/or auto-correlation function of the roughness profile for process control purposes.
  - The peak-to-valley roughness of surface profiles was found to be a very sensitive, but perhaps unduly severe indicator for the surface quality of ground parts.
  - The peak-to-valley value  $R_t$  of the tangential roughness profiles is determined by:
    - The shape (total run-out) of the grinding wheel (indicating the importance of the dressing/truing operation).
    - The maximum height difference between the active grains.
    - Unbalance of the grinding spindle (leading to excentricity).
    - Machine tool vibrations.
    - The ratio of the angular velocities of the grinding wheel and the part (in combination with the machine dynamics).
    - The spark-out time (number of passes made over surface without additional machine infeed).
  - If the scratch density on the part surface is high, the overlap between scratches made by different grains affects the characteristics of the roughness profile significantly. Although many grains may be actively cutting the part, the imprint of only a few most protruding grains will be visible afterwards. In those cases, the characteristics of the part roughness cannot be predicted by looking at the statistical properties of the wheel surface.
  - The results of simulations of tangential roughness profiles show trends with respect to the periodicity in these profiles which correspond very well with those observed in the grinding experiments.
  - The simulations are helpful in establishing the relations between machine behaviour and process variables on the one hand and the achievable part roughness on the other.

---

## References for chapter 2.

Andrea J., 1986, "Mass production of diffraction-limited replicated objective lenses for compact disc players", SPIE 645, pp. 45-48.

Batheja C.P., 1977, "An Enveloping Profile Approach for the Generation of Ground Surface Texture", Ann CIRP, Vol.25/1, pp. 333-227.

Buttery T.C. and Hamed M.S., 1978, "The Generation of random Surfaces Representative of Abrasion", J. Mech. Eng. Sci., Vol.20, No.3, pp. 133-141.

Chetwynd D.G., 1986, "Stochastic Methods and Engineering Surfaces", in Lecture Notes in Control and Information Sciences Vol.79: Signal Processing for Control, pp. 339-357., edited by K. Godfrey, Springer.

Franse J. and de Jong G.J., 1987, "Roughness Generation in Precision Grinding of Small optical Surfaces", SPIE 803, pp.43-52.

Hamed M.S., Whitehouse D.J. and Buttery T.C., 1978, "Random Surface Generation, An Integrated Approach", Ann. CIRP, Vol.27/1, pp. 499-504.

Hasegawa M., 1980, "A Statistical Analysis of Dressing Characteristics on the Ground Surface Roughness Generation", Int. J. of Mach. Tool Des. Res., Vol.20, pp.275-285.

Hasegawa M., 1981, "Order Statistical Approach to Ground Surface Generation", Trans ASME, J. Eng. for Ind., Vol.103, pp. 22-32.

Konig W. and Steffens K., 1982, "A Numerical Method to Describe the Kinematics of Grinding", Ann. CIRP, Vol.31/1, pp. 201-204.

Matsui S. and Tamaki J., 1979, "The role of Elastic and Plastic Behaviors of Grain and Work in Grinding", Techn. reports, Tohoku Univ., Vol.44, No.2, pp. 303-316.

Pandit S.M. and Sathyanarayanan G., 1982, "A Model for Surface Grinding Based on Abrasive Geometry and Elasticity", J. Eng. for Ind., Vol.104, pp.349-357.

---

Pandit S.M. and Sathyanarayanan G., 1984, "Data-Dependent Systems Approach to Surface Generation in Grinding", *J. Eng. for Ind.*, Vol.106, pp. 205-212.

Pandit S.M., 1986, "Prediction of Surface Roughness and Wavelength with Progress of Cut in Grinding", *Wear*, Vol.108, pp. 81-95.

Sayles R.S. and Thomas T.R., 1976, "A Stochastic Explanation of Some Structural properties of a Ground Surface", *Int. J. Prod. Res.*, Vol.14, No.6, pp. 641-655.

Steffens K., 1983, "Closed Loop Simulation of Grinding", *Ann. CIRP*, Vol.32/1, pp. 255-259.

Suto T. and Sata T., 1981, "Simulation of Grinding Process based on Wheel Surface Characteristics", *Bull. Jap. Soc. of Prec. Eng.*, Vol.15, No.1, pp. 27-33.

Thomas T.R., 1982, "Rough Surfaces", Longman Group Ltd, Essex, U.K.

Whitehouse D.J., 1978, "Surfaces - A Link Between Manufacture and Function", *Proc. Inst. Mech. Eng.*, Vol. 192, pp. 179-188.

Yossifon S., 1982, "The Surface Roughness Produced when Austenitic Stainless Steel is Ground by Alumina Wheels", *Ann. CIRP*, Vol.31/1, pp. 225-228.

Zwiers R.J.M. and Dortant G.C.M., 1985, "Aspherical lenses produced by a fast high-precision replication process using UV-curable coatings", *Applied Optics*, Vol. 24, pp. 4483 ev.

### 3. Mechanical model of the ductile to brittle transition.

#### 3.1. Introduction, the cracking threshold load concept.

In this chapter, the deformation and cracking phenomena observed in single point indentation of glass using diamonds are discussed. A mechanical model describing the relations between load, grain geometry, elastic-plastic deformation and cracking of the glass is presented. In indentation and sliding experiments (Fig. 3.1), the normal load (denoted by  $F$  in indentation,  $F_N$  in sliding) on the indenter is controlled, the depth of penetration into the material is not.

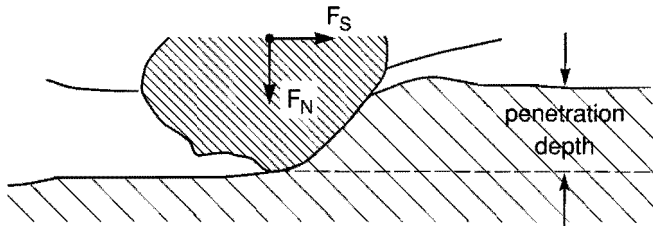


**Fig. 3.1** *In indentation and sliding, the controlled boundary condition is the normal force on the indenter.*

The deformation and cracking behaviour is governed by the stress field in the indented material, which for a given grain geometry and friction coefficient, follows from the load upon the indenter. In grinding, the grinding grains are contained in a binder that has a lower rigidity than the grains and the glass.

Although the machine tool slide is given a fixed displacement (infeed) in precision contour grinding (Fig. 3.2), the compliance of the binder and the machine tool components results in deflections due to the pressure generated in the contact area, in other words due to the forces on individual grains (see chapter 4). The situation in grinding is therefore very similar to indentation and sliding. The purpose of the current study is to establish a model for the cracking phenomena in indentation. Such a model is also applicable to sliding and grinding, since although



in these situations the imposed horizontal velocity will alter the stress field, the fracture criterion can still be applied to such a stress field. In precision contour grinding, the heat input is low enough to prevent material melting/softening, as sometimes observed in less subtle grinding regimes.

For a given grain geometry, friction coefficient and material properties such as the flow stress ( $\sigma_n$ ) in von Mises yield criterion, the modulus of elasticity ( $E$ ), Poisson's ratio  $\nu$  and the critical stress intensity factor ( $K_{Ic}$ ), the mechanical model should predict the threshold load ( $F_{thr}$ ) at which cracking of the glass occurs.

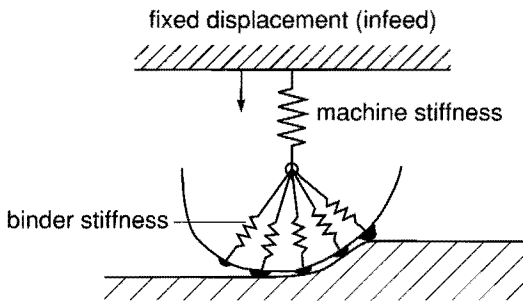


**Fig. 3.2.** *The machine tool slide is given a fixed infeed, but the pressure distribution in the contact area is governed by the load per grain and the compliance of the wheel, workpiece and machine tool.*

In the following paragraph, a survey of the literature on glass cracking phenomena under spherical and conical indenters will be presented. After that, attention is focussed on current experimental and theoretical work in indentation and sliding for conical indenters comparable in size to grinding grains. The experiments were carried out using soda-lime and boro-silicate glass. The plastic deformation of these amorphous glasses during indentation is reasonably continuous and so a continuum mechanics approach is appropriate. Some optically interesting materials like crystalline fused silica exhibit strong densification and inhomogeneous deformation. A continuum mechanics approach seems inappropriate for these materials, and they were excluded from the present study.

---

## 3.2. Survey of literature on indentation induced cracking of glass.

Sharp indenters such as faceted diamonds used in Vickers or Knoop hardness testers and conical indenters, cause significant plastic deformation. An indenter is called blunt if the indentation is mostly elastic in nature up to the point at which cracks initiate. The classic example of a blunt indenter is that of a large spherical indenter (diameter order of cm) in an elastic contact situation (Hertz's contact). The deformation and cracking phenomena under blunt and sharp indenters are notably different (Ostojic 1987). They will be described briefly and the question of whether to consider a given indenter as blunt or sharp will be addressed.

### 3.2.1. Sequence of cracking with blunt indenters.

Using large spherical indenters (radii in the cm range) on glass, the stresses in the glass can be described by the elastic Hertz solution (Hertz 1881, 1895, also Timoshenko, 1970). After initial contact, compressive stresses develop under the indenter. Tensile stresses arise at the contact perimeter, and (of much lower magnitude) deep under the surface along the axis of symmetry. At a threshold load  $F_{thr}$ , cone cracks initiate at the perimeter of contact (Fig. 3.3). They extend in such a direction as to avoid the compressed region under the indenter. If plastic flow occurs, it will be in a completely contained cavity under the surface. During unloading, the cracks tend to close. Small mismatches prevent this from happening completely.

If indentations are done using spherical indenters with smaller and smaller radii, the deformation and cracking pattern gradually changes to that observed under sharp indenters.

Peter (1964) observed three regions in his experiments with spherical steel indenters on glass. When using indenters with radii ( $R$ ) larger than  $170 \mu\text{m}$ , diverging cone cracks were observed. In the second region ( $50 \mu\text{m} \leq R \leq 170 \mu\text{m}$ ), the region under the indenter reached the plasticity limit, the cone cracks became more convergent. Using even smaller radii, the whole area around the indenter became plastic and crack formation set in from the boundary of the plastic zone and the crack patterns become similar to those described in section 3.2.3 for indentation with sharp indenters. The boundaries of the regions mentioned in general depend upon the elastic properties, the flow stress ( $\sigma_n$  as in von Mises yield

criterion) and the fracture stress ( $\sigma_{fr}$ =strength in uniaxial tension) of the materials in contact.

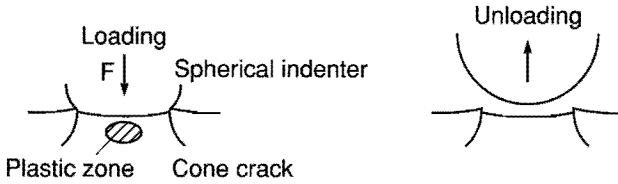


**Fig. 3.3** *During the loading phase of indentation with a blunt indenter, cone cracks may initiate. The plastic zone stays subsurface.*

Obviously, for precision grinding, where grains with diameters typically up to 50  $\mu\text{m}$  are used, the relevant indentation and sliding tests are those using sharp indenters. However, before concentrating on these, a so called size effect observed with spherical indenters has to be discussed because it underlies the idea that a fracture mechanics cracking criterion should be used to predict the threshold load for cracking.

### 3.2.2. The size effect in indentation.

In 1881 Hertz formulated his solution for the elastic stress field under a spherical indenter. Using it, the maximum tensile stress ( $\sigma_{tmax}$ ) at the perimeter of the contact zone can be calculated from

$$\sigma_{tmax} = \frac{(1-2\nu) \cdot p_0}{3} \quad \{3.1\}$$

where  $p_0$  is the maximum pressure in the contact area of radius  $a$ , and  $F$  is the total load:

$$p_0 = \frac{3 \cdot F}{2 \cdot \pi \cdot a^2} \quad \{3.2\}$$

$$a = \left[ \frac{3 \cdot F \cdot R}{4} \cdot \left( \frac{1 - \nu_g^2}{E_g} + \frac{1 - \nu_i^2}{E_i} \right) \right]^{\frac{1}{3}}$$

Assuming the fracture stress ( $\sigma_{fr}$ ) of the material to be a material property (constant value) and setting  $\sigma_{tmax} = \sigma_{fr}$  as a fracture criterion leads to a predicted threshold limit ( $F_{thr}$ ) according to Hertz's formulas of

$$F_{thr} = \frac{9 \cdot \pi^3 \cdot \sigma_{fr}^3}{2 \cdot (1 - 2 \cdot \nu_g)^3} \cdot \left[ \frac{1 - \nu_g^2}{E_g} + \frac{1 - \nu_i^2}{E_i} \right]^2 \cdot R^2 \quad \{3.3\}$$

Here,  $R$  is the indenter radius,  $E$  and  $\nu$  the moduli of elasticity and Poisson's ratios of the materials in contact (indices  $g$  and  $i$  for glass and indenter). The assumption that  $\sigma_{fr}$  is constant is valid for cases in which the stresses are (almost) uniform over the preexisting flaws and the stress field extends over a considerable region, many times larger than the preexisting flaw size. In 1891, Auerbach experimentally determined threshold loads in indentation tests using a variety of indenter radii. Instead of a quadratic relation between  $F_{thr}$  and  $R$  as predicted by eq. {3.3} he found  $F_{thr}$  to be proportional to  $R$ .

$$F_{thr} = C \cdot R \quad \{3.4\}$$

Relation {3.4} is known as Auerbach's law. If it is used in conjunction with eq. {3.3}, so  $\sigma_{tmax} = \sigma_{fr}$  is taken as fracture criterion, it implies that the apparent fracture stress of the material as calculated from eq. {3.3} increases if the indenter becomes smaller (size effect). This can also be seen in Fig. 3.4, reproduced from an article published in 1956 by Tillet.

In Fig. 3.4, it can be seen that for (steel) indenters with radii larger than 3.5 cm, the apparent fracture stress ( $\sigma_{fr}$ ) is constant. In this region, the threshold load ( $F_{thr}$ ) is proportional to  $R^2$ , in agreement with eq. {3.3}. Using smaller radii, Auerbach's law (eq. {3.4}) is valid and the apparent fracture stress  $\sigma_{fr}$  increases strongly with decreasing indenter radius.

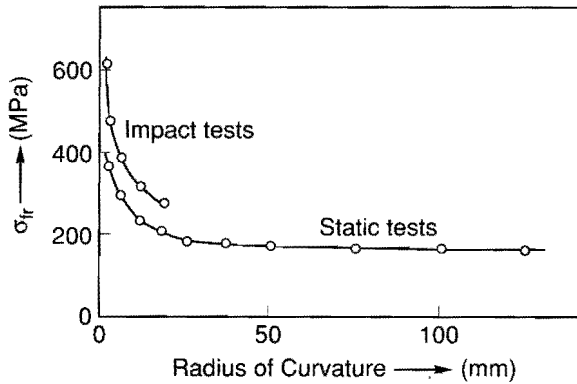


**Fig. 3.4** Apparent fracture stress ( $\sigma_{fr}$ ) in indentation tests, using spherical indenters with different radii (after Tillet, 1956).

Roesler (1956) showed that Auerbach's law can be explained if the strain energy stored in the material under the indenter is compared to the surface energy needed for the generation of cone crack surfaces (Fig. 3.3).

The conclusion from the experimental and theoretical work regarding size effects in fracture phenomena is that for small sharp indenters, a tensile stress magnitude in the material alone is not a suitable fracture criterion.

In addition, the elastically stored energy in the tensile region should be considered (fracture mechanics approach).

In the next section the phenomena in indentation using sharp indenters will be discussed. In section 3.2.4 the stress field under sharp (conical) indenters will be analyzed in more detail and in section 3.2.5 the fracture mechanics approach to cracking will be discussed.

### 3.2.3. Crack formation with sharp indenters.

The literature on crack formation in indentation testing is quite extensive. Since there are a number of recent good review articles (Ostojic 1987, Lawn 1975, Cook 1990), only the points of particular interest will be described in detail.

Different crack types have been observed to form either during the loading or the unloading phase of the indentation (Fig. 3.5).

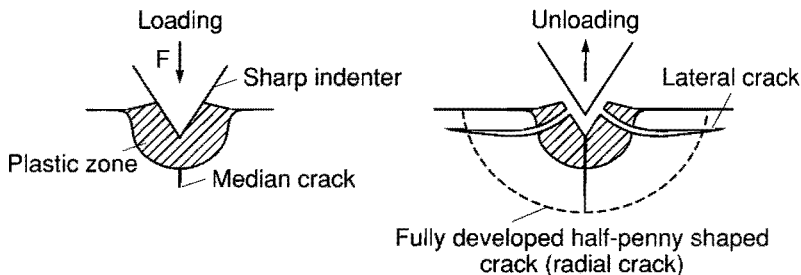


Fig. 3.5 Under sharp indenters, median, radial and lateral cracks are observed.

Cracks that are observed at the surface to run radially with respect to the center of the contact zone are called radial cracks. Cracks that initiate under the indenter and run in the depth direction of the indented material are called median cracks. Finally, another crack system is often reported, consisting of cracks running almost parallel to the surface. These are generally called lateral cracks.

There is general consensus on the fact that radial and median cracks occur at lower threshold loads than lateral cracks. Lateral cracks are consistently reported to occur during the unloading stage of the indentation test.

In the main body of the existing literature, the crack patterns are observed by looking at the surface after the indentation test has been completed. In that case, the median and radial cracks are often observed to be connected, and the sequence of events remains unclear.

It is very difficult to determine whether median cracks initiate during the loading or the unloading stage of the indenter even if glass is tested and the contact site is observed in-situ from the underside of the specimen.

In the literature, practically all tests involving a sharp indenter are done using the four sided pyramidal Vickers indenter. However, for a Vickers indenter, the angle included between opposing planes is  $136^\circ$ . Geometrically speaking, the Vickers indenter is therefore quite blunt compared to typical grinding grains. For grinding, it is important to know the influence of the geometry of the grinding grain on the threshold load as well.

Indentation tests are often used to determine material properties such as the hardness and the critical stress intensity factor  $K_{Ic}$ . There is a large variance in the fracture toughness data for nominally the same glasses reported in the literature. In prior experiments (Donkelaar 1989), it was found that this is probably due to the fact that the procedure to arrive at the  $K_{Ic}$  value involves measuring the length of the radial cracks after unloading. It was found that the time after unloading before the measurement is made (up to 24 hours) is important, since the cracks grow during this period. Furthermore, doing the test in different environments resulted in other values for  $K_{Ic}$ .

Smith et. al. (1981) compared  $K_{Ic}$  values obtained from indentation tests with those measured in standard double cantilever beam experiments. It was found that the values obtained by indentation testing were typically 30 % higher than with conventional tests for glasses containing substantial amounts of network modifiers. For silica rich glasses, the differences were even larger. Furthermore, the ranking of the glasses obtained by the different methods did not agree.

While the  $K_{Ic}$  values obtained with indentation tests ranged from 0.41 to 3.09 MPa $\sqrt{m}$  for the various glasses tested, the values obtained with the double cantilever beam specimen varied only between 0.62 and 0.88 MPa $\sqrt{m}$  for all glasses tested by Smith et. al (1981).

The results obtained with the double cantilever bending tests are considered to be more accurate since total fracture is instantaneous in contrast to indentation cracking where the final crack length involves slow crack growth that is environment dependent.

For the present study, the  $K_{Ic}$  values for the glasses used were determined experimentally from Vickers indentation tests (section 3.3). The values obtained (after 24 hours) were in close agreement with those determined with double cantilever beam tests by Smith (1981), for similar glasses.

### 3.2.4. Elastic-plastic stress field under conical indenters.

The stress field under a sharp indenter is first examined looking at models found in the literature. Although analytic models provide a lot of insight in the phenomena, they do not fully explain them. In particular the initiation of cracks in the residual stress field remains obscure due to the difficulty of calculating the residual field analytically.

The stresses around the tip of a sharp indenter always cause plastic flow. Boussinesq's solution for the elastic stress field under a point load on an infinite half-space predicts tensile stresses under the tip of the indenter and in a shallow region adjacent to it, at the surface. Stress fields under indenters of finite sharpness and a realistic size are more compressive in nature. However, tensile stresses do arise under the indenter as well as at the perimeter of contact and in general reach a maximum at the boundary of the plastic zone. The occurrence of tensile stress regions is not limited to the loading stage of the indentation test.

During the unloading stage, the material in the plastically deformed zone is compressed by the surrounding elastic region and tensile stresses occur once more at the boundary between these regions (residual stresses).

It is apparent that plasticity cannot be neglected for the size of indenters of interest for grinding. For indentation, an analytical approximation by Johnson (1985) can be used to estimate the elastic-plastic stress field around such an indenter. The situation is indicated in Fig. 3.6.

The indenter is supposed to be embedded in a fully plastic semi-hemispherical core (radius  $a$ ) of material. In this region, the pressure is (approximately) hydrostatic. The hydrostatic core is surrounded by a semi-hemispherical plastic zone ( $a \leq r \leq c_p$ ), which in turn is supported by an elastic region.

Johnson's solution is based on the analysis of Hill (1950) for the stresses around a hemispherical cavity expanding plastically in an infinite elastic medium due to internal hydrostatic pressure. The analytical solution for this case is possible because of the symmetry of the problem and the simple form of the plastic region.



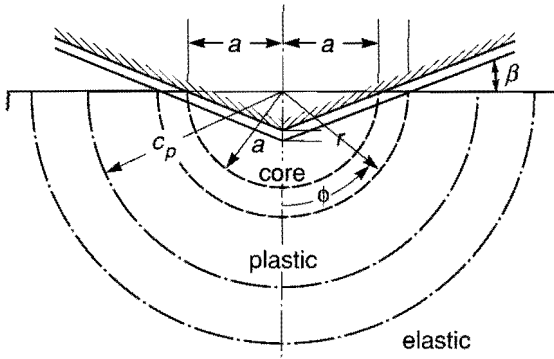


**Fig. 3.6** Spherical cavity model to calculate the elastic-plastic stresses under a sharp indenter (after Johnson, 1985).

The stresses  $\sigma_r$  and  $\sigma_\phi$  in the plastic and elastic regions are:

$$\begin{aligned}
 \text{Plastic zone } (a \leq r \leq c_p): \quad & \sigma_r = \sigma_\beta \left[ -2 \cdot \ln \left( \frac{c_p}{r} \right) - \frac{2}{3} \right] \\
 & \sigma_\phi = \sigma_\beta \left[ -2 \cdot \ln \left( \frac{c_p}{r} \right) + \frac{1}{3} \right] \\
 \text{Elastic zone } (r \geq c_p): \quad & \sigma_r = -\frac{2}{3} \cdot \sigma_\beta \cdot \left( \frac{c_p}{r} \right)^3 \\
 & \sigma_\phi = \frac{1}{3} \cdot \sigma_\beta \cdot \left( \frac{c_p}{r} \right)^3
 \end{aligned} \tag{3.5}$$

The (approximately) hydrostatic pressure ( $p$ ) in the core region ( $r \leq a$ ) is:

$$p = \frac{2 \cdot \sigma_\beta}{3} \cdot \left[ 1 + \ln \left( \frac{E \cdot \tan(\beta)}{3 \cdot \sigma_\beta} \right) \right] \tag{3.6}$$

where  $\beta$  is the angle indicated in Fig. 3.6 ( $\beta$  is larger for sharper indenters). Johnson (1985) argues that the load on the indenter ( $F$ ) at a given pressure  $p$  in the hydrostatic core is approximately:

$$F = \pi \cdot a^2 \cdot \left( p + \frac{2}{3} \cdot \sigma_f \right) \quad \{3.7\}$$

With these formulas, for a given  $\sigma_f$  and  $\beta$ , the pressure in the core region  $p$  may be calculated from eq. {3.6}, next  $a$  can be determined from eq. {3.7} and the size of the plastic zone  $c_p$  follows from:

$$\left( \frac{c_p}{a} \right)^3 = \frac{E \cdot \tan(\beta)}{6 \cdot \sigma_f \cdot (1-\nu)} + \frac{4 \cdot (1-2\nu)}{6 \cdot (1-\nu)} \quad \{3.8\}$$

The stress  $\sigma_\phi$  in the material, along the line coinciding with the centerline (axis of symmetry) of the indenter may cause median cracking. This stress has been calculated for different loads  $F$  (Fig. 3.7) and different indenter geometries (angles  $\beta$ , Fig. 3.8).

From Fig. 3.7 and Fig. 3.8, it is evident that  $\sigma_\phi$  is compressive in the plastic zone, reaches a maximum tensile value equal to  $\sigma_f/3$  and decays to zero in the elastic region further down under the surface. The discontinuity in the stress profile at the boundary of the plastic zone clearly is a result of the model assumptions (ideal-plastic material within the plastic zone, linear elastic elsewhere). In reality, a smoother stress profile can be expected.

The formulas {3.5} reflect the assumption of a cavity expanding plastically in an infinite elastic medium through the predicted similarity of the stress profile along the axis of symmetry and along the surface.

This model can therefore not predict whether radial cracks along the surface will appear before median cracks, and the residual stresses cannot be compared with those during the loading stage.

Chiang, Marshall and Evans (1982) extended the spherical cavity model to approximate the effect of the free surface. The procedure is based on work published in 1936 by Mindlin.

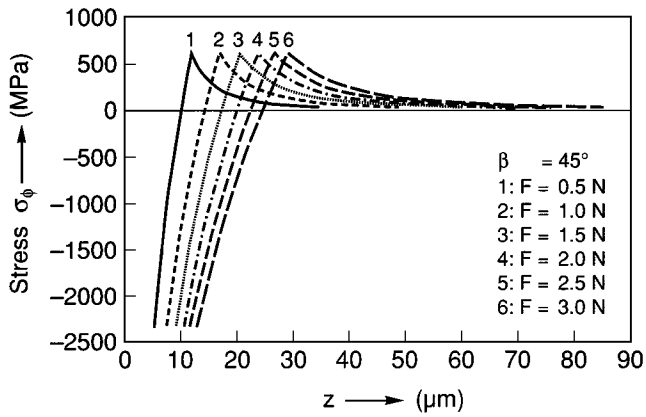


**Fig. 3.7** The stress  $\sigma_\phi$  along the axis of symmetry under a sharp indenter at different loads. (Spherical cavity model).

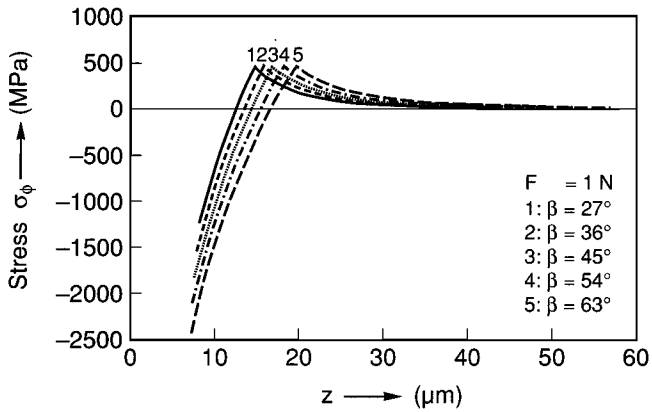


**Fig. 3.8** The stress  $\sigma_\phi$  along the axis of symmetry for various indenter geometries at a constant load. (Spherical cavity model).

In essence, the original cavity model of Hill (1950) is used, but subsequently, the infinite solid is considered to be split. This would result in a free surface that is not stress free. Point forces are therefore distributed over the surface to compensate the normal stress acting on this free surface, except in the contact area. In a similar manner, the residual stress field (after unloading the indenter) is estimated. The model predicts that for glass, the residual stresses pertinent to median cracks are lower than those at peak load. For the stresses at the surface leading to radial cracks, the residual stresses were found to be larger than the tensile stresses at peak load.

Although this model is to date the most realistic (almost) analytical representation of the situation, a number of things remain dubious. The superposition of stresses in the elastic-plastic regime is questionable, although the authors do show that the shear stresses in the plastic zone are not altered much. The indenter geometry is taken into account by a similar parameter as  $\beta$  in the spherical cavity model and by the distribution of point forces in the calculation of the residual stresses.

To calculate the stress field using the model by Chiang et.al. (1982) requires a significant amount of numerical integration. Also, in view of the approximations in the model, it was decided to evaluate the stress fields during indentation and unloading with finite element calculations instead. Before reporting the results of these calculations, the choice of a suitable fracture criterion to be used in conjunction with the stress calculations will be discussed in the next section.

### 3.2.5. Failure criteria for cracking.

If a large volume of a brittle material is stressed in uniaxial tension, a critical value of the (tensile) stress is an adequate failure criterion (Tangena 1989). The presence of holes, corners and other irregularities leads to local stress concentrations. If the ratio of the local and nominal stress (stress concentration factor) is known, the maximum principal tensile stress criterion may still be applied. The same criterion can also be applied in case the material subjected to a multiaxial stress state. Griffith (1920) calculated the maximum tensile stress generated around a hair-like crack in a plane stress state using an elastic solution obtained by Inglis in 1913. The maximum tensile stress at the crack tip was found to depend on the magnitude of the nominal stresses and the crack orientation with respect to these stresses.

If  $\sigma_{ii}$  and  $\sigma_{jj}$  are the nominal principal stresses in the plane of the crack, (indices  $i,j=x,y,z$  depending on the orientation of the global coordinate system with respect to the crack and the particular plane considered), and  $\sigma_f$  is the fracture stress of the material, the fracture stress cracking criterion for multiaxial stress states takes the form (Orowan 1949):

$$\text{For } 3 \cdot \sigma_{ii} + \sigma_{jj} \geq 0, \text{ fracture occurs if } \sigma_{ii} - \sigma_f > 0 \quad \{3.9\}$$

$$\text{For } 3 \cdot \sigma_{ii} + \sigma_{jj} \leq 0, \text{ fracture occurs if } (\sigma_{ii} - \sigma_{jj})^2 + 8 \cdot \sigma_f \cdot (\sigma_{ii} + \sigma_{jj}) > 0$$

A failure stress cracking criterion can only be applied if there is enough elastically stored energy in the region stressed in tension to extend the crack. (The elastic energy released upon cracking has to provide the surface energy needed for crack surface generation). When the nominal stress field is non-uniform and the tensile region is small, this may not be the case anymore.

This leads to the size effect observed in indentation that was discussed in section 3.2.2. An appropriate cracking criterion that takes this into account is the energy release rate ( $G_c$ ) or alternatively the stress intensity factor ( $K_c$ ). They are related (for a plane strain tensile cracking mode) by (Rossmannith 1982):

$$G_c = \frac{(1-\nu^2) \cdot K_c^2}{E} \quad \{3.10\}$$

The energy release rate failure criterion states that failure will occur if the elastically stored energy, released when the crack extends, is enough to compensate for the surface energy needed to create the crack surfaces (provided that there is little to no plastic deformation associated with crack extension).

In an elastically stressed section of material, local flaws act as stress raisers. The elastic stress field around a sharp crack tip (Fig. 3.9) has a singularity. The severity of this singularity depends upon the crack geometry and the material.

This is expressed by the value of the so called stress intensity factor  $K$  in the formulas for the stress components  $\sigma_{ij}$  in the vicinity of the crack (Rossmannith 1982):

$$\sigma_{ij} = \frac{1}{\sqrt{2\pi r}} \cdot [K_I \cdot f_{ij}^I(\theta) + K_{II} \cdot f_{ij}^{II}(\theta) + K_{III} \cdot f_{ij}^{III}(\theta)] \quad \{3.11\}$$

Here,  $r$  is the radial coordinate with its origin at the crack tip and  $f_{ij}(\theta)$  is an angular function only.

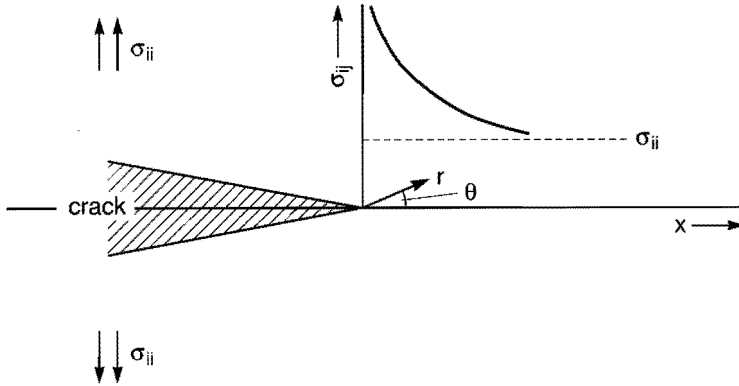


**Fig. 3.9** The stress components at a very sharp crack tip go to infinity (if no plasticity occurs).

The index I, II and III indicates a mode I (tension), II (in plane shear) or III (out of plane shear) loading situation (Fig. 3.10).

The median and radial cracks that we are concerned with are formed by maximum principal stresses in mode I configurations. If we consider a flaw with a known geometry in a nominal stress field (as if no flaw were present) the stress intensity factor  $K_I$  at the crack tip may be calculated.

The criterion for cracking is that  $K_I$  at the crack tip becomes larger than a "material constant" called the critical stress intensity factor ( $K_{Ic}$ ).

As stated before, the value of the stress intensity factor ( $K_I$ ) at the crack tip is not only a function of the stress in the vicinity of the crack but also depends on the crack geometry. The formulas and the differences between the  $K_I$  factors for different common crack geometries are discussed in Appendix 3.1.

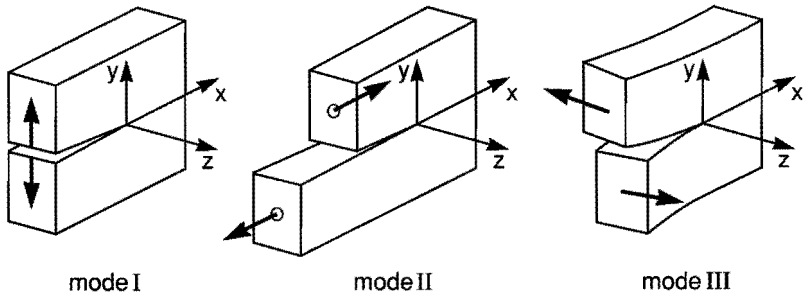


Fig. 3.10 The three fundamental modes of crack loading.

Lawn and Evans (1977) used the stress intensity factor approach to estimate the threshold load for median cracking. They first applied a model similar to the spherical cavity model to calculate the stresses along the axis of symmetry of a Vickers indenter. As a first approximation, the tensile stress under the indenter was assumed to decay linearly from the boundary of the plastic zone where the stress reaches its maximum. Furthermore, a penny-shaped crack was assumed to be present, its center located at the position of maximum stress. The stress intensity factor can now be evaluated (Paris 1965) using eq. {A3.1.1} from Appendix 3.1.

They found the following expression for the threshold load ( $F_{thr}$ ) for median cracking (at peak load)

$$F_{thr} = C \cdot \frac{K_c^4}{H^3} \quad \{3.12\}$$

where  $C$  is a constant depending on the indenter geometry,  $K_c$  is the critical stress intensity (in  $\text{MPa}\sqrt{\text{m}}$ ) and  $H$  the hardness of the material (in  $\text{MPa}$ ). The value of  $C$  varies gradually with the sharpness of the indenter and so it can be expected that the values of  $K_c$  and the hardness (which can also be interpreted as a measure of the flow stress) have a dominant influence upon the cracking threshold load.

Chiang, Marshall and Evans (1982) applied the same approach as Lawn and Evans, but took the non-linear course of the stress profile calculated in a companion paper (1982) into account, for median crack initiation. Like Lawn and Evans, they assumed an axial-symmetric penny shaped crack to be present at the site of the maximum in the stress profile. They once again found a relation similar to eq. {3.12}. The influence of the assumptions regarding the shape and size of the assumed pre-existing flaw on the  $K_I$  values calculated is not discussed in detail in the literature quoted.

### 3.2.6. Conclusions from the literature studied and remaining problems.

To use indentation results as a basis to understand the ductile to brittle transition in grinding, the following questions have to be answered with more certainty than possible on the basis of the literature available:

- What is the sequence of cracking events in indentation of glass with sharp indenters (radial, median and lateral cracks)?
- In what stage of the indentation test (loading, unloading) do these cracks occur?
- Does the environment have an influence on the threshold load for cracking? (If different environments give other values for  $K_{Ic}$ , and  $K_{Ic}$  is subsequently used in a model to predict the threshold load, then the threshold load would become environment dependent).
- What is the influence of the indenter geometry on the threshold load for cracking of glass?
- What are the stresses in the vicinity of the indenter during the loading and especially the unloading phase of the indentation test?
- Is the stress intensity factor  $K_{Ic}$  an appropriate criterion for cracking using sharp indenters?
- What is an appropriate  $K_I$  calculation method for a given stress profile?
- How sensitive is the  $K_I$  calculation method with respect to the assumptions regarding the flaw (crack pre-cursor) geometry and size?

It was decided to address these questions by indentation experiments (section 3.3), finite element calculations (section 3.4) and a sensitivity analysis of the stress intensity calculation method (Appendix 3.1).



### 3.3. Indentation experiments.

To answer the questions presented in the former section, experiments were performed in laboratory air (relative humidity  $\approx$  50%), deionized water and in krytox (a perfluoropolyether containing only 7  $\mu\text{g/ml}$  of water). Tests were done using conical indenters with apex angles of 80°, 100°, 110°, 120°, 130°, 140°, 150° and 160° and Vickers indenters. The load on the indenters could be varied between 0.05 N and 100 N.

The indentation tests reported here were done using an optical Natron-Silicate glass known as B 270 and a Boro-Silicate glass known as FCA 8866. The chemical composition (weight percent) of these glasses is given in the following table, apart from traces of ZnO, PbO and BiO present in both.

	SiO <sub>2</sub>	Na <sub>2</sub> O	K <sub>2</sub> O	CaO	B <sub>2</sub> O <sub>3</sub>	Al <sub>2</sub> O <sub>3</sub>
B 270	70	8	8	9		
FCA 8866	66	0.5	8		21	3

Initial tests were done on soda-lime glass using conical indenters made of single crystal diamond. It was found that the diamonds had very sharp tips indeed. However, some facetting was noted, probably caused by the non-uniform wear of the anisotropic diamond during the lapping procedure used. To rule out possible biasing of the results by this effect, a second series of indenters were made of polycrystalline diamond. These were found to be rougher than the single crystal diamonds and they have a significant tip radius ( $\approx$  5  $\mu\text{m}$ ). SEM photos of typical indenters can be seen in Fig. 3.11.

Surprisingly at first, the results using corresponding indenters from the two series gave practically identical threshold loads in the indentation tests. The probable explanation is that the cracks initiate from the boundary of the elastic and the plastic zone. This boundary is located some distance away from the indenter surface. Apparently the stress state there is not much influenced by the surface roughness and slight facetting, since the indenter is immersed completely in a plastic zone of nearly semi-hemispherical shape.

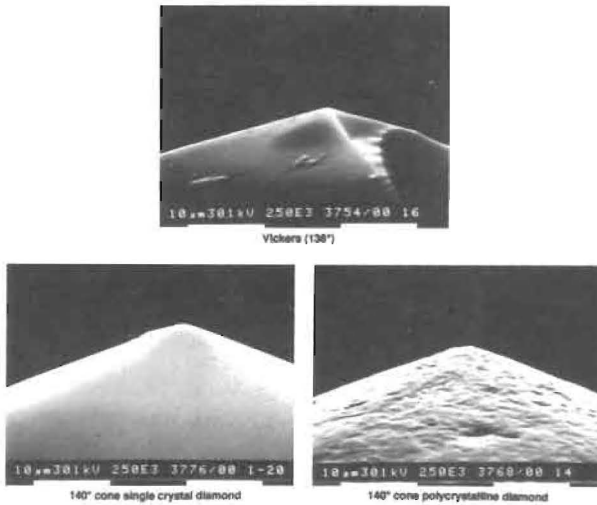


**Fig. 3.11** SEM photos of typical single crystal, polycrystalline and Vickers diamond indenters.

A series of indentation tests was carried out, using a range of loads, to determine the material properties ( $K_{Ic}$  and the Vickers hardness  $H_v$ ) of these materials. Vickers hardness values  $H_v=7000$  MPa and 5500 MPa were found for the B 270 and the FCA 8866 respectively. The  $K_{Ic}$  values were obtained using the procedure described by Lawn and Fuller in 1975. It involves measuring the radial crack length ( $c$ ) after a Vickers indentation test with a maximum load  $F$ . Next  $K_{Ic}$  is calculated from (Lawn and Fuller 1985)

$$K_{Ic} = 0.092 \cdot \frac{F}{c^{3/2}} \quad \{3.13\}$$

However, as Smith (1981) and Donkelaar (1989, 1990) found (section 3.2.3), the values of the measured crack length ( $c$ ) strongly depend on the time after unloading that has passed before the crack length is measured (due to crack growth after unloading). If the crack length values obtained directly after the indentation test are used,  $K_{Ic}$  values of 1.0 and 1.3 MPa $\sqrt{m}$  are found for the B 270 and the FCA 8866. These values are considerably higher than the 0.8 and 1.0 MPa $\sqrt{m}$  obtained when the procedure is applied 24 hours later, which is considered a better procedure. The

$K_{Ic}$  values determined 24 hours after the indentation tests also agree better with the values obtained with the standard double cantilever beam tests for similar glasses reported by Smith (1981), that indicate a  $K_{Ic}$  value of about 0.80 MPa $\sqrt{m}$  for both types of glass.

In view of the above considerations, for B 270, a hardness value of 7000 MPa and a toughness of 0.8 MPa $\sqrt{m}$ , for FCA 8866, a hardness of 5500 MPa and a toughness of 1.0 MPa $\sqrt{m}$  were taken as the material properties of the glasses studied. Using these values, threshold loads for median cracking at maximum loads of 0.02 and 0.12 N are predicted for the two glasses using eq. {3.12}, for indenters with an apex angle of 140°.

The indentation experiments to determine the threshold load for cracking and the sequence of cracking events (Donkelaar 1990) involved indenting 4-sided polished rectangular glass bars. The phenomena in the glass were observed with microscopes, arranged to give a side view, and to look at the area of contact from the underside of the bar, through the glass. The sequence of events described here is typical for glasses with an amorphous structure that do not densify significantly during indentation. These include most optical glasses often used for precision grinding, fused silica excepted. The side view obtained made it possible to draw definite conclusions regarding the sequence of crack formation. Each test, the indentation load was raised to its maximum value in short time, remained constant for 15 seconds and subsequently, the indenter was removed quickly (standard Vickers loading cycles). Starting at low peak loads (0.05 N), increasing the peak load (to 10 N max.) results in:

- Elastic-plastic deformation only.
- Radial (also called Palmqvist) cracks, initiating at the perimeter of contact, during the unloading stage of the indentation test. For the sharper indenters, these cracks occur at lower threshold loads.
- Both median and radial crack vents are observed after unloading.
- Median cracks are formed during the loading stage of the indentation test, sometimes delayed, depending on how much the maximum load is above the threshold load. As long as the load is maintained, the median vent has a contained penny-like geometry. It grows to a half-penny configuration (median/radial crack) during the unloading stage of the indentation.
- Besides the median crack that is formed during the loading stage and that grows toward the surface on unloading (median/radial crack), lateral cracks also occur during the unloading stage.

- At very high loads (also depending on the indenter geometry) the lateral cracks interact with the median/radial crack system and chipping occurs during the unloading stage.

The sequence of events, the different types of cracks observed and the influence of the indenter geometry can be seen in Fig. 3.12 and Fig. 3.13.

It is obvious that the indenter geometry does have a significant influence on the threshold load for cracking. For FCA 8866, the threshold load for radial cracking measured with the sharper indenters is virtually the same.

This is probably due to the roundness of the tips of the polycrystalline indenters used in these tests.

At low loads, the indenters do not penetrate the material very much and the different indenters all start to resemble spherical indenters with about  $5 \mu\text{m}$  tip radius. The higher toughness and the lower hardness of the FCA 8866 glass is reflected in a higher threshold load for median cracking. However, for the threshold load for radial cracking, similar values as for the B 270 glass were found.

The threshold load for a particular crack type had a reasonably well defined value that could be reproduced very well on the same and other specimen, and at various points in time. This leads us to conclude that the cracking phenomena are governed by the mechanics of the indentation process, and not by the random presence of scarce preexisting flaws in the material.

Apparently, flaws are generated by the deformation processes during the indentation test and cracking occurs if the combination of such a flaw and the local stress over the flaw surface becomes critical ( $K_I > K_{Ic}$ ).

The environment was found to influence the threshold load for cracking very little or not at all (in water, the threshold loads were marginally lower).

The length of the cracks directly after initiation (pop-in length) and subsequent crack growth was found to be highly dependent upon the environment. The influence of the environment upon the pop-in length of a crack indicates that the environment has access to the crack precursors, probably diffusion through the plastically deformed zone is relatively easy.

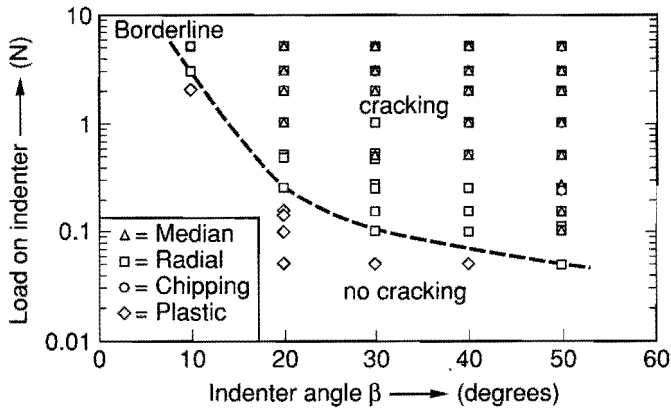


**Fig. 3.12** The crack patterns observed after unloading in B 270 as a function of load and indenter geometry.

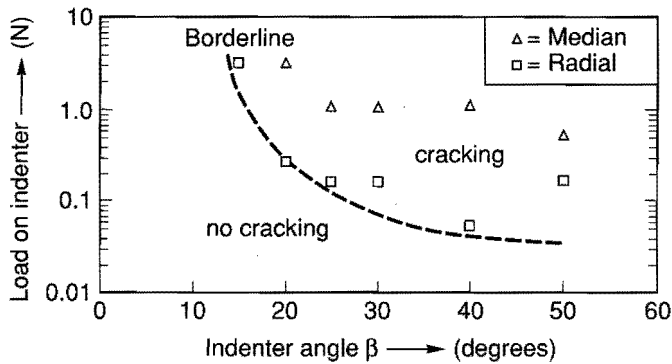


**Fig. 3.13** The crack patterns observed after unloading in FCA 8866 as a function of load and indenter geometry.

In water, the crack growth velocity and final crack length was larger than in laboratory air, in krytox they were lowest. This agrees with the reported lower fracture energy needed for crack propagation for glass in water (Inagaki 1985).

Crack growth was observed to continue for up to 24 hours after the cracks initiated. A noteworthy effect occurred when samples indented in krytox or air were immersed in water after cracks had popped in. The crack growth rate and final crack length in these cases assumed the same values as if the whole test had been performed in water.

Remarkably, if a test was done in krytox or open atmosphere, using a maximum indentation load not much above the threshold load, the cracks would pop-in quite some time after the actual test was finished. The pop-in time depends upon the difference between the maximum indentation load and the threshold load for that particular indenter geometry. This indicates that the time dependent behaviour of the glass has some influence on the residual stress field in the material.

Considering indenters with an apex angle of  $140^\circ$  and comparing the experimental threshold loads for median cracking at peak load (1 and 10 N for B 270 and FCA 8866) with the values calculated using eq. {3.12} (0.02 and 0.12 N respectively) shows that the experimentally determined values are considerably higher. Lawn and Evans already indicated that the model they presented could only be expected to give values that indicate the order of magnitude, in view of the simplifications and uncertainties in the model.

In the model presented in the following sections, some of these shortcomings have been addressed and one may expect that the threshold loads can be predicted somewhat more accurately.

Evidently, a mechanical model for the transition from ductile to brittle material removal should, as a first step, be able to explain the sequence of crack formation observed experimentally. In the following sections such a model will be introduced. The time dependent effects mentioned above are not taken into account in the model presented.

### 3.4. Finite element calculations.

Initial finite element simulations of indentation tests in glass were done with varying mesh sizes and quadrilateral elements with both linear and quadratic base functions to investigate the effects of these parameters on the stresses calculated.

The mesh finally used to model the indentation of glass with sharp indenters consisted of 2300 axial-symmetric first order quadrilateral elements. The calculations were performed using the MARC finite element program (MARC version K4, 1990). The glass was given isotropic properties:  $E=90$  GPa,  $\nu=0.25$ ,  $\sigma_n=1800$  MPa. No strain hardening and no time dependent behaviour was assumed.

The elements in the top surface had a spacing of  $0.2 \mu\text{m}$ , along the first part of the axis of symmetry the element size was  $0.5 \mu\text{m}$ .

Indenters were simulated with apex angles of  $100^\circ$  and  $140^\circ$ , a tip radius of  $0.5 \mu\text{m}$  was modeled.

The effect of friction was investigated by doing simulations without friction and with a Coulomb type friction coefficient  $\mu=0.3$  along the indenter-glass contact surface.

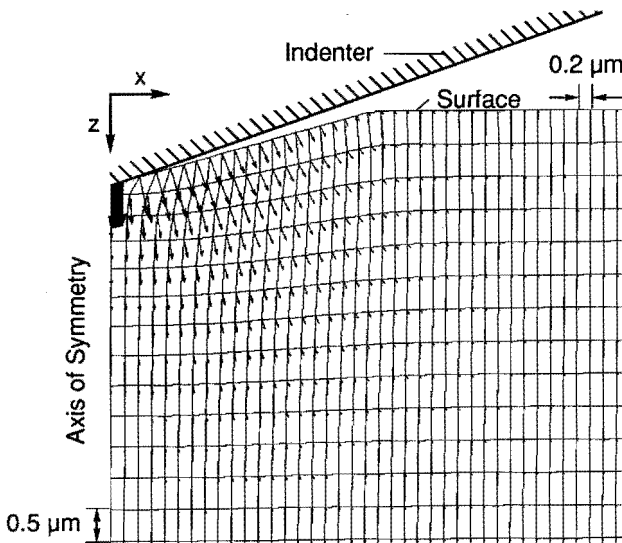


Fig. 3.14 Typical plot of the deformed mesh as the indenter penetrates the material.

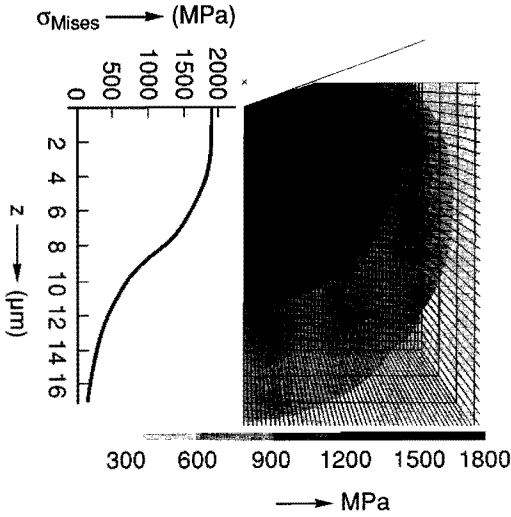


Fig. 3.15 The von Mises stress in the material during the indentation stage

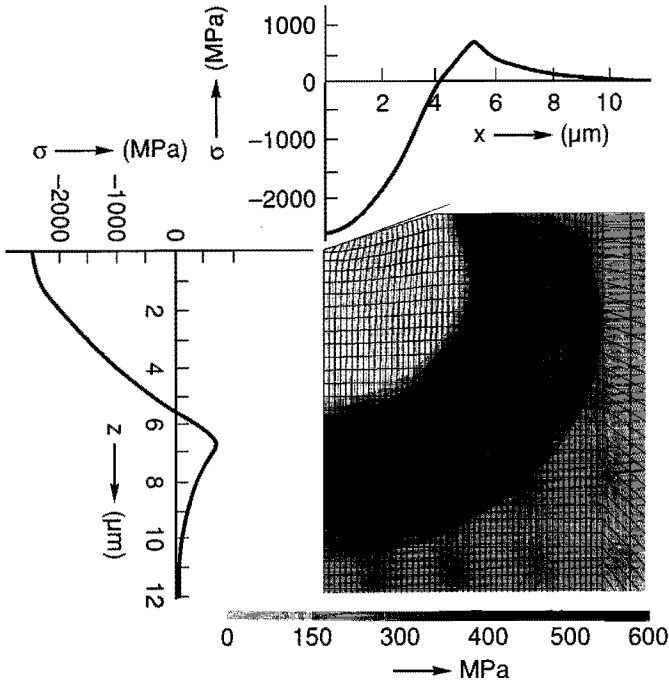
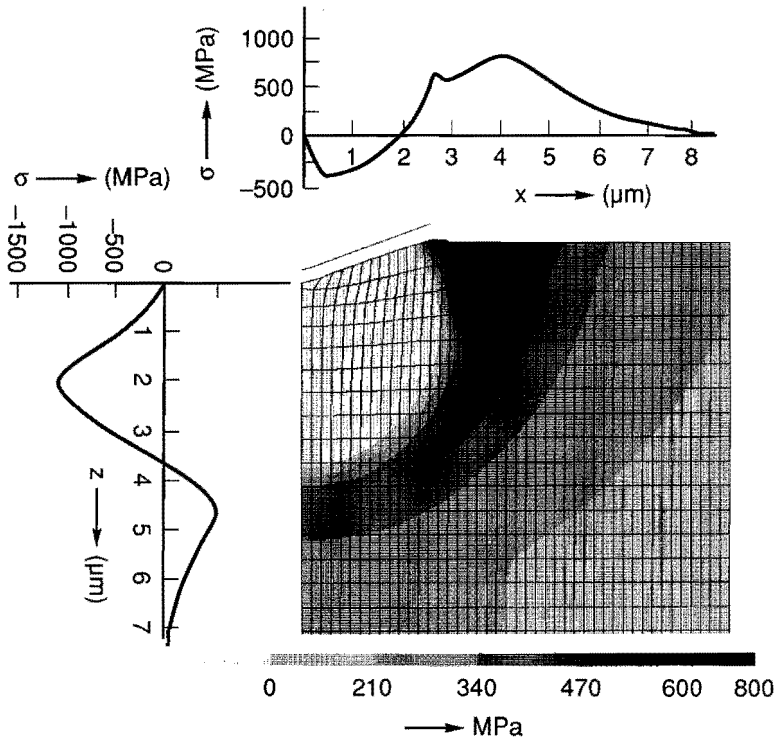


Fig. 3.16 The maximum principal stress contours during the indentation stage.





**Fig. 3.17** Max. principal stress contours after unloading the indenter.

For the sharper indenter geometry modeled, at an indentation depth of 4  $\mu\text{m}$  the distortion of the elements close to the indenter tip became problematic. Residual stresses were calculated by unloading the indenters after indentation to depths of 0.5, 1.0, 1.5, 2.0, 2.5, 3.0, 3.5 and 4.0  $\mu\text{m}$ , which corresponds to an indentation load range of up to 1 N.

Typical plots obtained for the displacement, the von Mises stress and the maximal principal stress during the loading stage of a simulated indentation can be seen in Fig. 3.14, Fig. 3.15 and Fig. 3.16. The maximum principal stress after unloading the indenter can be seen in Fig. 3.17. The indenter modeled in this particular simulation had an apex angle of  $140^\circ$  ( $\beta=20^\circ$ ). A Coulomb type friction coefficient of 0.3 was assumed along the indenter-glass interface in this simulation.

The maximal principal stress reaches an extreme value at the boundary of the plastically deformed region, both under the indenter and along the surface.

This agrees with the results of the analytical models discussed in section 3.2.4.

There are however significant differences in the stress profiles along the axis of symmetry and along the surface. This can be seen (for an indenter with an apex angle of  $100^\circ$ ) in Fig. 3.18 and Fig. 3.19. The node positions of the undeformed mesh and the stresses in the various deformed states were used to compose these graphs.

The differences in the profiles along the axis of symmetry and along the surface reflect the influence of the free boundary, which is not taken into account in the spherical cavity model. In agreement with the analytical model, the numerical results indicate that there is a region close to the indenter tip where the stress state is practically hydrostatic. The values of the hydrostatic pressure can be seen in Fig. 3.18 and Fig. 3.19 ( $\approx 3200$  MPa). In the simulations with an apex angle of  $140^\circ$ , a cavity pressure of 2500 MPa was found.

This agrees qualitatively with the spherical cavity model, eq. {3.6} predicts a larger cavity pressure under a sharper indenter. However, the numerical values for the cavity pressure are significantly lower than the predicted values of 4360 and 3300 MPa for indenters with apex angles of  $100^\circ$  and  $140^\circ$ . This can be explained once again by the free surface effect neglected in the spherical cavity model.

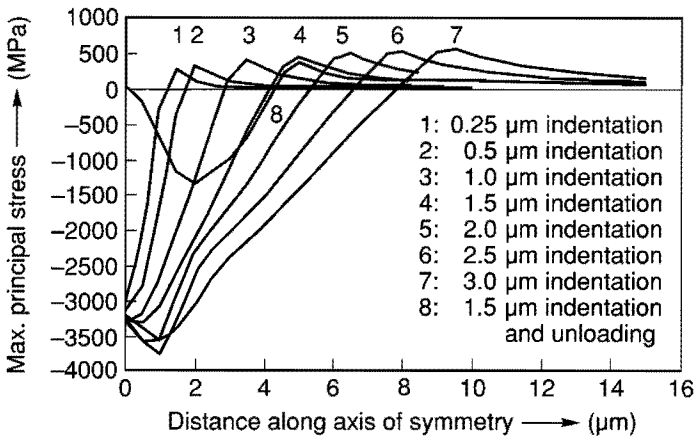


Fig. 3.18 Max. principal stress along the axis of symmetry at different stages of a simulated indentation (Apex angle  $100^\circ$ ,  $\mu=0.3$ ).

This also results in a plastic zone size predicted by the spherical cavity model that is smaller than that found in the finite element calculations.

Finally, the gradients in the stress profiles calculated with finite elements are less steep than indicated by the analytical model, and this will result in significant differences in the stress intensity factor calculations presented later on.

Returning to Fig. 3.18 and Fig. 3.19, three points are noteworthy in these graphs of the maximum principal stress components along the axis of symmetry and along the surface:

- The extreme value of the maximum principal stress under the indenter increases slowly with increasing indentation depth but does so at a faster rate than the extreme value of the surface profile.
- The decay rate of the stress profile along the axis of symmetry is less than that along the surface. With increasing penetration depth, these decay rates in both profiles diminish.
- The residual stress profile (after unloading the indenter) on the axis of symmetry is virtually the same as that during the loading stage. The residual tensile stresses along the surface are larger in magnitude, and extend over a larger region than during the corresponding loading stage.

These effects will be reflected in the results of the  $K_I$  calculations presented in the next section.

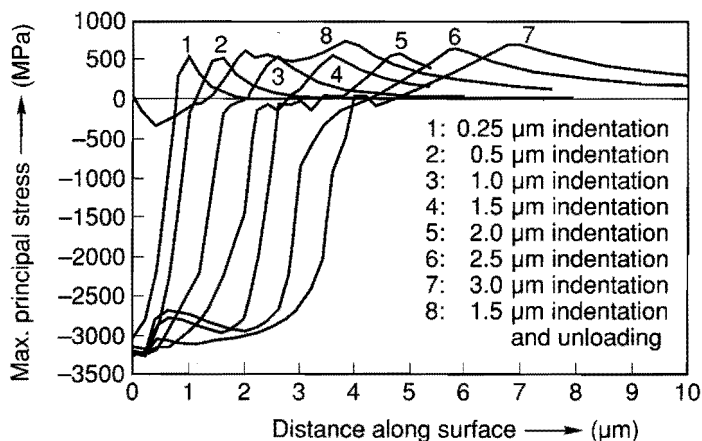


**Fig. 3.19** Profiles of max. principal stress along the surface at various stages of a simulated indentation. (Apex angle  $100^\circ$ ,  $\mu=0.3$ ).

### 3.5. Stress intensity factor ( $K_I$ ) calculations.

#### 3.5.1. $K_I$ calculation method used in this study.

In section 3.2.5, the stress intensity factor  $K_I$  was introduced as a potentially suitable fracture criterion to model indentation and sliding with sharp indenters. It was indicated that the  $K_I$  value calculated in a particular configuration depends on the size, shape and the stress over the preexisting flaw. In Appendix 3.1, the sensitivity of the  $K_I$  values with respect to these assumptions is reported in detail.

In the current investigation, the stress intensity factors  $K_I$  leading to median and/or radial cracking were calculated in the following way:

- The stress profiles along the axis of symmetry under the indenter and along the contact surface were obtained at various stages of the finite element simulation of the indentation test (loading and unloading phase). This allowed to account for plasticity, friction along the indenter, the indenter geometry, and made it possible to calculate the residual stresses in the material after unloading the indenter.
- After the stress profiles had been obtained, two curves were fitted through the profiles, the first describing the stress in the plastic region, the second the stress in the elastic region. The fitting routines were made interactive so that the order of the fitted polynomials and the portion of the data used in the fits could be optimized in an iterative way.
- A hair-like flaw (length  $2 \cdot c = 1 \mu\text{m}$ ) was assumed to be present, positioned symmetrically with respect to the elastic/plastic boundary. This assumption was made after evaluation of the influence of the shape of the flaw and its assumed position on the  $K_I$  values obtained (see Appendix 3.1).
- The  $K_{I,\text{sym}}$  method discussed in Appendix 3.1 was used to calculate  $K_I$  factors by numerical integration of eq. {A3.1.2}. All  $K_I$  values quoted further on in this thesis have been obtained in this manner unless stated otherwise.

As illustrated in Fig. 3.20, the stress state under the indenter, along the axis of symmetry is triaxial compression at the indenter tip. Deeper down, two principal stresses become tensile. In contrast, along the surface only one principal stress of the plane stress state becomes tensile. The biaxial stress state under the indenter results in two equal mode  $K_I$  factors acting upon one flaw. In view of the energy

argument discussed in Appendix 3.1, these have to be combined. Since the two principal stresses and therefore the two  $K_I$  factors are equal in magnitude, the effective  $K_I$  factor under the surface, along the axis of symmetry, should be calculated as

$$K_{I_{\text{effective}}} = \sqrt{2} \cdot K_{I_{\text{individual}}} \quad \{3.14\}$$

In the  $K_I$  values reported later on, this has been taken into account. From the discussion in Appendix 3.1, it is evident that due to the influence of the assumptions underlying the calculations, the absolute values for the stress intensity factors ( $K_I$ ) cannot be expected to be very accurate. (Worst case up to 40% difference, typically less).

However, the deviations are systematic. This means that any trends of the stress intensity factors calculated as a function of load, position and indenter geometry will be assessed correctly. A comparison with the experimental results should at least be in qualitative agreement, and the quantitative comparison should be reasonable.

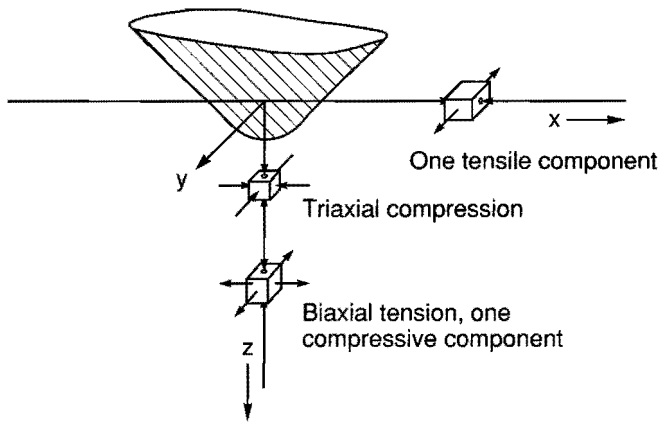


**Fig. 3.20** Characteristics of the principal stress state along the axis of symmetry and along the surface of the glass.

### 3.5.2. Stress intensity factors calculated from FE results.

The stress profiles obtained from the finite element calculations were used to calculate stress intensity factors ( $K_I$ ) in the way described in section 3.5.1.

The  $K_I$  factors during the loading and unloading stages of the indenter with apex angle of 100 degrees and friction coefficient ( $\mu$ ) of 0.3 can be seen in Fig 3.21.

Similarly, Fig 3.22 shows the  $K_I$  factors obtained from the simulations with the blunter indenter (140 degrees apex angle,  $\mu=0.3$ ).

With increasing load (penetration depth), the  $K_I$  factors both along the axis of symmetry and along the surface are seen to increase gradually, as expected.

For the sharper indenter, the  $K_I$  factor along the axis of symmetry is higher than at the surface (over the indentation range from 1 to 4  $\mu\text{m}$ ). With the blunter indenter, the  $K_I$  factors along the axis of symmetry are initially also larger than those along the surface, at higher loads the  $K_I$  factor becomes largest at the surface.

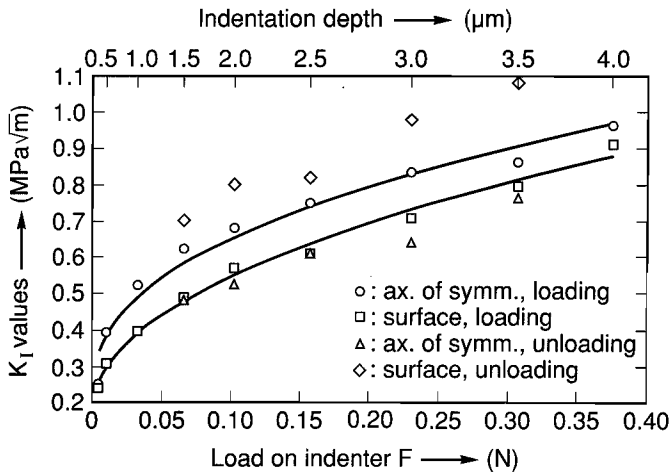


**Fig. 3.21** Calculated stress intensity factor  $K_I$  at various stages of indentation simulations, along both the axis of symmetry and the surface (Apex angle 100°,  $\mu=0.3$ ).

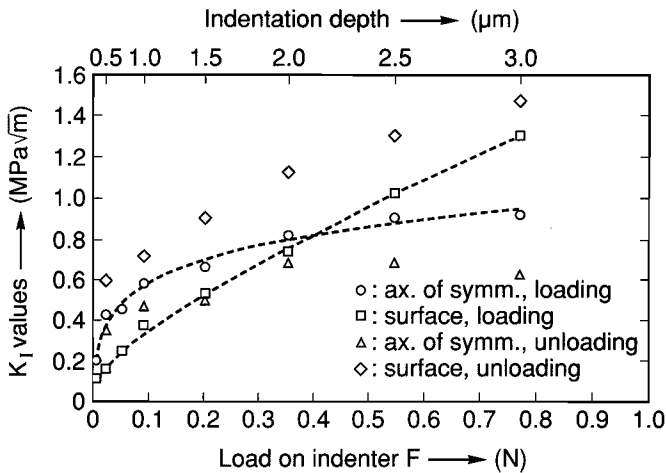


**Fig. 3.22** Calculated stress intensity factors at various stages of indentation simulations for an indenter with  $140^\circ$  apex angle,  $\mu=0.3$ .

Unloading results in a residual stress state very much like that during the loading stage. After unloading, the  $K_I$  factor along the axis of symmetry is less than during the loading phase. At the surface, the  $K_I$  factor increases significantly upon unloading.

### 3.6. Comparison of simulated and experimental results.

The calculated trends shown in Fig. 3.21 and Fig. 3.22 agree with the experimental observations (section 3.3) The radial crack system is activated at the lowest threshold load, before the median and lateral crack systems.

The effect of the indenter geometry on the  $K_I$  factors can be seen in Fig. 3.23. During the loading phase, the stress intensity factor along the axis of symmetry is larger for the sharper indenter.

This agrees with the observed inclination of these indenters to form median cracks during the loading stage at lower threshold loads than blunter indenters.

The  $K_I$  factors at the surface after unloading are calculated to be only marginally higher for the sharper indenter.

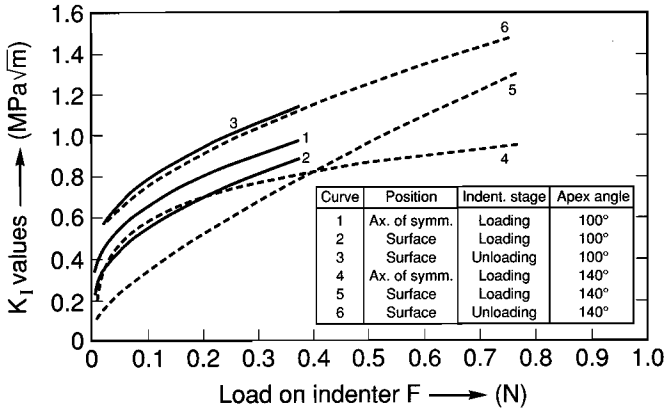


**Fig. 3.23** Effects of the indenter geometry on the calculated stress intensity factors along the axis of symmetry and the surface, during loading and unloading ( $\mu=0.3$ ).

In view of the assumptions in the model, it would be doubtful whether the calculated difference is significant. However, the experiments confirm that for sharper indenters, the threshold load for radial cracking is indeed lower.

Fig. 3.23 can be used to determine the threshold load for cracking, for a material with  $E=90$  GPa,  $\nu=0.25$  and  $\sigma_n=1800$  MPa, in the following way. Start at the vertical ( $K$  value) axis at the  $K_c$  value of the material under consideration. Draw a horizontal line. A vertical line from the intersection of this line with the curve representing a particular type of crack indicates the threshold load for this particular crack system (on the load axis).

Taking  $K_{Ic}$  as  $0.8$  Mpa $\sqrt{m}$ , the calculated threshold load for radial cracking upon unloading is about  $0.1$  N. This agrees very well with the observation on B 270 for the sharpest of the two indenters. For the blunter indenter, the threshold load is underestimated by the simulations in comparison to the experimentally determined value of  $0.25$  N. The threshold loads for median cracking are calculated as  $0.20$  and  $0.35$  N respectively for the sharper and the blunter indenter. These values are close to the experimentally observed values of  $0.25$  N and  $0.50$  N on B 270.



If  $K_{Ic}$  is taken as  $1.0 \text{ MPa}\sqrt{\text{m}}$ , threshold loads of 0.35 N for radial cracking upon unloading and between 0.5 N ( $100^\circ$  apex angle) up to approximately 2 N ( $140^\circ$  apex angle) for median cracking, during the loading phase of the indentation test, are predicted. These values are low compared to the values between 5 and 10 N found experimentally for FCA 8866.

However, the agreement between the experimentally determined values and the calculations is quite good in view of the systematic deviations which are to be expected as a result of the assumptions regarding the length and location of the flaw over which the stress profile is evaluated.

### 3.7. Conclusions

The results of the indentation experiments (section 3.3), the modeling effort (section 3.4 and 3.5) and the comparison of these results discussed in the former sections can be summarized as follows:

- With increasing peak indentation load, the following sequence of events was observed in the two glasses studied:
  - Elastic-plastic deformation only.
  - Radial cracking upon unloading.
  - Mixed radial/median cracking upon unloading.
  - Median cracking upon loading (and radial upon unloading).
  - All of the above, and lateral cracks upon unloading.
- The cracking threshold is reasonably well defined (not a stochastic variable depending upon scarce, randomly present flaws in the material).
- The cracking threshold is considerably higher for blunt indenters compared to sharper indenters.
- Especially close to the threshold load, delayed cracking effects were observed, indicating time dependent mechanical behaviour of the glasses tested. Specimens that did not crack within 24 hours after the test were never observed to have cracked later on.
- The environment was found to have an only marginal effect on the cracking threshold load.
- Environmental effects on crack growth were much more pronounced. Water especially promotes crack growth (speed of propagation and final crack length) and was seen to speed up any time dependent effects (delayed cracking) greatly.

- The stresses along the axis of symmetry at indentation peak load calculated with finite elements correspond reasonably well with those predicted by the analytical models reported in the literature (Chiang 1982, Johnson 1985).  
Discrepancies between the stress profiles calculated with the spherical cavity model and the finite element simulations are due to the effect of the free surface, which is not taken into account in the cavity model.
- The maximum principal stress along the axis of symmetry after unloading was very similar (slightly lower) than that during the loading stage.
- The maximum principal stress at the surface after unloading was somewhat higher, and extends over a much larger region than during the loading stage.
  
- The calculated trends in the stress intensity factor  $K_I$  as a function of load and indenter geometry, and the predicted sequence of cracking correspond well with the experimental results.
- The calculated cracking threshold loads agree reasonably well with the experimental values.
- The calculated differences in the threshold load for radial cracking upon unloading due to the indenter geometry are less than experimentally observed.
- The agreement between the simulations and the experiments presented here is better than that obtained with the models presented in the literature discussed in section 3.2.5.
- To study cracking effects in indentation with small size indenters, the stress intensity approach is appropriate to approximate cracking threshold loads for cracking.
- The differences in the stress state under the surface (biaxial tension) and at the surface (one tensile component, plane stress state) need to be taken into account in the fracture mechanics approach of indentation cracking.

---

**References for chapter 3**

- Auerbach F., 1891, "Absolute Hartemessung", *Ann. Phys. Chem.*, Vol.43, pp. 61-100.
- Chiang S.S., Marshall D.B. and Evans A.G., 1982, "The Response of Solids to Elastic/Plastic Indentation: I. Stresses and Residual Stresses", *J. Appl. Phys.*, Vol.53, pp. 298-311.
- Chiang S.S., Marshall D.B. and Evans A.G., 1982, "The Response of Solids to Elastic/Plastic Indentation. II. Fracture Initiation.", *J. Appl. Phys.* Vol.53, pp. 312-317.
- Cook R.F. and Pharr G.M., 1990, "Direct Observation and Analysis of Indentation Cracking in Glasses and Ceramics", *J. Am. Cer. Soc.*, Vol. 73, No.4, pp. 787-817.
- Donkelaar E.J. van and Dijk H.J.A. van, 1989, Personal Communication.
- Donkelaar E.J. van and Dijk H.J.A. van, 1990, Personal Communication.
- Griffith A.A., 1920, "The Phenomena of Rupture and Flow in Solids", *Philos. Trans. R. Soc. London, Ser. A*, Vol.221, pp. 163-198.
- Hertz H., 1881, "On the Contact of Elastic Solids", (in German), *Zeitschrift fur die reine und Angewandte Mathematik*, Vol.92, pp. 156-171. English translation by D.E. Jones and G.A. Schott in *Miscellaneous Papers*, pp. 146-162, McMillan, London, 1896.
- Hertz H., "Gesammelte Werke", Vol.1, pp. 155 ev., Leipzig 1895.
- Hill R., 1950, *The Mathematical Theory of Plasticity*, Oxford Un. Press, pp. 103-106.
- Inagaki M., Urishima K., Toyomasu S, Goto Y. and Sakai M., 1985, "Work of Fracture and Crack Healing in Glass", *J. Am. Cer. Soc.*, Vol.68, pp. 704-706.
- Inglis C.E., 1913, "Stresses in a Plate Due to the Presence of Cracks and Sharp Corners", *Trans. Inst. Naval Archit.*, Vol.51, No.1, pp. 219-230.

Johnson K.L., 1985, *Contact Mechanics*, Cambridge Un. Press, pp. 170 ev.

Lawn B.R. and Fuller E.R., 1975, "Microfracture beneath Point Indentations in Brittle Solids", *J. Mat. Sci.*, Vol.10, pp. 113-122.

Lawn B.R. and Wilshaw R., 1975, *J. Mat. Sci.*, "Review Indentation Fracture: Principles and Applications", pp. 1049-1081.

Lawn B.R. and Evans A.G., 1977, "A Model for Crack Initiation in Elastic/Plastic Indentation Fields", *J. Mat. Sci.*, Vol.12, pp. 2195-2199.

MARC, 1990, *Revision K4 Handbook*, MARC Analysis Res. Corp., Palo Alto, CA, USA.

Mindlin R.D., 1936, "Force at a Point in the Interior of a Semi-Infinite Solid", *Physics (NY)*, Vol.7, pp. 195-202.

Orowan E., 1949, "Fracture and Strength of Solids", *Rep. Progr. Physics*, Vol.14, pp. 185-232.

Ostojic P. and McPerson, R., 1987, "A Review of Indentation Fracture Theory: Its Development, Principles and Limitations", *Int. J. Fract.* Vol.33, pp. 297-312.

Paris P.C. and Sih G.C. 1965, "Stress Analysis of Cracks", *ASTM Spec. Publ.* 381, pp. 30-81.

Peter K., 1964, "Sprodruch und Mikroplastizitat von Glass in Eindruckversuchen", *Glastechn. Ber.*, Vol.37, No.7, pp. 333-345.

Roesler F.C., 1956, "Brittle Fractures near Equilibrium", *Proc. Phys. Soc.*, No.10, pp. 981-992.

Rossmann H.P., "Grundlagen der Bruchmechanik", Springer, 1982.

---

Smith S.S., Magnusen P. and Pletka B.J., 1981, "Fracture Toughness of Glass using the Indentation fracture Technique", in *Fracture Mechanics Methods for Ceramics Rocks and Concrete*, ASTM STP 745, Freiman S.W. and Fuller E.R. editors, ASTM, pp. 33-45.

Tangena A.G., Franklin S. and Franse J., 1989, "Scratch Tests on Hard Layers", Proc. 16<sup>th</sup> Leeds-Lyon Symp. on Interface Dynamics.

Tillet J.P.A., 1956, "Fracture of glass by spherical indenters", Proc. Phys. Soc. B. Vol.69, pp. 47-54.

Timoshenko S.P. and Goodier J.N., 1970, *Theory of Elasticity*, McGraw-Hill, NY, pp. 308-402.

### Appendix 3.1 : Discussion of stress intensity factor calculations.

For the case of an axial symmetrically loaded penny shaped crack (Fig. 3.24 a), the stress intensity factor is (Paris 1965)

$$K_I = \frac{2}{\sqrt{\pi c}} \cdot \int_0^c \frac{x \cdot \sigma(x) \cdot dx}{\sqrt{c^2 - x^2}} \quad \{A3.1.1\}$$

For a very thin (hair-like) crack in a plane strain stress state, with a non-uniform stress over its crack faces (Fig. 3.24 b),  $K_{Ir}$  at the right-most crack tip is calculated to be:

$$K_{Ir} = \frac{1}{\sqrt{\pi c}} \cdot \int_{-c}^c \sigma(x) \cdot \sqrt{\frac{c+x}{c-x}} \cdot dx$$

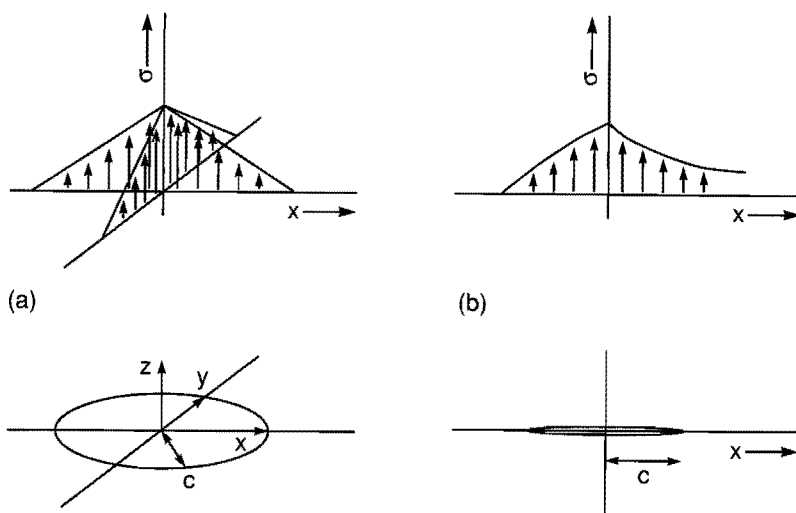


**Fig. 3.24**

*An axial symmetrically loaded penny shaped crack (a) and a hair-like crack (b), in a non-uniform stress field.*

The  $K_I$  factor at the left-most crack tip  $K_{II}$  for the same case is:

$$K_{II} = \frac{1}{\sqrt{\pi c}} \cdot \int_{-c}^c \sigma(x) \cdot \sqrt{\left(\frac{c-x}{c+x}\right)} \cdot dx \quad \{A3.1.3\}$$

Since the  $K_I$  factor calculation involves taking an integral over the product of the stress and the distance along the preexisting flaw, it is also a measure of the elastically stored energy in the vicinity of the flaw.

If a flaw is subjected to more loads simultaneously, in the same fracture mode, the  $K_I$  factors due to the individual loads may be added to obtain the total  $K_I$  value. (For instance the  $K_I$  factors due to a distributed load and that due to a point load, acting in the same direction on a crack can be added)

If a crack is loaded in more than one mode (direction), the energy release rates are summed to see if the combination of modes will lead to cracking. The total stress intensity factor  $K_{tot}$  in that case follows from an expression of the basic form

$$K_{tot} = \sqrt{K_I^2 + K_{II}^2 + K_{III}^2} \quad \{A3.1.4\}$$

(The exact form involves the modulus of elasticity and Poisson's ratio to account for differences between the tensile and shear moduli).

This rule is used in the present study to take into account the effect of two principal tensile stresses acting on one flaw.

Obviously, the type and the dimension of the assumed flaw (axial-symmetric stress over penny like crack versus hair-like crack in non-uniform stress field) can be expected to influence the calculated value of  $K_I$ . In addition, the location of the assumed flaw with respect to the maximum in the stress profile will also influence the calculated value of  $K_I$ . From a physics point of view, it seems reasonable to assume that the flaw (caused by the deformation during indentation) originates from within the plastic region. It not unlikely that it partially extends into the elastic region. The most likely size of the flaws can be estimated from the following reasoning. The flaws are loaded in tension, so they would be opened due to the load. However, in practice, they are not resolved by an optical microscope, so they cannot be much larger than one micrometer. In addition, the tensile stress region extends only over a few micrometers, so it makes little sense to assume a much larger flaw size. The minimum dimension of the flaw can also be estimated. For a hair-like crack (length  $2 \cdot c$ ) loaded by a uniform tensile stress  $\sigma$  the  $K_I$  factor is

$$K_I = \sigma \cdot \sqrt{\pi \cdot c} \quad \{A3.1.5\}$$

$K_c \approx 0.8 \text{ MPa}\sqrt{\text{m}}$  for most glasses and the plasticity limits the maximum value of  $\sigma$  to about one third of the flow stress ( $\sigma_f \approx 1800 \text{ MPa}$ ) The minimum flaw size that could become critical can be calculated by rearranging eq. {A3.1.5}.

$$c_{\min} = \frac{1}{\pi} \cdot \left( \frac{3 \cdot K_c}{\sigma_f} \right)^2 = 5 \cdot 10^{-7} \text{ m} = 0.5 \text{ }\mu\text{m} \quad \{A3.1.6\}$$

In view of the foregoing, the size of the flaw ( $2 \cdot c$ ) has to be about 1 micrometer. Any choice however between 0.5 and 2  $\mu\text{m}$  is arbitrary. A larger value for  $c$  leads to systematically higher calculated  $K_I$  values. Since the stress profiles decay away from the maximum, the sensitivity of  $K_I$  with respect to the assumed flaw size is limited, especially if the flaw is located symmetrically with respect to the maximum in the stress profile. In calculations of  $K_I$  factors using the same stress profile assuming values for  $c$  of 0.25, 0.5 and 0.75  $\mu\text{m}$ , variations of about 20% were typically found. All the  $K_I$  factors reported here were obtained assuming  $c=1 \text{ }\mu\text{m}$ , unless explicitly stated otherwise.

The next topic to be addressed is the assumed geometry of the flaw. The flaws from which cracks pop-in are intersecting shear faults in the plastic region in which the indenter is encased. There are some arguments to support that the hair-like flaw geometry is somewhat more realistic than the axial symmetrical loaded penny shaped crack. In the literature, the most commonly assumed flaw is the penny shaped flaw in a axial symmetrical stress state. This is probably due to the fact that eq. {A3.1.1} can be integrated relatively easy. The stress state over such an assumed penny shaped flaw located somewhere along the axis of symmetry under the indenter is definitely not axially symmetric. The difference in the  $K_I$  value calculated for both flaw geometries was investigated in the following way.

Looking at eq. {A3.1.1}, {A3.1.2} and {A3.1.3}, it is seen that the integrand for the stress intensity factor calculation in all cases is the product of a geometrical factor and the stress over the crack.

In Fig. 3.25, the value of these geometrical factors along the crack face can be seen for the two crack geometries. In addition, a characteristic normalized stress profile is shown. It is characteristic in the sense that in the actual stress profiles



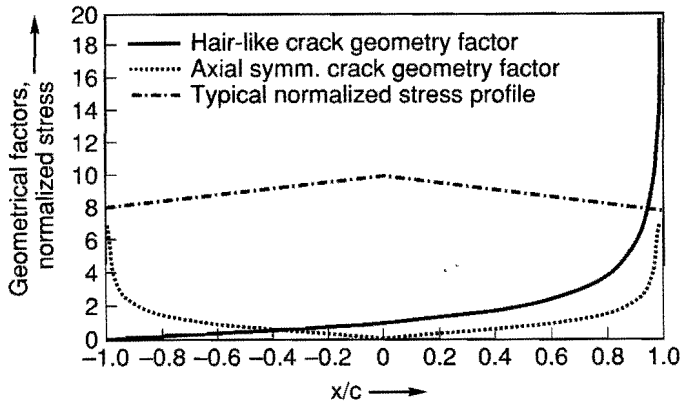


**Fig. 3.25** *The geometrical factors and a typical stress profile used to investigate the influence of the flaw geometry on the calculated  $K$  value.*

analyzed, the decay rate is usually such that the stress value at the flaw tip position is typically 20% less than the maximum stress value. Using equations {A3.1.1}, {A3.1.2} and {A3.1.3}, "K factors" were now calculated for the hair-like and the axial symmetrical crack geometries. By themselves, these numbers are quite meaningless, but their ratio is the same as would be obtained comparing two actual  $K_I$  factors calculated using the two crack geometries and the same stress profile. It was found that the  $K_I$  value calculated assuming a hair-like crack is typically 30 to 40 percent higher than for a penny shaped crack.

In view of the arguments presented (visibility, minimum crack size that could lead to cracking in view of maximum stress value and limited extend of tensile stress region), it was decided to assume a hair-like flaw geometry for the  $K_I$  calculations.

The last point that needs clarification is the influence of the assumed location of the flaw with respect to the position of the extreme value in the stress profile.

In Fig. 3.26, three situations that were compared are illustrated. The first two are the  $K_I$  factors at the right ( $K_{I_r}$ ) and left ( $K_{I_l}$ ) crack tips for a hair-like crack lying completely in the elastic region. The third case was that of a crack located with its

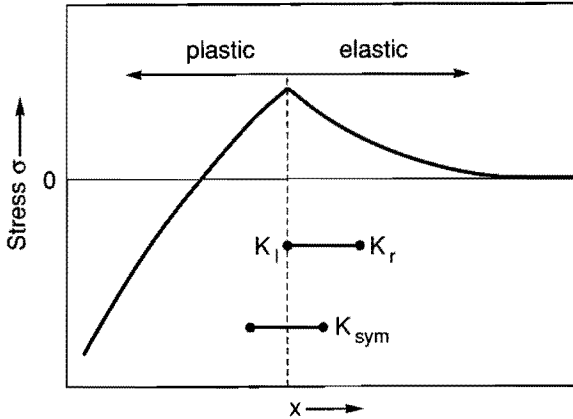


**Fig. 3.26** *The value of the  $K$  factor calculated depends on the location of the flaw with respect to the maximum in the stress profile.*

center at the position of the maximum in the stress profile. In the latter case, the stress profile over the crack was assumed to be symmetrical over the crack ( $K_{I_{sym}}$ ) (the stress in the elastic region was taken). It was found that the values of  $K_{I_l}$  and  $K_{I_{sym}}$  calculated were virtually the same, and the values for  $K_{I_r}$  were typically 30% lower for values of  $K_{I_{sym}}$  up to 0.3 MPa $\sqrt{m}$ , while for higher values the difference decreased to about 10%. The observations of crack initiation during the indentation experiments suggest that the cracks, directly after initiation at the boundary of the plastic zone, run both toward the indenter and away from it (virtually simultaneous extension of both crack tips). Therefore, it was decided to use the  $K_{I_{sym}}$  method to calculate  $K_I$  factors, and all values presented have been calculated this way.



## 4. Form accuracy in precision contour grinding.

### 4.1. Problem description, method of investigation.

As discussed in section 1.5.1, the form accuracy of optics is essential for their optical performance (geometrical aberrations). The achievable form accuracy depends on the combination of machine tool and process conditions used (section 1.4).

Form errors generally arise due to slow varying effects. The time scale of fluctuations causing form errors is similar (or longer) than the duration of a single cut over the surface (also called pass). For a more thorough discussion of error categorization and reduction techniques the reader is referred to the literature (Blaedel 1980).

The situation during contour grinding and the meaning of various terms frequently used throughout this chapter can be seen in Fig. 4.1.

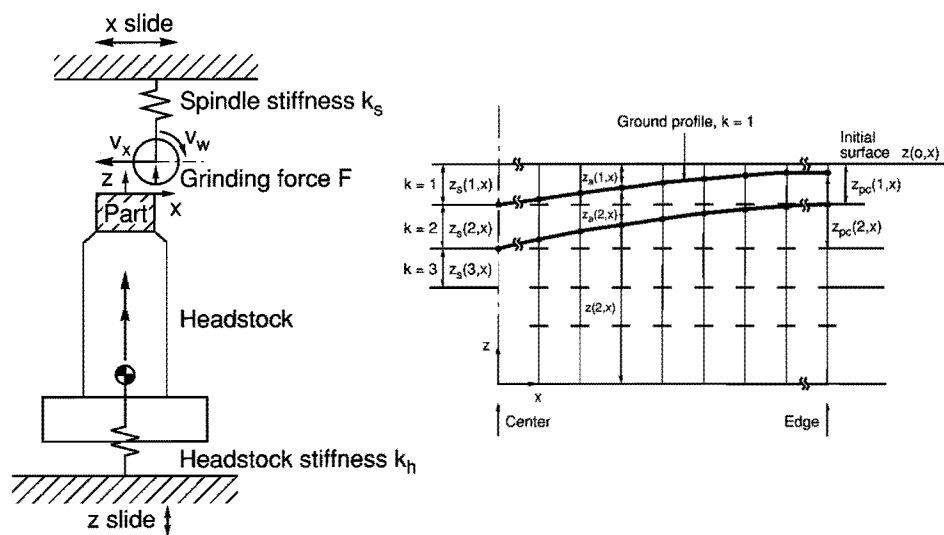


Fig. 4.1 Contour grinding situation, meaning of infeed per pass  $z_s(k,x)$ , cumulative depth of cut  $z_{pc}(k,x)$  experienced by the material and actual cutting depth  $z_o(k,x)$ .

During a cut, the grinding wheel moves in x-direction from the edge of the part toward the center, at a speed  $v_x$ . In later sections, discrete x-positions ( $x_i$ ), spaced a distance  $f$  apart are considered. This feed rate  $f$  is given by

$$f = \frac{60 \cdot v_x}{N_p} \quad \{4.1\}$$

with  $N_p$  the part speed in rpm and  $v_x$  in mm/s. In contour grinding, during an arbitrary cut (index  $k$ ) the grinding wheel is given an infeed denoted by  $z_s(k,x)$  by moving the z-slide. During cut number  $k$ , at position  $x$ , the cumulative infeed is given by  $z_{sc}(k,x)$ :

$$z_{sc}(k,x) = \sum_{n=1}^k z_s(n,x) \quad \{4.2\}$$

The actual depth of cut in pass  $k$ , position  $x$ , is  $z_a(k,x)$  and the total depth of cut at position  $x$  after pass  $k$  is

$$z_{ac}(k,x) = \sum_{n=1}^k z_a(n,x) \quad \{4.3\}$$

The grinding force in z-direction (cut number  $k$ , position  $x$ ) is  $F(k,x)$ .

A distinction is made between the infeed (machine slide displacement) and the cumulative depth of cut as experienced by the part material. The cumulative depth of cut  $z_{pc}(k,x)$  experienced by the part material is the difference between the cumulative infeed  $z_{sc}(k,x)$  and the total depth of preceding cuts  $z_{ac}(k-1,x)$ .

$$z_{pc}(k,x) = z_{sc}(k,x) - z_{ac}(k-1,x) \quad \{4.4\}$$

The indices  $k$  and  $x$  are omitted when considering  $x$  as a continuous variable and when discussing a variable in a general context, without referring to a specific cut.

The problems addressed in this study will be illustrated by discussing experimental results of a grinding operation (Fig. 4.2). Before each cut, the machine z-slide is moved  $z_s(k,x)=1 \mu\text{m}$  in the z-direction. In all experiments reported in this thesis, such uniform infeed profiles were used, instead of the non-uniform infeed profiles used when grinding a complex contour. The grinding wheel comes in contact near the edge of the initially flat part and is moved toward the centerline of the part. At the edge of the cylindrical part, a reference step has been ground

before the test. After  $k$  cuts, the total infeed  $z_{sc}(k,x)$  is  $k \mu\text{m}$  (Part speed  $N_p=100$  rpm, wheel speed  $N_w=40.000$  rpm).

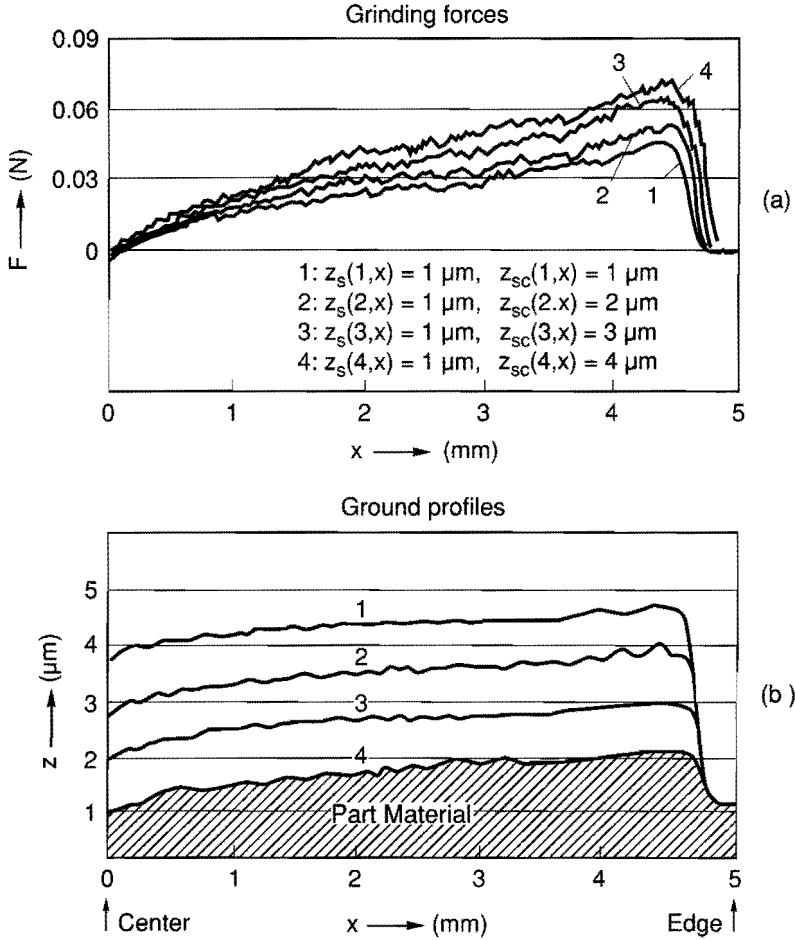


Fig. 4.2 Grinding force  $F$  (a) and surface profiles (b) ground in glass (type BK7) with infeeds of  $1 \mu\text{m}$  each cut. Resin bond wheel (K+888), feed rate  $v_x=2 \text{ mm/min}$ .

Fig. 4.2 (a) shows the grinding force ( $F$ ), measured in the  $z$ -direction, and ground surface profiles (Fig. 4.2 (b), height  $z$  as a function of the radial coordinate  $x$ ) after subsequent cuts. At the edge of the part, the grinding force is largest, it decreases as the grinding wheel moves toward the center. The maximum value of the force during a cut ( $F_{\max}$ ) becomes higher in consecutive cuts.

Looking at the ground profiles in Fig. 4.2, it is noted that after the first cut, the profile  $z(x)$  is non-linear in  $x$ , so the actual depth of cut has not been uniform as intended. In the second and third cuts, the shape of the ground profiles changes slightly. The difference in the shape of the ground profiles becomes less in following cuts. There is an evident similarity between the form of the ground profiles and the corresponding force curves.

In precision contour grinding, thermal and other environmental effects, deflections due to the compliance of the machine tool and the grinding wheel, and grinding wheel wear are sources of form errors. At the outset of this investigation, the relations between the machine characteristics and the process variables on one side and the form of the ground profile on the other were not understood.

The experimental results discussed above indicate that the process has a "memory effect" in the sense that the profile (error) generated in a particular pass to some extent depends on the cutting sequence executed before.

The purpose of the investigation reported here was:

- To study the effects of the grinding process variables upon form errors experimentally.
- To model the process and quantify the effects of machine, process parameters and the memory effect on form accuracy.
- To improve the reproducibility and the achievable form accuracy of the precision contour grinding process.

The approach in this chapter is as follows:

- First an inventory of the random error sources and a brief description of appropriate counter-measures is made.
- Next the machine properties and process variables which are likely to affect contour accuracy in a repeatable manner are listed.
- The results of grinding experiments carried out to investigate these effects are presented.

- A model to quantify the effects of the dominant parameters and to simulate the process is presented.
- The results of simulations are compared with those obtained from grinding experiments.
- Based on experiments and simulations, a quite general theory is developed to predict the profile accuracy that can be reached with an arbitrary combination of machine tool, grinding wheel, process variables and grinding procedure.
- It is shown that the achievable profile accuracy can be improved by a feed forward compensation for the profile errors resulting from former passes.

## 4.2. Random form errors in contour grinding.

The term random is used here for errors resulting from disturbances whose occurrence is unpredictable, and whose effects are not (yet) corrected by the measurement and control system.

### 4.2.1. Environmental effects.

Form errors due to *thermal effects* in the machine environment are usually random in nature (McClure 1969). In earlier tests on the so-called Kolatje facility (Fig 1.6), this type of errors seriously affected the reproducibility of grinding experiments.

Although the sensitivity of a machine tool to thermal disturbances can be limited by good design (symmetry rules, choice of materials, metrology loop lay-out), suppression of these effects at the source is often the best way to reduce the influence of random temperature fluctuations to an acceptable level.

A thermally stable experimental facility (the ESDO, Fig.1.8) was built, to be able to do grinding tests in a thermally well-conditioned environment. The oil supplied to the machine slides is conditioned to within a bandwidth of  $0.01^\circ$  around  $20^\circ\text{C}$  nominal. The machine is operated in a relatively small down-flow laminar flow enclosure with air temperature control to within  $0.04^\circ\text{C}$  (Peak to Valley variation around  $20^\circ\text{C}$ ). Even with these provisions, it proved to be necessary to follow strict procedures for the grinding and form measurement cycles during experiments. Such procedures are useful to allow the system to reach a stationary situation after



thermal disturbances such as turning on the coolant, or starting the headstock spindle.

With the measures described above, tests on the ESDO reproduced much better indeed, compared to earlier tests on the Kolatje facility (section 1.6). Test-to-test variance in grinding experiments carried out on the ESDO is more often than not due to process related effects which will be discussed in more detail in section 4.2.2.

The brief description given here of counter-measures against thermal effects does not mean that they are relatively unimportant compared to the effects described further on.

The study of thermal effects in a machine tool (environment) and coordinate measurement machines (Teeuwesen 1989) is a field in itself within precision engineering (Franse 1990<sup>1</sup>). To achieve the temperature control for the ESDO mentioned was a considerable endeavor. However, the techniques used are state-of-the-art in the field of thermal measurement and control for precision machine tools. Since the emphasis here is on the precision grinding process, we will not go into details of the machine construction or the environmental control system.

With machine tools whose linear motions are controlled using laser interferometry in air, changes in the index of refraction in the measurement path due to changes in the composition of the machine environment and barometric pressure variations cause random error motions (Schellekens 1986). For the ESDO, these errors are in the order of 0.1-0.2  $\mu\text{m}$  typically over an 8 hour period ( $\approx 0.1 \mu\text{m}/\text{mbar}$  drift) in the x-direction, less in the z-direction due to the shorter measurement path of the laser interferometer. This means that over the duration of a grinding test ( $\approx 1$  hour), these errors are relatively small. Several measures can be taken to get rid of these errors and enhance the reproducibility of the grinding operation, for instance:

- Place the interferometer in vacuum.
- Compensate in-process for the change in refractive index (wavelength compensator).
- Replace the interferometer with another length measuring system, such as a glass ruler.

---

<sup>1</sup> Section 3.7 of this overview article and references listed there.

---

#### 4.2.2. Surface of the grinding wheel after conditioning.

Another error source is the *condition of the grinding wheel surface* after dressing and trueing. It is uncertain whether after multiple dressing/trueing operations the grinding wheel has similar topographic and mechanical characteristics.

In section 4.5 where the grinding experiments are reported, this is discussed in more detail.

This effect was found to be the major source of variance in our grinding results.

#### 4.3. Reproducible form error contributions.

Some reproducible errors are solely due to characteristics of the machine tool. *Geometrical error motions* of the slide and headstock spindle and the form error of the *reference mirror* used in the laser interferometric measurement system fall in this category.

The form error budget of the ESDO (Table 1.1) shows that these contributions are in the nm range for small diameter parts.

Another category of repeatable form errors are the *deflections* of machine tool components and the grinding wheel due to cutting forces. These deflections depend on the stiffness of the grinding wheel and the machine tool structure, in combination with the process variables chosen. The process variables and the grinding wheel surface condition determine the intensity of the tool-part interaction, and consequently, the grinding force. The magnitude of the deflections (form error) in turn depends on the force and the combination of all the compliances in the structural loop. However, if the process variables are well controlled (reproducibility of all relevant quantities), the force and thus the form errors due to these compliance effects will be repeatable.

To some extent, a similar reasoning is valid for the form errors due to *grinding wheel wear*. If the wear follows a simple law, such as "the grinding wheel radius ( $R_w$ ) decreases at a constant rate, and so the radius of the grinding wheel decreases linear with the total path traversed over the part", the resulting error will be predictable/repeatable (Giridharan 1986).

In practice, a typical resin bond grinding wheel shows a high wear rate directly after reconditioning.

During further use, for quite a number of passes, the wear rate is low and can be neglected (when grinding small enough parts), until the wheel becomes so dull that reconditioning becomes necessary.

From preliminary experiments, it became apparent that deflections in the structural loop, in other words the machine tool and grinding wheel stiffness in combination with the process variables, are the most dominant sources of profile errors. It was therefore decided to model these effects and to investigate them experimentally.

#### **4.4. Qualitative discussion of influences, nominal parameter values in contour grinding.**

A schematic view of the contact situation during grinding can be seen in Fig. 4.3. Quantities which can be expected to have an influence upon the grinding forces and therefore on the deflections and form errors are:

- The hardness and elasticity of the material to be ground. Tests were mainly done on the optical glass BK7, with a hardness  $H_v$  of about 5500 MPa and modulus of elasticity ( $E$ ) of 81 GPa. For comparison, tests were also done on a ferritic 17% Chromium steel,  $E=210$  GPa, hardness 50 Rockwell C, which corresponds to  $H_v \approx 3500$  MPa.
- The stiffness of the headstock and grinding spindles (rotating at working speed, but for low frequency excitation). The headstock spindle stiffness in axial direction ( $k_b$ ) was (experimentally determined)  $60 \text{ N}/\mu\text{m}$ , the grinding spindle stiffness ( $k_s$ ) measured in z-direction at the position of the cutting edge was  $0.7 \text{ N}/\mu\text{m}$ .
- The modulus of elasticity of the grinding wheel ( $E_w$ ). Time dependent effects in resin binders are not considered. A grinding wheel is a composite of a resin or metal binder material, metal or polymer filler material, and diamond. The modulus of elasticity of a typical resin bond grinding wheel (Winter K+888, D7, c100, a resin bond wheel containing 0.88 gram,  $7 \mu\text{m}$  average diameter diamond/cm<sup>3</sup>, approximately 25 vol. % diamond) was derived from indentation tests. A value of  $E_w=8$  GPa was found. Typical values for the modulus of elasticity for the resins and polymers used as binders in grinding wheel are between 1 and 5 GPa.

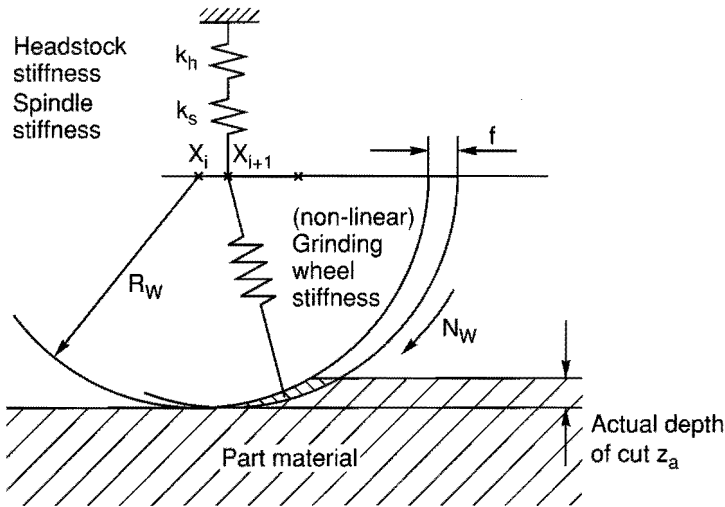


Fig. 4.3 The contact situation during contour grinding.

It can be concluded that the filler materials and the relatively high diamond concentration in the wheel does indeed increase the matrix stiffness. Tests were done using this type of wheel as reference. More resilient and more rigid wheels (polymer and metal bonds) were also tested.

- The radius of the grinding wheel ( $R_w$ ) was nominally 4.0 mm. This parameter affects the local area of contact in grinding, so it can be expected to have an influence.
- The width of the contact area in the  $y$  direction. In case a line contact is assumed this will be the width ( $W$ ) of the grinding wheel. In principle, the form of the grinding wheel can be expected to give rise to an approximately elliptical contact area. In that case the radius of the grinding wheel  $R_y$  in the  $y$ - $z$  plane (Fig. 4.13) is of importance. Both the line and the elliptical contact situation will be analyzed theoretically. The experimental approach was to use cylindrical grinding wheels to approximate a line contact situation. The contact width  $W$  was estimated at 1 mm.
- The feed rate  $v_x$  influences the geometry of the contact area and therefore probably the grinding force. Typical values are about 1 mm/min.

- The angular velocity of the headstock spindle influences the amount of material removed per unit time and can therefore be expected to have an effect on the grinding forces. Typical values are about 100 rpm.
- The influence of the angular velocity of the grinding spindle can be expected to be small, presuming it remains above a certain value, so that adequate space for the removal of debris from the contact area is ensured. The grinding spindle speed in the experiments was 40.000 to 50.000 rpm.
- The actual depth of cut  $z_a$  (Fig. 4.3). This affects the contact area, so it will influence the grinding forces (section 4.6.1).
- The viscosity of the coolant entering the space between the part and the grinding wheel has been suggested to lead to a wedge action. This effect was investigated using formulas presented by Gross (1980). Calculations were done for typical grinding conditions, where water is used as coolant, assuming a linear decreasing gap height in the contact zone, ranging from 200 to 0.5  $\mu\text{m}$ . The results suggest only a small force due to this wedge action ( $\approx 0.01 \text{ N}$ ). This force is mainly determined by the angular velocity of the spindle (40.000 rpm) and is therefore virtually constant, independent of the grinding wheel position with respect to the part center.

After this qualitative introduction of the most important parameters in profile grinding, their influence will be discussed more quantitative in section 4.6.1. Grinding experiments were also carried out to investigate the effects of these parameters on the form accuracy in contour grinding.

## 4.5. Grinding experiments.

### 4.5.1. Description of grinding experiments.

From the inventory in the former section, 16 parameters appear to be important for the profile errors in contour grinding:  $v_x$ ,  $N_p$ ,  $N_w$ ,  $k_h$ ,  $k_s$ ,  $R_w$ ,  $R_p$ ,  $z_s$ ,  $E_w$ , number of cuts  $k$ , number of spark-out cuts (additional passes without machine infeed), modulus of elasticity, hardness of the part, the shape (line or elliptical) and width of the contact area and the wheel surface condition after dressing/truing.

If the aim of this investigation would have been process control for mass production, a two-level factorial experiment design would be appropriate to obtain the maximum amount of information from only a limited number of experiments (Gibbins 1986, Wadsworth 1990).

This type of experiments involves changing more than one condition at a time. The results obtained are the main effects of particular variables on average (averaged over the high and low levels of the other variables), and (depending on the experiment lay-out) an understanding of some of the interactions between the variables.

However, to improve the reproducibility and accuracy of the contour grinding operation, it is necessary to develop a thorough understanding of the mechanisms underlying the effects of the dominant variables, including non-linear effects and interactions between dominant variables, and to identify sources of variance.

Therefore, the number of variables investigated was first limited using a few pragmatic rules. Next, a one-at-a-time approach was taken and the effect of each variable was determined in turn while the others were held at their nominal values in the mid-range of the span over which these parameters are varied in grinding practice.

The stiffness of the headstock and grinding spindle were considered as fixed values,  $R_w$  and  $R_p$  were kept constant (4 mm), and  $N_w$  was kept at 40.000 rpm, since in practice, the spindle speed is determined by dynamic considerations. Cylindrical grinding pallets were used, to approach a line contact situation with  $W=1$  mm.

In some experiments, more than one variable is inevitably changed at the same time ( $E$  and  $H$  when going from glass to steel parts for instance, or because the wheel has to be reconditioned during a series of experiments) and in a multi-cut procedure  $k$  is varied automatically. This limits the number of experiments to a reasonable number.

The reconditioning operation is treated as a source of variance, not as a variable, since it is meant to bring the wheel surface in the same condition every time.

The number of effects to be discussed in this section is therefore limited to 8; influence of  $k$ , effect of reconditioning,  $N_p$ ,  $v_x$ ,  $E_w$ , spark-out passes, part material and finally the effect of the machine infeed  $z_s$ .

After a brief description of the experimental procedures in the remainder of this section, the experimentally observed effects of these variables will be presented in the next section.

Most experiments were carried out on optical glass (BK7, hardness  $H_v=5500$  MPa,  $E=81$  GPa,  $\nu=0.25$ ), some were done on a 17% Chromium, ferritic stainless steel ( $E=210$  GPa,  $\nu=0.3$ ,  $H_v=3500$  MPa). Cuts were made on an end face of cylindrical pieces with a radius of 5 mm.

A typical cutting sequence was to start with a flat surface and to make a number of cuts, each with a nominally uniform infeed in z-direction of  $z_s(k,x)=1 \mu\text{m}$ . The (by far the largest) component  $F$  of the grinding force perpendicular to the part was measured during each cut, the form of the part was measured on-line after each cut.

Description BK7 tests	Parameter value	K+888 phenol resin	SP2042 poly- amide resin	BZ387 bronze bond	K730E phenol resin
5 cuts, $v_x$ constant.	5 times $z_s=1 \mu\text{m}$	*	*	*	*
5 cuts, $N_p$ increasing	5 times $z_s=1 \mu\text{m}$ , $50 < N_p < 600$	*	*	*	*
2 cuts + spark-out	2 times $z_s=1 \mu\text{m}$ , 20 times $z_s=0 \mu\text{m}$	*	*	*	*
Part speed $N_p$ varied	$N_p=50$ rpm $N_p=100$ rpm $N_p=300$ rpm				*
feed rate $v_x$ varied	$v_x=0.25$ mm/min $v_x=0.5$ mm/min $v_x=1.0$ mm/min $v_x=1.5$ mm/min $v_x=2.0$ mm/min $v_x=2.5$ mm/min	*	*	*	*
infeed $z_s$ , 5 cuts each test.	$z_s=5$ times $0.25 \mu\text{m}$ , $z_s$ was raised in $0.25 \mu\text{m}$ steps to $z_s=5$ times $2.0 \mu\text{m}$	*			*

**Table 4.1** Summary of test conditions in experiments on BK7 glass with four different grinding wheels.

Steel	Parameter value	K730E
5 times $z_s = 1 \mu\text{m}$	feed rate $v_x = 1.0, 2.5 \text{ mm/min}$	*
3 times $z_s = 1 \mu\text{m}$ , + 10 x spark-out	feed rate $v_x = 0.25, 0.5 \text{ mm/min}$	*
3 times $z_s = 1 \mu\text{m}$ , + 10 x spark-out	$N_p$ increasing from 50 to 600 rpm	*

**Table 4.2** Test conditions during grinding tests on stainless steel.

In some tests, after a part had been cut this way, spark-out passes were made.

A spark-out pass is an additional pass over the surface, without further infeed of the machine ( $z_s(k,x) = 0 \mu\text{m}$ ).

These procedures were carried out using four different grinding wheels, ranging from resilient resin bond wheels (Winter SP2042, K+888, and K730E) to an extremely hard bronze bond wheel (Winter BZ 387 (Holz and Sauren, 1986)).

With all four grinding wheels, a test was also done in which the part speed  $N_p$  was increased while the wheel moved from the edge to the centerline of the part, to keep the volume of material per unit time more constant than if constant part speed and feed rate are maintained during the pass.

Tests were also done with resin bond wheels (Winter type K730E), in which only the feed rate  $v_x$  was varied. Another series of tests was carried out in which the part speed  $N_p$  was varied while all other parameters were kept constant. A number of tests were done two or three times, in some cases with intermediate reconditioning of the wheel, to study the effect of dressing and trueing on the reproducibility of the tests.

A summary of the tests performed on glass is given in Table 4.1. A similar overview for the test conditions during the experiments on steel parts can be found in Table 4.2.



#### 4.5.2. Results of grinding experiments.

As explained in the former section, the influence of 8 variables and one source of variance will be discussed in this section: the influence of the number of cuts  $k$ , the effect of reconditioning the wheel (variance source), varying  $N_p$ ,  $v_x$ ,  $E_w$ , spark-out passes, the part material and finally the effect of the infeed per cut  $z_s$ .

Those parameters that are not explicitly mentioned were held at their nominal values during tests. ( $N_p=100$  rpm,  $v_x=2.5$  mm/min,  $N_w=40.000$  rpm, glass part).

##### *Nominal conditions, effect of the number of cuts $k$ .*

In Fig. 4.4 and Fig. 4.5, the grinding forces and ground profiles are shown for a test consisting of 5 uniform cuts (5 times  $z_s=1$   $\mu\text{m}$ ) with the relatively resilient resin bond K+888 wheel. The part speed  $N_p$  was 100 rpm, the feed rate  $v_x$  was 2.5 mm/min, a glass part was ground.

It is apparent that the actual depth of cut  $z_s$  has not been uniform as intended. In the part center, grinding forces become virtually zero each cut, and all material that was meant to be removed is indeed cut away. The (maximum value of the) grinding force increases each pass.

The non-linear course of the grinding force as a function of the  $x$  position of the wheel is reflected in a non-linearity of the ground profile, especially close to the center of the part.

The "step" at the edge of the part (Fig. 4.5) is a reference plane that was ground before a particular test to establish a reference plane. The "hobble" left in the part center (Fig. 4.5) is due to an irregularity in the grinding wheel surface. In these experiments no special care was taken to avoid this effect which is often observed. It can be avoided by rigorous redressing of the grinding wheel, or by changing the orientation of the grinding spindle with respect to the part surface.

In general, the distance between profiles ground in successive passes, measured at the part center, is a good indication of the actual relative displacement between the cutting edge and the part between cuts, so it can be used to discover possible machine infeed errors.

##### *Reconditioning of the wheel.*

The experimental procedure included (re)conditioning the grinding wheel before each test. However, this was found to give rise to significant variance in the results.

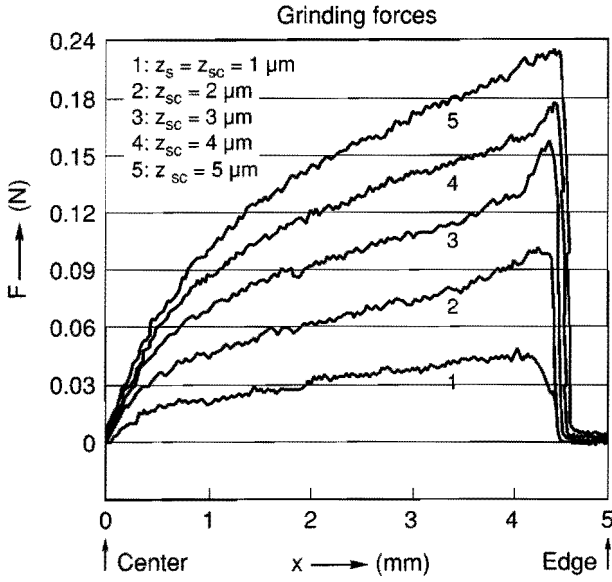


**Fig. 4.4** Grinding force  $F$  during test on glass, consisting of 5 times  $z_s = 1 \mu\text{m}$ , grinding wheel K+888, nominal conditions.

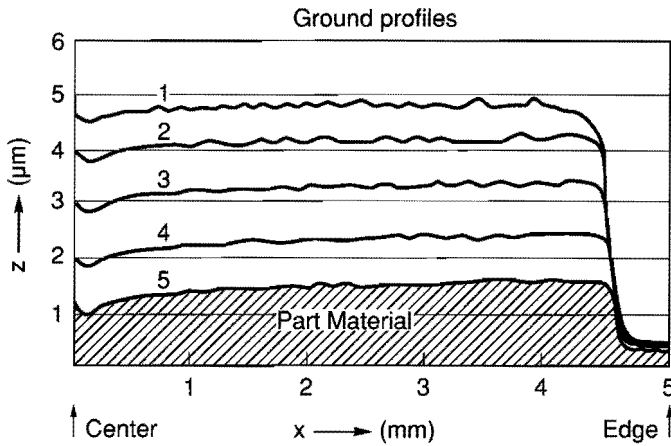


**Fig. 4.5** Profiles ground with wheel K+888, 5 cuts, each nominally  $1 \mu\text{m}$  infeed, nominal conditions.

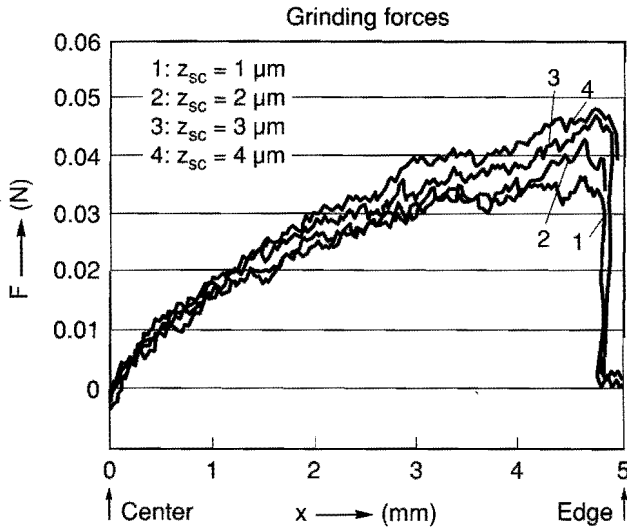


Fig. 4.6 Grinding force in test with 4 times  $z_s=1 \mu\text{m}$ , K+888 wheel, nominal conditions.

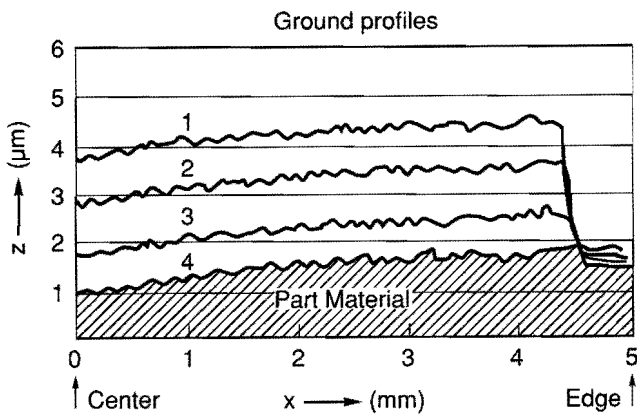


Fig. 4.7 Profiles ground with 4 times  $z_s=1 \mu\text{m}$ , K+888 wheel, nominal conditions.

As an example, Fig. 4.6 and Fig. 4.7 show forces and profiles obtained in a test (4 infeeds of 1  $\mu\text{m}$ ) which otherwise is a replication of the one reported above (nominal values for the controlled parameters  $N_p$  and  $v_x$ ).

The difference in the maximum value of the grinding forces (compare Fig. 4.4 to Fig. 4.6) is caused by the different wheel condition in these two tests. The grinding wheel condition was apparently not optimal (did not run true) during the second test, which results in significant vibrations. The part profiles reflect this by irregularities (compare Fig. 4.7 to Fig. 4.5). The force levels in the second experiment are significantly lower than during the first experiment (compare Fig. 4.6 to Fig. 4.4), which indicates that the material removal is by fracture mode grinding in the second experiment.

*Effect of the part speed  $N_p$*

Fig. 4.8 shows the maximum value of the grinding force ( $F_{\text{max}}$ ) during the last of a sequence of 5 cuts, each with 1  $\mu\text{m}$  infeed, at different part speeds during grinding tests on glass. Looking at the data obtained in consecutive experiments, a trend is suggested where  $F_{\text{max}}$  diminishes with increasing  $N_p$ . If these data are compared with those obtained from replicated tests, with the same wheel at a later time, when it has been reconditioned a number of times, the variance is larger than the trend in the first set of data.

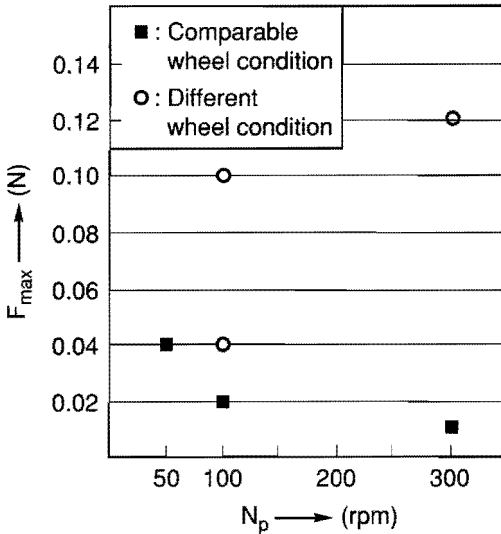


Fig. 4.8 The maximum value of  $F$  in tests were the part speed  $N_p$  was varied. (Wheel K730E,  $v_x=2.5 \text{ mm/min}$ ).

Experiments were also carried out in which the part speed was varied continuously, so as to keep the material removal rate more constant.

The forces and the ground profiles were indeed more linear in nature, except close to the part center. This indicates that grinding under constant removal rate conditions can be beneficial, especially when grinding with resilient resin bond wheels.

#### *Effect of the feed rate $v_x$ .*

Fig. 4.9 shows the maximum force  $F_{\max}$  in the fifth of a series of 5 cuts, each with a uniform infeed  $z_s = 1 \mu\text{m}$  again, for different feed rates  $v_x$ . From the experiments with the K730 wheel, the conclusion is that there is no apparent trend, looking at the K+888 experiments done consecutively, a trend is suggested. Comparing the data with those obtained at other points in time, the variance caused by the wheel reconditioning operation is larger than the trend observed during a series of consecutive experiments.

#### *Interim conclusion regarding wheel reconditioning (dressing).*

The test-to-test variance caused by the surface condition is such that no definitive conclusions can be drawn concerning the effects of varying the feed rate  $v_x$  and the part speed  $N_p$  from the experimental data obtained.

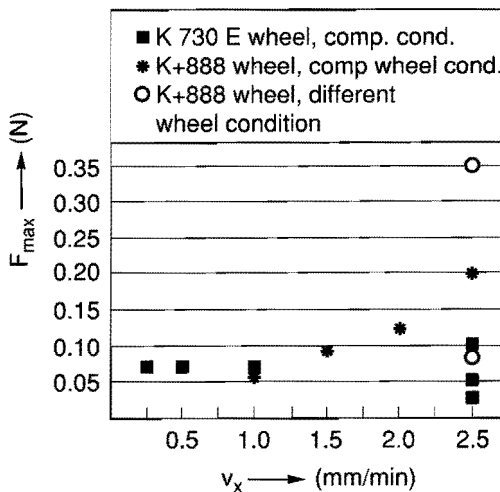


**Fig. 4.9** Maximum value of  $F$  during tests in which the feed rate  $v_x$  was varied (otherwise nominal conditions).

Once the reconditioning operation had been identified as the main source of variance, it was decided to monitor the force on the grinding wheel during the dressing procedure in further experiments. This force signal was found to provide a reasonable indication of the condition of the wheel surface, so the variance could be reduced somewhat.

*Effects of grinding wheel resilience and spark-out passes.*

The differences in the resilience of the grinding wheels tested was very apparent from the experiments. This is illustrated in Fig. 4.10 and Fig. 4.11.

The results seen in Fig. 4.10 and Fig. 4.11 were obtained in the following way. With each grinding wheel in turn, a glass part was ground, 2 cuts  $z_s=1 \mu\text{m}$  infeed each time, followed by 20 spark-out cuts (no additional infeed, so 20 times  $z_s=0 \mu\text{m}$ ).

The forces seen in Fig. 4.10 are those during the second cuts with the different grinding wheels. The SP2042 and K+888 wheels are more resilient than the K730E and the BZ387 wheels. The larger force on the more compliant wheels is accompanied by larger deflections and profile errors.

With the more rigid wheels (K730 and BZ 387), the force curves and the ground profiles after a series of cuts with equal infeed are much straighter than with the more compliant wheels. After 20 spark-out cuts, with resilient wheels, the grinding force still had a maximum value around 0.03 N. With more rigid wheels, the grinding force is virtually zero by that time. The ground profiles after 20 spark-out passes can also be seen in Fig. 4.11.

With the stiff bronze bond wheel (BZ 387), spark-out passes effectively reduce the profile error, using compliant resin bond wheels, the profile error is still considerable even after 20 spark-out passes.

Care has to be taken in interpreting some of these experimental findings, since the effect of some of the variables are confounded with the influences of others.

For instance, the bronze bond wheel is stiffer than the resin bond wheels. The ranking of the resin bond wheels however, can change if wheels of slightly different shape are considered, or if wheels with different surface conditions are compared and the contact stiffness is altered (section 4.6.1).

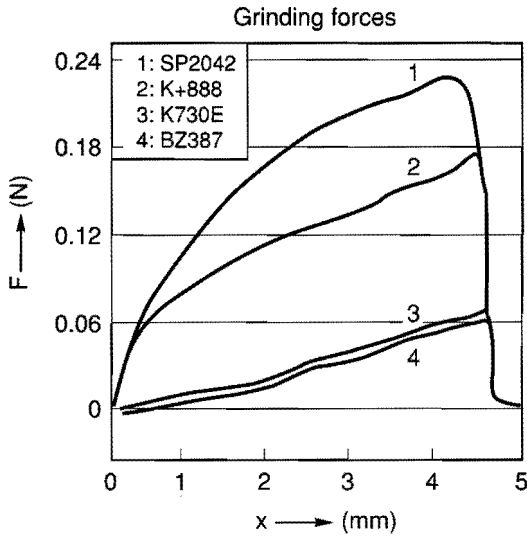


**Fig. 4.10** Grinding forces during second cuts, in tests on glass, using four different wheels (nominal conditions).

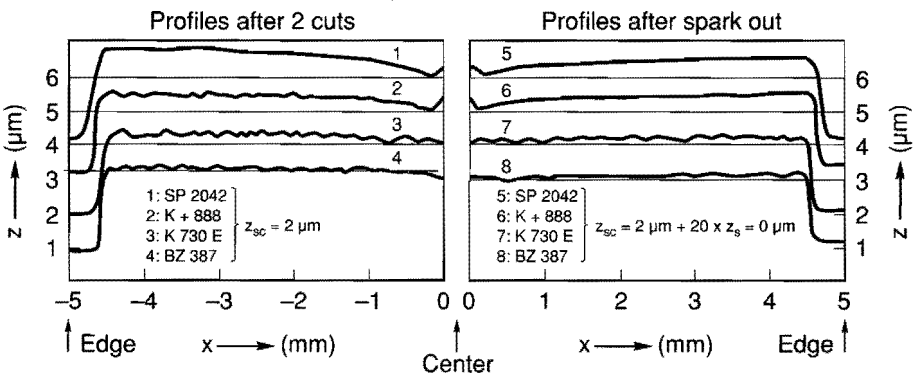


**Fig. 4.11** Ground profiles after 2 cuts with  $1 \mu\text{m}$  infeed, (1 to 4) and after 20 spark-out (5 to 8), 4 different wheels, nominal conditions.

*Effect of part material (glass and steel).*

Grinding tests on steel parts yield results very similar to those on glass. In general, the maximum force under similar conditions is roughly a factor two higher when grinding steel. Consequently, the profile errors generated by compliance effects are also larger.

With glass, a complication is the transition from the ductile to the brittle material removal mode (chapter 3 of this thesis). With a large infeed, or when the cumulative depth of cut  $z_{pc}$  has become too large, fracture mode grinding is promoted. This results in significant (sub)surface damage, a lower grinding force and a much rougher part surface.

*Effect of the machine infeed  $z_s$ .*

The multi-cut procedure (5 times a uniform infeed  $z_s$ ) was executed on glass, using the resin bond wheels under nominal conditions a number of times, for various values of  $z_s$ .

Fig. 4.12 shows the profiles obtained with the K730E wheel. The total profile error is seen to increase substantially with increasing infeed  $z_s$ . The results obtained with the K+888 wheel are similar.

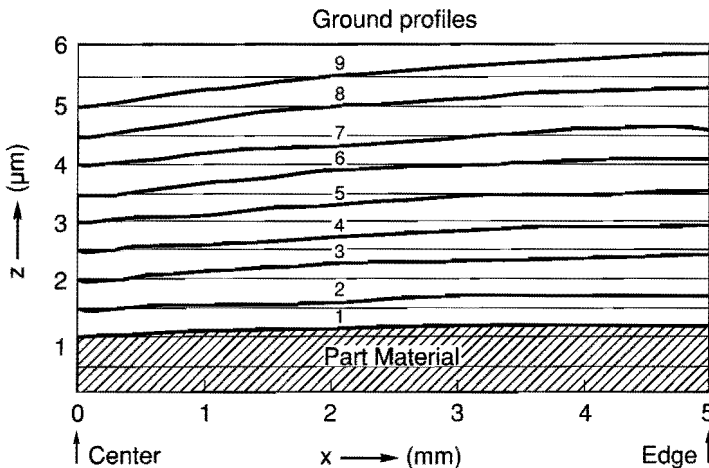


**Fig 4.12** Profiles ground (after 5 cuts) with different infeeds  $z_s$ .

- 1:  $z_s=0.1 \mu\text{m}$ , 2:  $z_s=0.25 \mu\text{m}$ , 3:  $z_s=0.5 \mu\text{m}$ , 4:  $z_s=0.75 \mu\text{m}$ , 5:  $z_s=1 \mu\text{m}$ , 6:  $z_s=1.25 \mu\text{m}$ , 7:  $z_s=1.5 \mu\text{m}$ , 8:  $z_s=1.75 \mu\text{m}$ , 9:  $z_s=2 \mu\text{m}$ .



To improve the accuracy of the profile grinding process, it is very important to understand these effects more quantitatively. In the following sections, a theoretical model to explain these phenomena will be developed.

### *Conclusions.*

The conclusions drawn from the experiments can be summarized as follows:

- Compliance effects are the main cause of profile errors in contour grinding (after reduction of thermal errors to sub-micron level).
- In a multi-cut procedure with equal infeed per pass, the grinding force and the profile error increase in successive cuts, due to the residue (cumulative profile error) left in foregoing passes (memory effect).
- The number of foregoing cuts that contributes significantly to the profile error after a multi-cut procedure depends on the resilience of the grinding wheel, the condition of the grinding wheel and the machine stiffness.
- The magnitude of the deflections in the structural loop and the resulting profile errors depend on the resilience of the wheel matrix. This quantity is not necessarily the same as the wear hardness found in the catalogue of a grinding wheel manufacturer, since the details of the contact geometry also influence the wheel stiffness.
- The grinding wheel condition after reconditioning is a major source of variance in the test results. This makes it dubious to draw definite conclusions regarding the effects of the feed rate and the part speed upon the grinding forces and the profile errors.
- Given a grinding wheel between reconditioning operations, the compliance effects are deterministic and repeatable. This means that, when grinding small parts, wear is not a crucial factor and the force-displacement relation for a grinding wheel stays the same for a relative long period of time.

The experimental results indicate that the profile errors generated in a number of cuts could perhaps be predicted by a theoretical model of the process, and even more valuable, corrected for. This will be investigated next.

## 4.6. Theory, non-linear model and simulation of profile grinding.

The effects of the influence factors introduced qualitatively in section 4.4 will be investigated more quantitative. After the development of quantitative relations for the different effects, they are bundled in a cohesive model and used to simulate the contour grinding process.

### 4.6.1. Physics and mechanics of the model.

#### *Machine compliance.*

Referring to Fig. 4.3, the headstock and grinding spindle compliances are modeled as linear springs placed in series.

The machine displacement  $u_m$  due to the compliances of the spindles for a given grinding force  $F$  is

$$u_m = \frac{F}{k_h} + \frac{F}{k_s} \quad \{4.5\}$$

where  $k_h=60 \text{ N}/\mu\text{m}$  and  $k_s=0.7 \text{ N}/\mu\text{m}$  are the stiffness of the headstock and grinding spindle respectively, measured in the critical z-direction, on the part center-height.

The spindle stiffness of  $0.7 \text{ N}/\mu\text{m}$  is very small compared to any other stiffness on the machine, and a stiffer spindle can be expected to enhance the profile accuracy in contour grinding considerably.

#### *Immersed area of the grinding wheel.*

During a grinding cut, the grinding wheel is partly immersed in the material. The projection of the contact area in the x-z plane, seen in Fig. 4.13 as the hatched area, (also called immersed or interfering section A) depends on the grinding wheel radius  $R_w$ , the feed rate  $f$  (in mm/part revolution) and the actual depth of cut  $z_a$ . In reality, the ratio of  $z_a$  and  $R_w$  is much smaller than suggested by Fig. 4.13.

The immersed area is bounded by the contours  $f(x)$  and  $g(x)$  which describe the outline of the cutting edge during two successive revolutions of the part, and the part surface before the current cut.

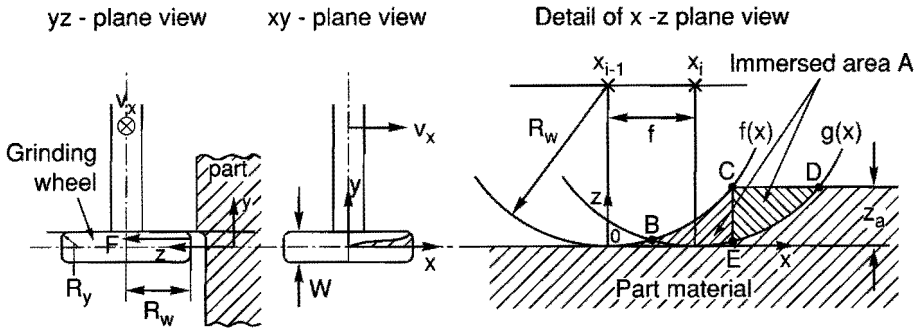


**Fig. 4.13** *The immersed area  $A$  depends on the grinding wheel radius  $R_w$ , the feed rate  $f$  and the actual depth of cut  $z_a$ .*

In Appendix 4.1 the relation between  $R_w$ ,  $f$ ,  $z_a$ , and the immersed Area  $A$  is derived.

$$A = f \cdot z_a - \frac{f^3}{24 \cdot R_w} \quad \{4.6\}$$

The feed rate  $f$  in mm/rev follows from

$$f = \frac{60 \cdot v_x}{N_p} \quad \{4.7\}$$

with  $v_x$  the feed rate in mm/s, and  $N_p$  the part speed in rpm. Eq. {4.6} is valid over a wide range, limited by (Appendix 4.1):

$$f \leq 2 \cdot \sqrt{2 \cdot R_w \cdot z_a} \quad \{4.8\}$$

This implies that eq. {4.6} is valid only if the interfering sections in successive revolutions of the part overlap.

The sensitivity of  $A$  to changes in the feed rate  $f$ , depth of cut  $z_a$  and grinding wheel radius  $R_w$  can be seen in Fig. 4.14, Fig. 4.15 and Fig. 4.16. It appears that  $A$  increases (practically) linear with both  $z_a$  and  $f$  over the range of interest, and  $A$  is equally sensitive to these parameters.

The immersed area  $A$  is a non-linear function of  $R_w$ , and  $f$ , but the non-linearity is negligible for realistic values of  $z_a$ ,  $R_w$  and  $f$ . The \* positions in the figures denote "mid-range" values for grinding practice,  $f=10 \mu\text{m}/\text{part rev.}$ ,  $z_a=1 \mu\text{m}$ ,  $R_w=4 \text{ mm}$ .

The conclusions from this sensitivity analysis are:

- The effects of  $z_a$  and  $f$  on  $A$  are comparable in magnitude and (practically) linear within the range of interest.
- The (non-linear) dependence of  $A$  on  $R_w$  and  $f$  can be neglected; the second term in eq. {4.6} is much smaller than the first, and variations in  $R_w$  are insignificant. (so grinding wheel wear for example will not affect  $A$  considerably).

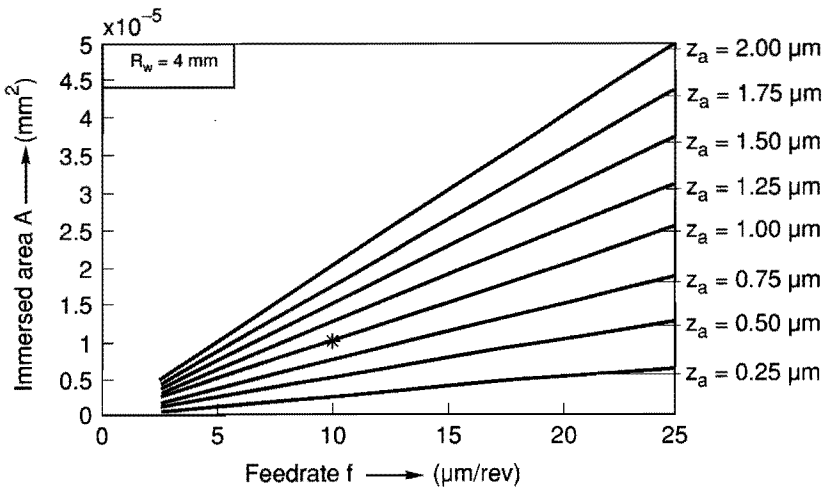


Fig. 4.14 Immersed Area as function of  $f$ , for various values of  $z_a$ .

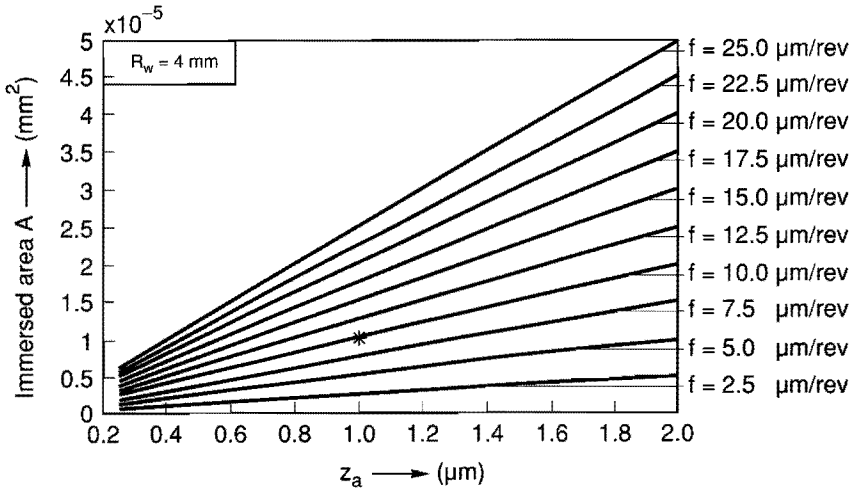


Fig. 4.15 Immersed area as function of  $z_a$  for various values of  $f$ .

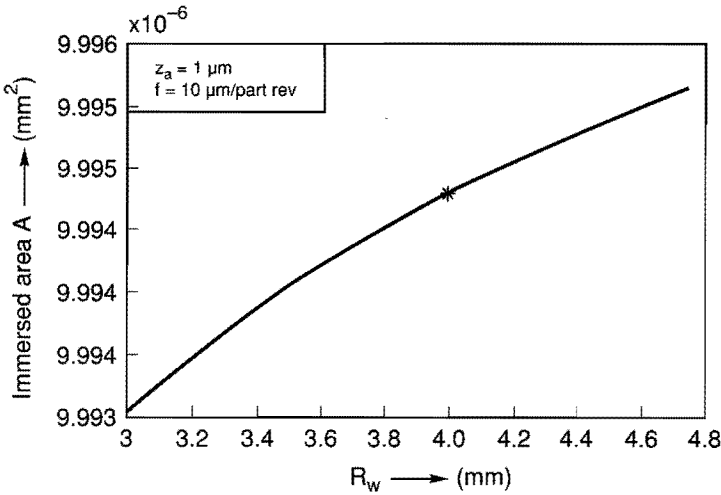
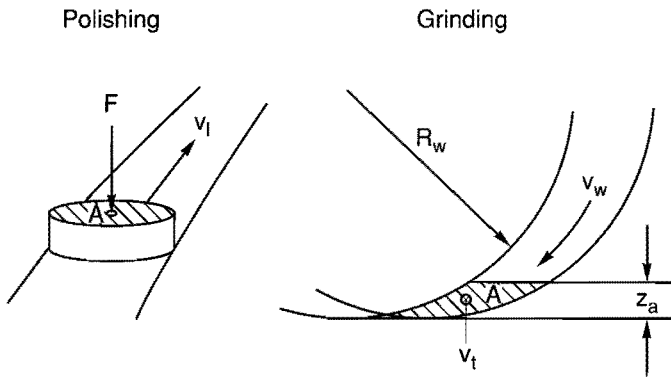


Fig. 4.16 Immersed area as function of  $R_w$ .

**Material removal and grinding force.**

The part material is removed by an abrasive wear process. The relation between the immersed area  $A$ , the removal rate  $dV/dt$  ( $\text{mm}^3/\text{s}$ ) and the grinding force  $F$  can be derived using the relation known in tribology as Archard's law (Rabinowicz 1965, Archard 1980, Zum Gahr 1983), in polishing as Preston's (Preston 1927) equation.



**Fig. 4.17** Comparison of the contact area and wear situation in polishing and grinding.

In Fig. 4.17, the contact and wear situations in polishing and grinding are shown schematically. In polishing (or in a pin-on-disk wear test), a lap has a contact area  $A$  with the part. If it is loaded with a force  $F$  and the lap travels over the part with a speed  $v_l$ , the wear rate  $dh/dt$  is given by Preston's equation:

$$\frac{dh}{dt} = C \cdot \frac{F \cdot v_l}{A \cdot H} \quad \{4.9\}$$

with  $C$  a constant, depending on material properties and details of the contact and abrasive geometry. (The constant  $C$  for instance takes into account the difference between the true area of contact and the projected area of contact  $A$ ).  $H$  represents the hardness of the part material. Equation {4.9} can be manipulated to express that the volume of material removed per unit time  $dV/dt$  is proportional to the applied load  $F$ .

$$\frac{dV}{dt} = A \cdot \frac{dh}{dt} = \frac{C \cdot v_t \cdot F}{H} \quad \{4.10\}$$

The comparison of polishing and contour grinding reveals analogical quantities in these processes. In grinding, the immersed area  $A$  corresponds to (the projection of) the contact area under the lap in polishing, the speed corresponding to the lap speed in the polishing situation is the cutting speed  $v_w$ , determined by the angular velocity and the grinding wheel radius. The volume of part material removed per unit time corresponding to  $dV/dt$  in polishing is determined by the product of  $A$  and the tangential velocity of the part material  $v_t$ . The equivalent of Preston's equation for the grinding situation thus becomes

$$\frac{dV}{dt} = A \cdot v_t = \frac{C \cdot v_w \cdot F}{H} \quad \{4.11\}$$

In eq. {4.11},  $v_w$  and  $C$  are constant, so the important result is obtained that in the contour grinding situation, the grinding force  $F$  can be expected to be a linear function of the material removal rate  $dV/dt$ .

This suggests that by varying the part speed and feed rate so as to keep the material removal rate constant as the wheel is moved over the part, the force might be kept approximately constant. This would in turn lead to a more uniform profile error.

The constant  $C$  in Preston's (or Archard's) equation is usually determined experimentally. Theoretical models of friction and wear can be found in the literature developed to predict this constant from fundamental properties of the materials in contact (Halling 1983). These models enhance our insight in wear phenomena, but their practical application is hampered by the fact that they generally contain many uncertain parameters which would have to be determined experimentally. In the present study it was decided to determine  $C$  experimentally. This can be done by applying eq. {4.11} to experimental results.

For a surface profile ground in an arbitrary grinding cut,  $dV/dt$  can be calculated accurately and  $F$  is measured during the experiment, so  $C$  can be determined. The result of such a procedure using the forces and profiles generated in two different cuts during a grinding experiment is shown in Fig. 4.18. The assumption that  $F$  is proportional to  $dV/dt$  is seen to be reasonable. The deviation in the center of the part is due to the fact that in that region, the grinding wheel starts to overlap the center of the part, and other

effects come into play. The parameter  $C$  in the grinding situation implicitly accounts for the difference between the total area of contact and the projected (immersed) area of contact  $A$  (Fig. 4.3).

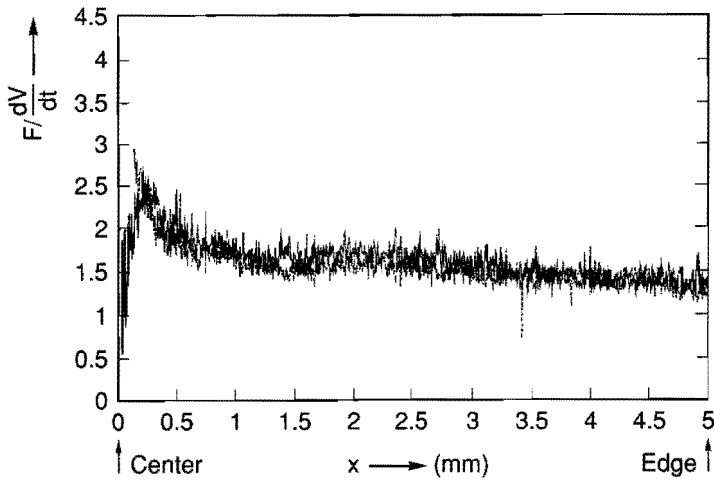


**Fig. 4.18** From a grinding experiment, the ratio of  $F$  and  $dV/dt$  has been determined (two different cuts). It is virtually constant, except close to the center of the part where other effects dominate.

#### *Grinding wheel deflection.*

The final step in deriving the model is to quantify the interaction between the tool and the part. The grinding wheel wear rate is low, supporting the generally accepted view that the contact is elastic from the point of view of the grinding wheel. The contact pressure distribution is approximately elliptical, following Hertz's equations for a line or an elliptical contact situation. The irregular grinding wheel surface can be expected to modify the contact pressure distribution (Greenwood et. al. 1984, Kagami 1983, and Tangena 1987). These modifications result in a broadening of the contact patch (compared to the Hertz situation).

The overall force, and the total deflection are still comparable to those in a Hertz contact situation where a normal force acts on two elastic bodies in contact. The slip in the contact zone (the tangential velocity of the grinding



wheel) is generally considered to generate shear stress in the contact zone. This alters the stress distribution in the materials in contact considerably.

However, it does not affect the normal pressure in the contact area, so the total wheel deflection will not be influenced significantly.

*Wheel deflection in line contact situation.*

The grinding wheels used in this study were cylindrical pellets, to approximate a line contact situation. For an arbitrary value of the grinding force  $F$ , with a grinding wheel that is much more resilient than the part material, the deflection of the grinding wheel ( $u_w$ ) in a line contact situation can be calculated as (Snoeys 1968, Johnson 1985)

$$u_w = \frac{2 \cdot F \cdot (1 - \nu^2)}{\pi \cdot E_w \cdot W} \cdot \left[ \ln \left( \frac{2 \cdot R_w}{a} \right) - \frac{\nu}{2 \cdot (1 - \nu)} \right] \quad \{4.12\}$$

with  $a$  the half width of the contact zone,

$$a = 2 \cdot \sqrt{\frac{R_w \cdot F \cdot (1 - \nu^2)}{\pi \cdot E_w \cdot W}} \quad \{4.13\}$$

$E_w$  is the modulus of elasticity,  $\nu$  Poisson's ratio of the grinding wheel ( $\approx 0.3$ ) and  $W$  is the width of the line contact (dimension in the  $y$  direction).

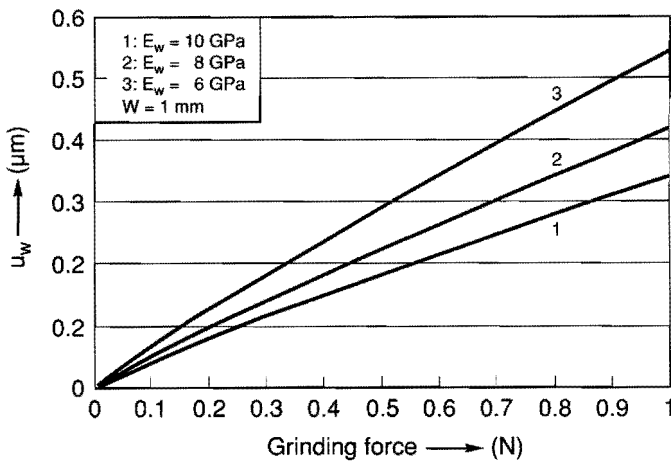


**Fig. 4.19** Calculated grinding wheel deflection  $u_w$  as a function of  $F$  (line contact situation).

The grinding wheel deflection  $u_w$  as a function of the grinding force  $F$  can be seen for various values of the grinding wheel's modulus of elasticity in Fig. 4.19. The value of 8 GPa was experimentally determined for the K+888 wheels, the other values were chosen to investigate the sensitivity of the wheel deformation to changes of the modulus of elasticity. The wheel deflection is a non-linear function of the grinding force.

The sensitivity of  $u_w$  to variations in  $F$  and the modulus of elasticity  $E_w$ , and the severity of the non-linearity should be seen in connection with the machine compliance. In Fig. 4.20, the grinding wheel and the machine deflections  $u_w$ ,  $u_m$  and their sum  $u_t$  can be seen for  $E_w$  values which are realistic for resin bond grinding wheels, an estimated contact width  $W=1$  mm, headstock and spindle stiffness of the ESDO and practical grinding force values.

The wheel deflection is a substantial fraction of the total displacement. However, the machine deflection is larger. The total displacement and the share of the wheel deflection becomes larger if the contact width  $W$  becomes smaller.

The non-linearity of the wheel deflection as a function of the grinding force for the line contact situation is almost insignificant over the grinding force range of practical interest. This has important implications which will be discussed in section 4.7.

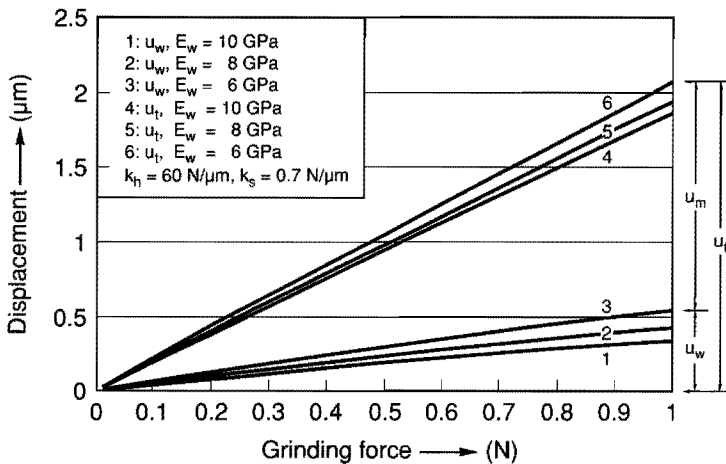


Fig. 4.20 Calculated wheel deflection  $u_w$  compared to the machine ( $u_m$ ) and total deflection  $u_t$  (line contact situation).

*Wheel deflection in elliptical contact situation.*

In practice, grinding wheels are often contoured to give the cutting edge a defined radius. Even the cylindrical pellets used in the current study will have some finite radius, so the contact situation will be elliptical to some extent. For this situation, again under the assumption that the grinding wheel is much more resilient than the part, the deflection due to the contact compliance can be approximated (Johnson 1985) as

$$u_w = \left( \frac{9 \cdot F^2}{16 \cdot \sqrt{R_w \cdot R_y}} \right)^{1/3} \cdot \left( \frac{1 - \nu^2}{E_w} \right)^{2/3} \quad \{4.14\}$$

with  $R_y$  the radius of the cutting edge in the  $y$ - $z$  plane. In Fig. 4.21, the wheel deflection in the line ( $R_w=1$  mm,  $W=1$  mm) and elliptical contact situation can be compared ( $R_w=4$  mm and  $R_y=1$  mm).

The wheel deflection in the elliptical contact situation is larger for a given force, and the non-linearity of the force compliance relation is more severe.

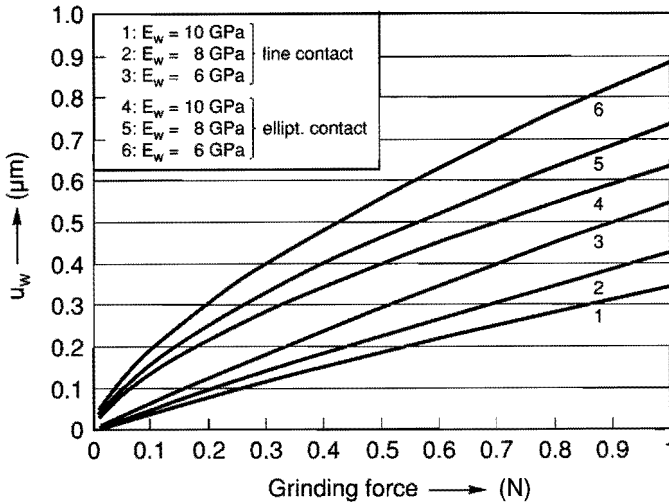


**Fig. 4.21** Grinding wheel deflection for a line contact situation ( $R_w=4$  mm,  $W=1$  mm) compared to an elliptical contact situation ( $R_w=4$  mm,  $R_y=1$  mm).

*Conclusions regarding contact situation and wheel deflection.*

The comparison between the line and elliptical contact situation and the resulting compliance should be made considering at the same time the machine compliance. For  $E_w=6$  GPa,  $R_w=4$  mm,  $W=1$  mm,  $R_y=1$  mm,  $k_s=0.7$  N/ $\mu$ m and  $k_b=60$  N/ $\mu$ m this comparison is shown in Fig. 4.22. The wheel deflection for the elliptical contact situation starts to dominate the overall cutting edge displacement if the grinding force becomes very small. In that case, the non-linearity of the force-displacement relation is also quite severe, especially for the elliptical contact situation.

In practice, at the center of the part, the grinding force always becomes very small. The experimentally observed non-linearity of the grinding force and the ground profiles close to the center (Fig. 4.2, Fig. 4.4 and Fig. 4.5), when grinding with compliant resin bond wheels, indicates that it is more realistic to assume an elliptical contact situation than to assume a line contact.

With very stiff grinding wheels, the wheel deformation is negligible compared to the machine deflection, and the force-total displacement relation becomes practically linear.

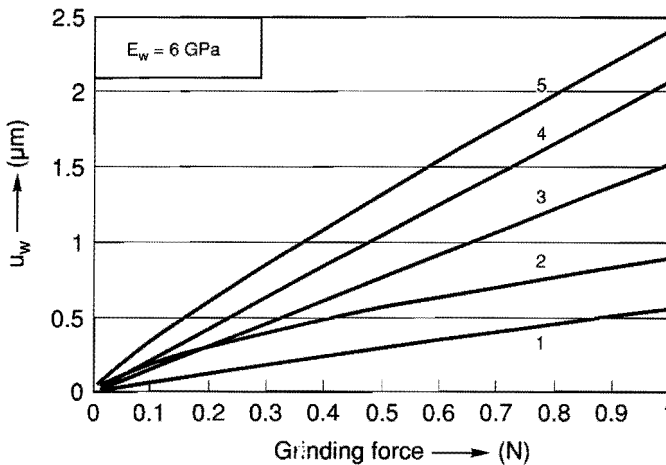


**Fig. 4.22** Wheel deflection  $u_w$  for line (1), and elliptical contact situation (2), machine deflection  $u_m$  (3), total deflection  $u_t$ , for line (4) and elliptical contact situation (5).

#### 4.6.2. Simulation of profile grinding.

All elements having been described quantitatively, they are combined to form a cohesive model of the contour grinding process. The equations discussed in foregoing sections used in the simulation are summarized in Appendix 4.2 and the flow-chart in Fig. 4.24.

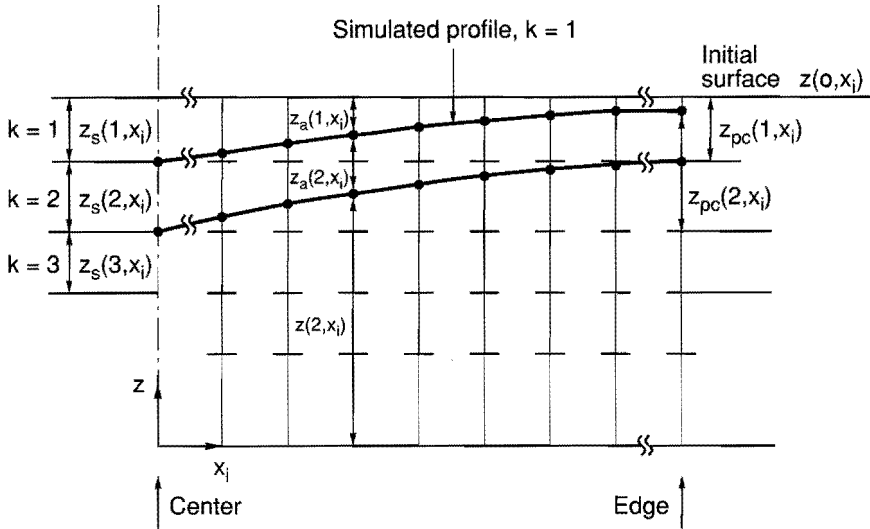


**Fig. 4.23** Machine infeed  $z_s(k, x_i)$ , cumulative depth of cut  $z_{pc}(k, x_i)$  and actual depth of cut  $z_a(k, x_i)$  at position  $x_i$ , pass  $k$ .

Equally spaced  $x$  positions (index  $i$ , spacing  $f$ ) in radial direction (Fig. 4.23), and an arbitrary number of passes (index  $k$ ) are considered. The cumulative machine infeed  $z_{sc}(k, x_i)$  with respect to an initial surface  $z(0, x_i)$ , in pass  $k$  at position  $x_i$  is represented by  $z_{sc}(k, x_i)$ , given by eq. {4.2}. The cumulative depth of cut experienced by the material  $z_{pc}(k, x_i)$ , is given by eq. {4.4}, so the amount of material actually left behind during former cuts is taken into account.

During each pass  $k$ , at each position  $x_i$ , the actual depth of cut  $z_a(k, x_i)$  is determined by the following iterative procedure (Fig. 4.24):

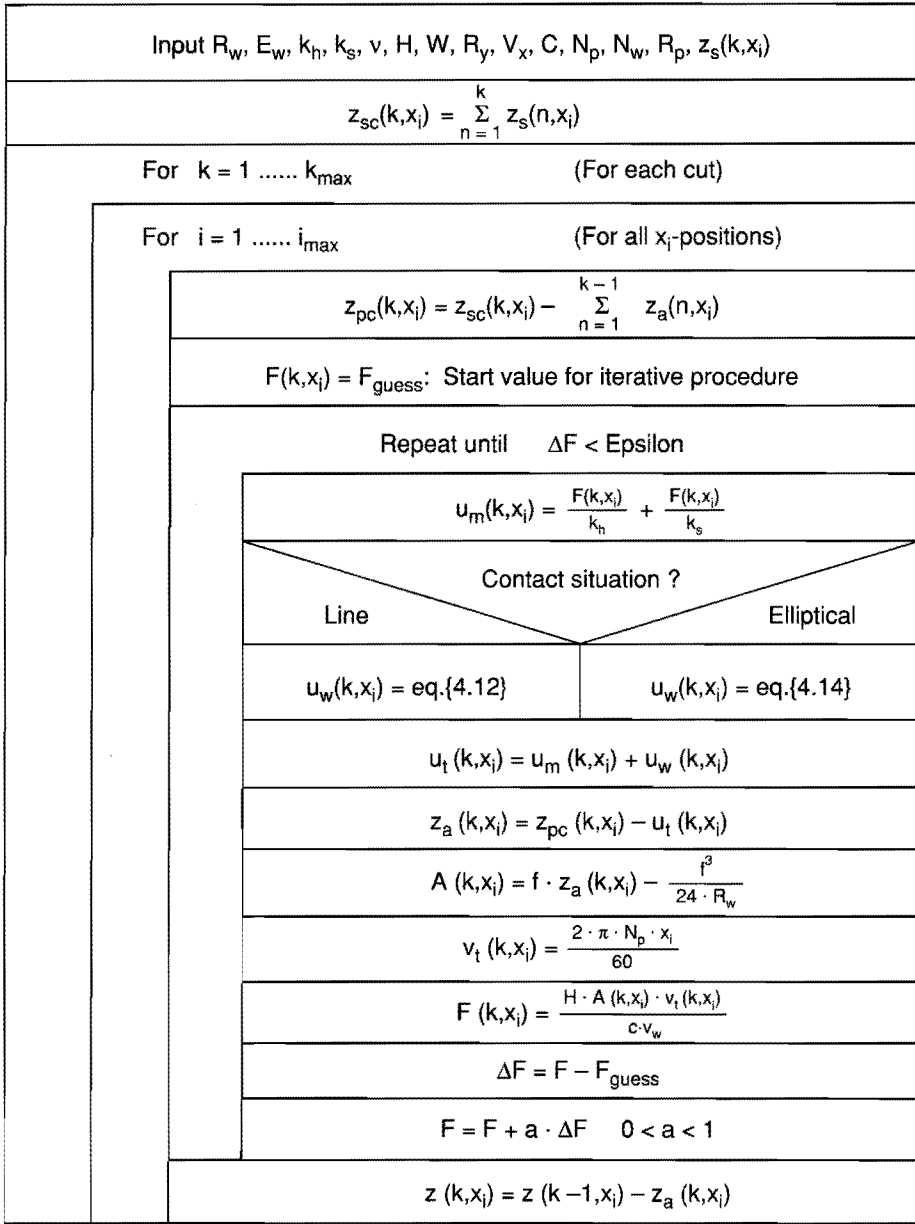


**Fig. 4.24** Structure diagram of the contour grinding simulation. The program was written in PC-Matlab, standard routines were used to solve the equations.

- 1) With a guess value for  $F(k, x_i)$ , and the known values for  $R_w$ ,  $E_w$ ,  $k_b$ ,  $k_s$  and  $v$  as input, the deflection of the machine  $u_m(k, x_i)$  is calculated using eq. {4.5}. The grinding wheel  $u_w(k, x_i)$  is calculated using eq. {4.12} or {4.14}, depending on whether a line contact or elliptical contact situation is assumed.

The total deflection  $u_t(k, x)$  is determined as

$$u_t(k, x_i) = u_w(k, x_i) + u_m(k, x_i) \quad \{4.15\}$$

- 2) With  $R_w$  and  $f$  known, and the value of  $u_t(k, x_i)$  determined in step 1, the actual depth of cut  $z_a(k, x_i)$  is estimated as:

$$z_a(k, x_i) = z_{pc}(k, x_i) - u_t(k, x_i) \quad \{4.16\}$$

- 3) With the estimate for  $z_a(k, x_i)$ , the immersed area  $A(k, x_i)$  is calculated from eq. {4.6}.
- 4) A new estimate for the grinding force  $F(k, x_i)$  is calculated using the assumed value of the constant  $C$  and the value for  $A(k, x_i)$  calculated in the former step using eq. {4.11}.

A new guess value for  $F$  is determined, and steps 1 through 4 are repeated until convergence of  $F(k, x_i)$ ,  $u_t(k, x_i)$  and  $z_a(k, x_i)$  is achieved.

- 5) The surface profile ground,  $z(k, x_i)$  is finally found by setting

$$z(k, x_i) = z(k-1, x_i) - z_a(k, x_i) \quad \{4.17\}$$

In the next section, some results of simulations performed in this manner will be presented.

#### 4.6.3. Results and discussion of simulations.

The results of simulations presented in this section are not meant to produce results which correspond exactly with experimental results. Simulations would have to be done adapting the width of the contact area ( $W$ ) and the wear coefficient  $C$  (eq. {4.11}) to make the simulations match the experimental data.

However, such a procedure does not improve the predictive power of the model in any way, since adapting  $C$  would in effect take into account the

variance in the surface condition of the grinding wheel after reconditioning.

Rather than to follow such a procedure, the uncertainties regarding the numerical values of these parameters in the model are accepted for now, and the effects of those variables that could be varied experimentally are reported here.

In section 4.7, a simple method to circumvent the uncertainties associated with the numeric values of the model parameters and make the model useful in a predictive sense will be discussed. All simulations presented here were carried out taking  $H_v=5500$  MPa,  $N_w=40.000$  rpm and  $C=1 \cdot 10^{-3}$ .

*Simulations assuming a line contact situation.*

Forces and profiles simulated with *nominal values* for the parameters  $R_w$ ,  $v_x$ ,  $E_w$ ,  $k_h$  and  $k_s$  and  $W$  (assuming a line-contact situation) can be seen in Fig. 4.25 and Fig. 4.26. Four cuts are simulated, each with an infeed  $z_s=1 \mu m$ . After the first "cut", the profile is slightly non-linear.

The force calculated in subsequent passes is seen to increase, until a steady state situation is approached. This has also been observed in practice. The profiles generated in consecutive cuts become straighter. In practice this has been observed when using a bronze bond grinding wheel and with the less resilient resin bond grinding wheels.

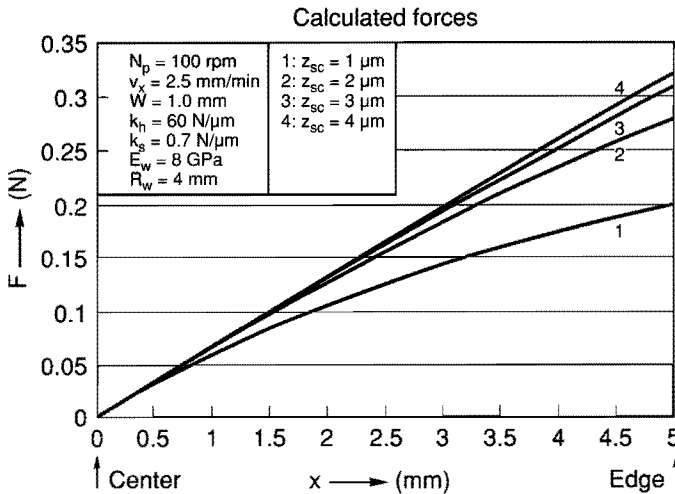


**Fig. 4.25** Forces during simulation of equal uniform infeeds ( $z_s=1 \mu m$ ) each cut. The cumulative infeed  $z_{sc}$  increases from  $1 \mu m$  (curve 1) to  $4 \mu m$  (curve 4). Line contact situation.



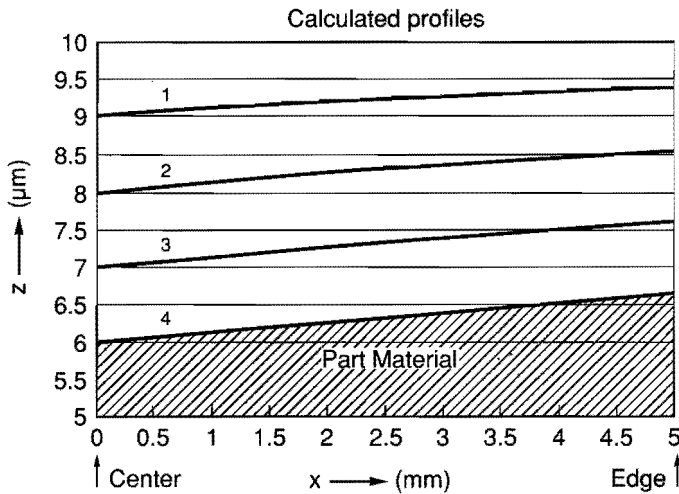


**Fig. 4.26** Surface profiles calculated in simulation of multi-cut grinding operation.  $z_{sc}$  increases from  $1\ \mu\text{m}$  (curve 1), to  $4\ \mu\text{m}$ , (curve 4). Line contact situation.

The simulated combined effect of a *more resilient binder and a smaller contact width* is seen by comparing Fig. 4.27 and Fig. 4.28 to Fig. 4.25 and Fig. 4.26. (Same cutting procedure of  $1\ \mu\text{m}$  infeed each cut as before was simulated). The total profile error is larger with the more resilient wheel, the curvature of the ground profiles is more pronounced and the steady state is approached at a lower rate.

*The contact width  $W$*  influences the relative contribution of the wheel and machine deflection significantly. A smaller contact width results in a larger wheel deformation and more pronounced non-linear profiles. This can be seen by comparing Fig. 4.29 and Fig. 4.30 to Fig. 4.27 and Fig. 4.28. (Same cutting procedure consisting of 4 equal infeeds, each  $z_s=1\ \mu\text{m}$  simulated).

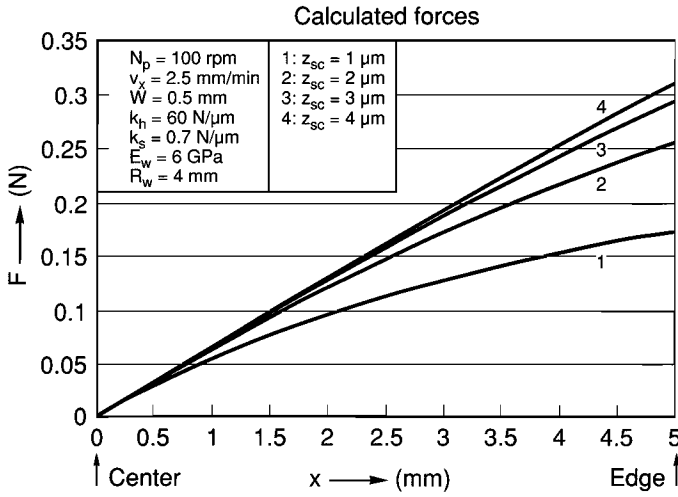


**Fig. 4.27** Force simulated with a more resilient grinding wheel and a smaller contact width  $W$  (line contact situation).

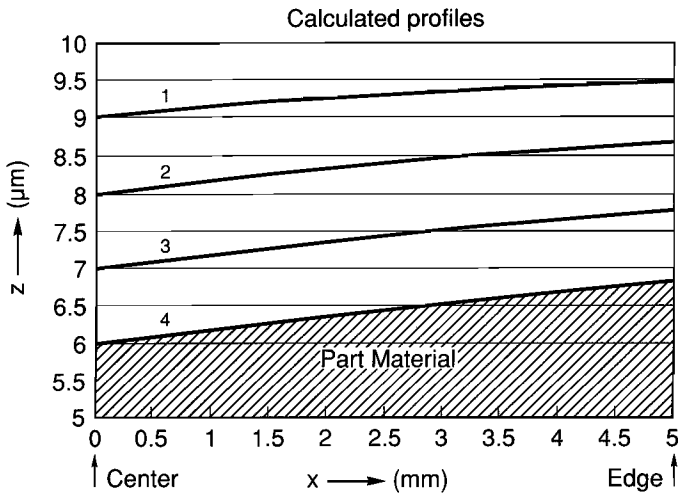


**Fig. 4.28** Profiles calculated in simulation of grinding with a more resilient grinding wheel and smaller contact width (line contact situation).

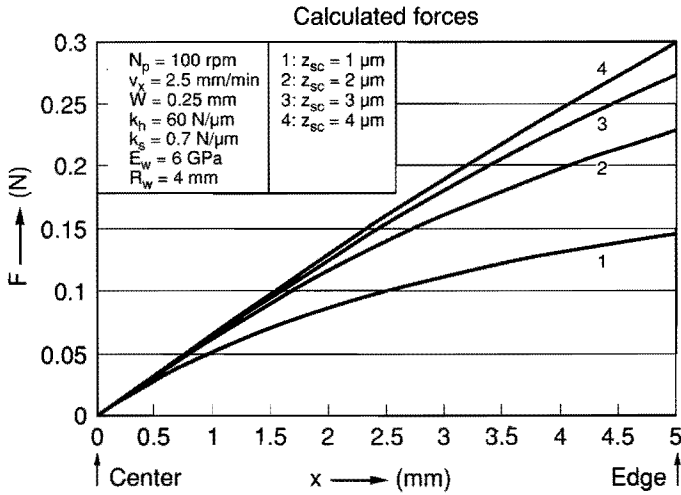


Fig. 4.29 Forces calculated assuming a low value for  $W$  (line contact situation).

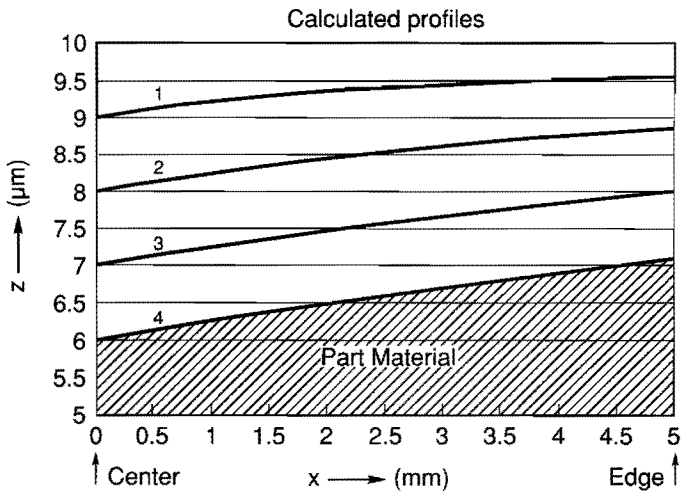


Fig. 4.30 Profiles calculated with a low value for  $W$  (line contact situation).



The simulation technique is a very useful tool to clarify the effects and the sensitivity of the process to changes in process variables or machine stiffness.

However, the model contains a number of parameters ( $C, W, R_s$ ) whose numerical value is difficult to determine from experiments. Furthermore, in practice, the surface condition of the grinding wheel causes considerable variance in the value of these parameters, so they would have to be determined quite frequently (basically every time after reconditioning the wheel).

The nearly linear relation between force and deflection makes it feasible to formulate a linear theory to describe the grinding process, which contains only one parameter that can be determined experimentally quite simple. This linear theory will be discussed in the next section.

## 4.7. Analytic model of contour grinding and cutting.

### 4.7.1. Linear process model.

From the sensitivity analyses regarding  $A(f, R_w, z_a)$  and  $u_t(k_a, k_b, E_w, F)$  reported in section 4.6.1, it has become apparent that the non-linearities associated with the contact situation are small. If the non-linear effects are neglected, the force-total displacement relation simplifies to

$$u_t = C_2 \cdot F \quad \{4.18\}$$

with  $C_2$  a constant, and the non-linear model presented in section 4.6. simplifies to a set of linear equations (summarized in appendix 4.2). Such a linear model predicts a number of trends which in hindsight almost seem trivial, and will be mentioned only for completeness.

- The grinding force  $F$  (component perpendicular to the ground surface) can be expected to be proportional to the actual depth of cut  $z_a$ , the feed rate  $f$  and to the part speed  $N_p$  (at constant  $f$ ).
- The grinding force is predicted to be inversely proportional to the wheel speed  $N_w$ .

With a linear process model it becomes possible to:

- Find an analytical expression for the degree to which the cutting edge truly follows the slide motion (motion copying ability of the combination machine and process).
- Derive analytical expressions to predict the achievable accuracy of an arbitrary multi-cut procedure for a given machine and grinding wheel stiffness.
- Investigate the "memory effect" in contour grinding (how many passes are needed to reach a stable situation).
- Calculate the number of spark-out cuts needed to reduce a form error to a specified value (Tlustý 1972).
- Specify an infeed profile to compensate for the profile error due to compliance effects (feed forward) and grind a desired profile more accurate, and more efficient (shorter production time).

In this section, the focus is on the effects of multiple cuts. The infeed and cumulative depth of cut, at an arbitrary  $x$  position, are considered. This means that the factor  $p$  which will be introduced next can be treated as a constant value (for a given value of  $x$ ), and the indices  $k$  and  $n$  are used in the following formulas to indicate the number of cuts. In the next section the dependence of  $p$  on the position  $x$  is also considered.

In Appendix 4.2, it is shown that the linear model predicts that the actual depth of cut  $z_a(k)$  for a given value of  $v_t$  (given  $x$  position) is a constant fraction ( $p$ ) of the cumulative depth of cut experienced by the material  $z_{pc}(k)$ , in cut number  $k$ .

$$z_a(k) = p \cdot z_{pc}(k) \quad 0 \leq p \leq 1 \quad \{4.19\}$$

The residue (profile error  $e(k)$  after cut number  $k$ ) can also be defined:

$$e(k) = (1-p) \cdot z_{pc}(k) \quad \{4.20\}$$

The numerical value of  $p$  can be expressed as (see also Appendix 4.2)

$$p = 1 - \frac{C_2 \cdot f \cdot N_p \cdot x \cdot H}{N_w \cdot R_w \cdot C + C_2 \cdot f \cdot N_p \cdot x \cdot H} = \frac{N_w \cdot R_w \cdot C}{N_w \cdot R_w \cdot C + C_2 \cdot f \cdot N_p \cdot x \cdot H} \quad \{4.21\}$$

which shows how  $p$  depends on the resilience of the wheel, the geometry of the contact area and the machine stiffness (expressed by  $C_2$ ), the wheel and part size and speeds (via  $N_w$ ,  $R_w$ ,  $N_p$  and  $x$ ), and the hardness of the part ( $H$ ).

For accurate contour grinding,  $p$  should be high. The closer  $p$  is to 1, the better the actual cutting depth corresponds to the machine infeed. Therefore,  $p$  is called the motion copying ability for the combination of machine and process.

Equation {4.21} indicates that to get  $p$  close to 1, the first term in the denominator should be made larger than the second. Equation {4.21} shows how the machine, grinding wheel and process parameters can be manipulated to achieve this in practice. For  $p$  close to 1, eq. {4.21} can be simplified further (Appendix 4.2, eq. {A4.2.21}) and  $p$  becomes nearly linear in  $x$ .

For low values of  $p$ , the character of the operation changes from grinding to polishing. In that regime, the motion copying ability is low and the material removal becomes determined by the dwell time of the tool rather than the slide motions.

To make the following expressions more widely applicable, the variables with dimension length can be considered to be normalized with respect to an arbitrary value of the infeed per pass  $z_s(k)$ . Normalized quantities are indicated by a  $\tilde{\phantom{x}}$  symbol.

For a series of cuts, consisting of equal machine infeeds  $z_s(k)$ , the cumulative depth of cut  $z_{pc}(k)$  in an arbitrary pass consists of the sum of  $z_s(k)$  (for that particular cut) and the residue left after the preceding pass. Alternatively, it can be stated that in cut number  $k$ , the intended depth of cut is equal to  $kz_s(k)$  diminished with the total amount of material actually removed at that location in foregoing passes. The actual (dimensionless) depth of cut in pass  $k$ ,  $\tilde{z}_a(k)$ , will again be a fraction  $p$  of this cumulative depth of cut in pass  $k$ :

$$\tilde{z}_a(k) = p \cdot \left( k - \sum_{n=1}^{k-1} \tilde{z}_a(n) \right) \quad \{4.22\}$$

If  $k$  goes to infinity,  $\tilde{z}_a(k)$  tends to 1 (Fig. 4.32). This reflects grinding practice in the sense that the actual depth of cut will, due to the compliance, always be less than, and in the limit equal to, the machine infeed. In how many passes the steady state is reached in which  $z_a(k)$  practically equals the infeed per pass  $z_s(k)$  depends on the value of  $p$  (Fig. 4.32). The number of passes it takes to reach the steady state (for say 95%) for an arbitrary  $p$  value is the "horizon" of the "memory effect" in contour grinding. It indicates the number of past cuts that, through the profile error generated in those passes, influences the form (error) of the profile ground in the current cut.

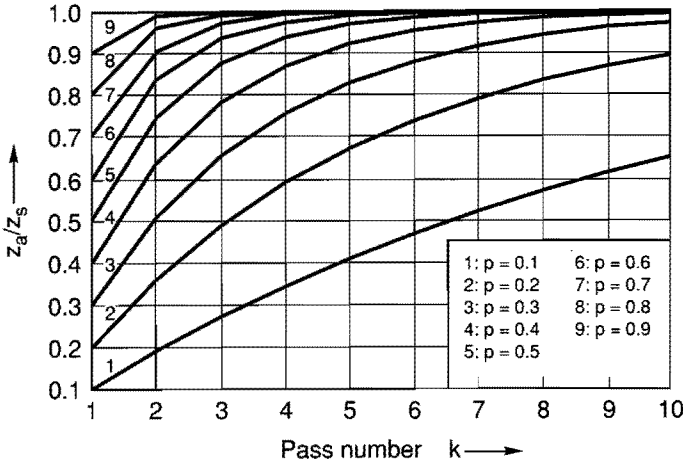


Fig 4.32 Ratio of actual depth of cut  $z_a$  and infeed per pass  $z_s$  in successive cuts for various values of  $p$ .

It is also interesting to look at the series that describes the development of the residue (total profile error  $e(k)$ ) left after subsequent passes.

The (normalized) residue  $\tilde{e}(k)$  left after pass  $k$  (total profile error) is

$$\tilde{e}(k) = (1-p) \cdot \tilde{z}_{pc}(k) = \tilde{z}_{pc}(k) - \tilde{z}_a(k) = \tilde{z}_{pc}(k) - p \cdot \left( k - \sum_{n=1}^{k-1} \tilde{z}_a(n) \right) \quad \{4.23\}$$

If  $k$  goes to infinity, this profile error  $\tilde{e}$  goes to a limit value of

$$\tilde{e}_{k \rightarrow \infty}(k) = \tilde{e}_{lim} = \frac{1}{p} - 1 \quad \{4.24\}$$

This can be made plausible by looking at the value of the cumulative depth of cut in the steady state situation, where (normalized with respect to  $z_s$ ) the actual depth of cut  $z_a$  equals the infeed per cut  $z_s$  and so

$$\tilde{z}_a(k) = p \cdot \tilde{z}_{pc}(k) = 1 = p \cdot (1 + \tilde{e}_{lim}) \quad \{4.25\}$$

Solving  $\tilde{e}_{lim}$  from eq. {4.25} gives eq. {4.24}. For  $p$  close to 1, eq. {A4.2.21} and {A4.2.22} can be substituted in eq. {4.24} and  $\tilde{e}_{lim}$  can be expressed as;



$$\text{for } p \approx 1: \tilde{e}_{\text{lim}} = \frac{C_2 \cdot f \cdot N_p \cdot H}{N_w \cdot R_w \cdot C} \cdot x \quad \{4.26\}$$

#### 4.7.2. Experimental determination of p.

The multi-cut, uniform infeed procedure can be used to determine  $p$  since after a sufficient number of cuts (see Fig. 4.32), the profile error will be practically equal to  $e_{\text{lim}}$ . To investigate how well the linear theory approximates reality, the multi-cut procedure was carried out (nominal conditions) with different values of the infeed per cut  $z_s(k,x)$ . If the linear theory is appropriate, the grinding force in corresponding cuts and the profile error  $e(k) \approx e_{\text{lim}}$  (after a sufficient number of cuts) in these tests should depend linearly on  $z_s$ .

Fig. 4.33 shows the maximum value of the grinding force during the second of a series of 5 cuts with uniform infeed, for two resin bond wheel used on glass. The profile error ( $\approx e_{\text{lim}}$ ) after 5 cuts with uniform infeed can be seen in Fig. 4.34. These graphs indeed show linear relations, supporting the idea that the linear theory adequately describes the situation.

Using eq. {4.24}, the values of  $p$  for these particular grinding wheels, in this particular shape and condition, at the edge of the 10 mm diameter part (for  $x=5$  mm) are determined as 0.71 (K730E wheel) and 0.77 (K+888 wheel).

It is noteworthy that in these tests, the K+888 wheel appears to be the stiffer of the two. From the grinding tests presented in section 4.5, the opposite was found. This again stresses the importance of the wheel conditioning operation. The form of the cutting edge and, to a lesser extent, the wheel surface condition, may alter the compliance characteristics of the wheel.

For the grinding tests on glass ( $H_v=5500$  MPa), the nominal conditions are  $v_x=2.5$  mm/min,  $N_p=100$  rpm,  $N_w=40.000$  rpm,  $R_w=4$  mm, and  $R_p=5$  mm. For the resin bond wheels used in this study, the experimentally determined contact stiffness together with the spindle stiffness suggest values for  $C_2 \approx 1$   $\mu\text{m/N}$ . The value of the wear coefficient  $C$  (also determined from experiments) is about  $5 \cdot 10^{-4}$ . With these numerical values, for  $x=5$  mm, a  $p$  factor of 0.6 is calculated using eq. {4.21}. In view of the variance associated with the dressing operation,

this agrees reasonably well with the experimentally determined values of  $p$  for the K+888 and K730 E wheels.

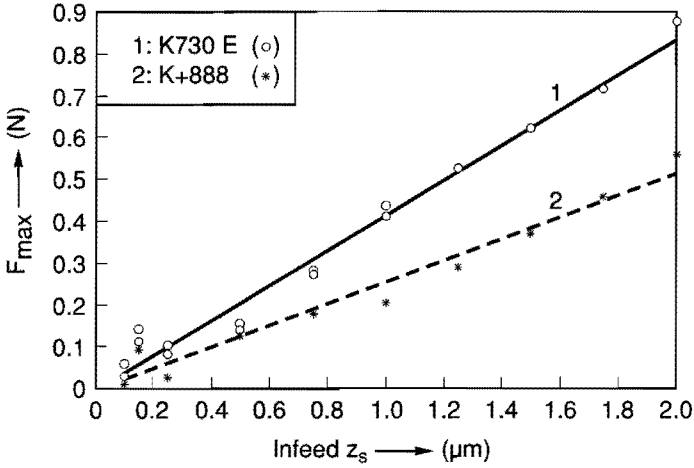


Fig. 4.33 Maximum force in second cut of multi-cut tests with uniform infeeds  $z_s$ , using resin bond wheels on glass.

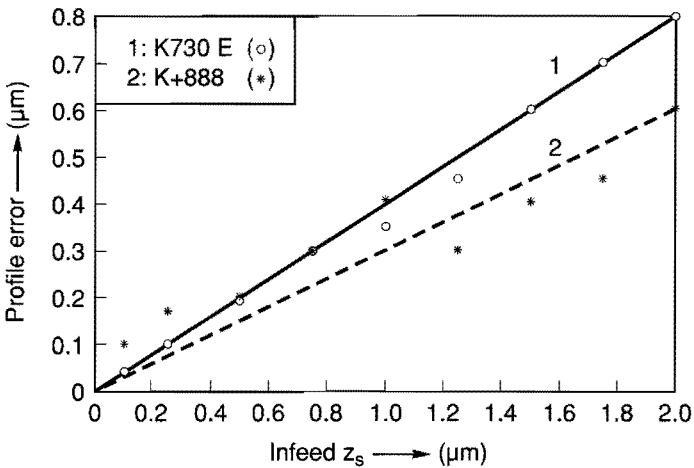


Fig. 4.34 Profile error (at the part edge) after 5 cuts with uniform infeed  $z_s$ , using resin bond grinding wheels on glass.

### 4.7.3. Implications and practical use of the linear theory.

Equations {4.19} through {4.26} have important practical implications. If the force-deflection relation for a machine-grinding wheel combination is reasonably linear, prediction of the total profile error after an arbitrary set of grinding cuts becomes feasible after some simple tests are done to determine the motion copying ability  $p$  as a function of the  $x$  position of the grinding wheel with respect to the part centerline  $p(x)$ . Such a procedure circumvents the uncertainty associated with the parameters  $C$  and  $W$  (or  $R_y$ ) in the non-linear model discussed in section 4.6. The procedure is to grind a number of cuts with equal infeed and measure the profile error as a function of  $x$  ( $e_{im}(x)$ ) when a steady state has been reached. Next, using eq. {4.24},  $p(x)$  is derived. The profile error resulting after an arbitrary cutting cycle can now be predicted using equations {4.2}, {4.3}, {4.4} and {4.23}.

Another practical use of these equations is to predict how many spark-out passes are needed to diminish a total profile error  $e_{start}(x)$  to an acceptable level by grinding over the surface without additional infeed.

In every spark-out pass (number  $n$ ) the infeed  $z_s(n,x)=0$  and the profile error  $e(n-1,x)$  at position  $x$  is reduced by a fraction  $p(x)$ . The necessary number of spark-out passes ( $n$ ) to reduce the profile error to a fraction  $a$  ( $0 < a < 1$ ) of the initial error profile  $e_{start}(x)$  can be found from the condition

$$(1-p(x))^n \cdot e_{start}(x) \leq a \quad \{4.27\}$$

which upon substitution of eq. {4.24} and solving for  $n$  yields

$$n \geq \frac{\log\left(\frac{a \cdot p(x)}{1-p(x)}\right)}{\log(1-p(x))} \quad \{4.28\}$$

The number of spark-out passes needed to reduce an initial profile error to an acceptable fraction  $a$  ( $0 < a < 1$ ) for a given  $p$  value can also be seen in Fig. 4.35.

A final and probably most important practical application of the theory presented is to generate a feed forward compensation for compliance effects in contour grinding. In this way, the infeed necessary to accurately generate a desired profile can be calculated.

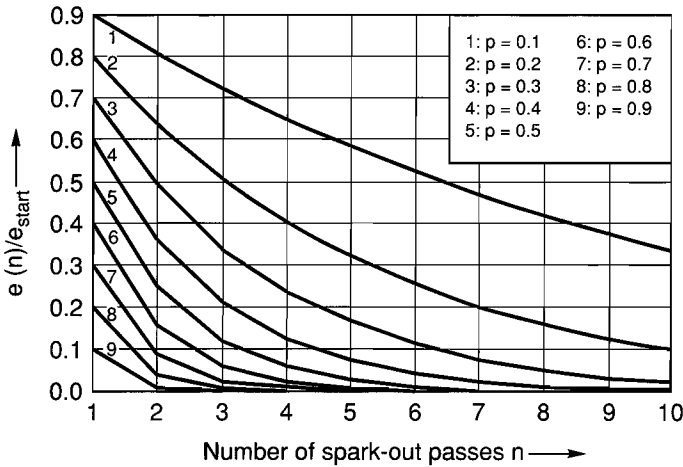


**Fig 4.35** Residual error (normalized to the initial error) after a number of spark-out passes for various  $p$  values.

To do so, the first step is to carry out grinding cuts with known infeeds (normalizing factor  $z_s$ ), until a steady state is reached.

In the steady state situation (Fig. 4.36), the ground profile is measured, so  $\tilde{e}_{lim}(x)$  can be determined. Next the factor  $p$  as a function of the  $x$ -position of the grinding wheel is derived using eq. {4.24}.

Suppose the function describing the ideal profile to be ground in the next pass is  $z_{ideal}(x)$ .

The actual depth of cut to realize this in the next pass has to be (Fig. 4.36)

$$z_a(x) = e_{lim}(x) - z_{ideal}(x) \tag{4.29}$$

The cumulative depth of cut  $z_{pc}(x)$ , needed in the next pass to accomplish this, compensating for compliance effects is given by:

$$z_{pc}(x) = \frac{z_a(x)}{p(x)} \tag{4.30}$$

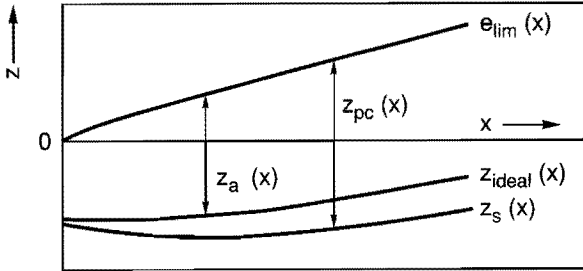


**Fig. 4.36** Steady state error  $e_{lim}(x)$ , profile  $z_{ideal}(x)$  to be cut and infeed profile  $z_s(x)$  to do so, compensating for compliance effects.

Substitution of eq. {4.24} and {4.29} gives

$$z_{pc}(x) = \frac{e_{lim}(x) - z_{ideal}(x)}{p(x)} = [e_{lim}(x) - z_{ideal}(x)] \cdot [\tilde{e}_{lim}(x) + 1] \quad \{4.31\}$$

which when written out gives four terms:

$$z_{pc}(x) = e_{lim}(x) - z_{ideal}(x) - \tilde{e}_{lim}(x) \cdot z_{ideal}(x) + e_{lim}(x) \cdot \tilde{e}_{lim}(x) \quad \{4.32\}$$

The first two "geometrical terms" can direct be seen in Fig. 4.36, the last two terms are "compliance correction terms".

In implementing this correction/prediction scheme practically, it is noteworthy that the first term  $e_{lim}(x)$  in eq. {4.32} is generated in preceding passes (see Fig. 4.36). This means that to realize the cumulative depth of cut  $z_{pc}(x)$  given by eq. {4.32}, only the last three terms of eq. {4.32} have to be included in the infeed profile for the next cut  $z_s(x)$ . Another aspect to be wary of is the sign of the terms in eq {4.31} in view of the location of axis zero-points (see Fig. 4.36) and positive coordinate directions on CNC machines.

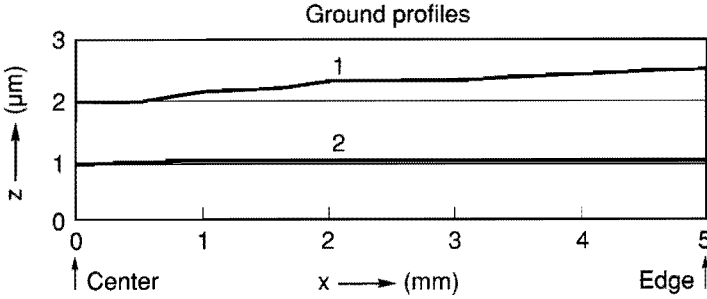


**Fig. 4.37** Profile ground with grinding wheel K+888, after 5 cuts, each 1 μm infeed (1), and after 1 additional cut with a correction applied to the infeed to correct for compliance effects (2).

The procedure described above has been used to correct the surface profile ground with the relatively soft grinding wheel K+888 in 5 successive cuts, each nominally 1 μm deep. The profile after these 5 cuts and the profile ground with a correction scheme as outlined above can be seen in Fig. 4.37.

The correction applied was based on the assumption that the profile ground after the first 5 cuts could be approximated as a second order polynomial. In that case the infeed profile necessary to grind a flat part next time around consists of a polynomial of order four (eq. {4.32}). Such a polynomial was relatively easy implemented in the CNC of the ESDO.

A more general implementation of the correction procedure described here is easily achieved by fitting other functions to the measured error profile  $\tilde{e}_{lim}(x)$  and by determining more complex corrections for the compliance effects.

An even better approach would be to determine  $p(x)$  in a non-parametric sense from experimental data (filtered so that only reproducible form errors are taken into account) and to generate a non-parametric correction profile  $z_c(x)$  that is transferred to the CNC as an array of set-points for the machine infeed profile.

A small ( $\approx 0.1 \mu\text{m}$ ) residual deviation of the corrected profile from a straight horizontal line close to the center of the part is sometimes observed in practice even after a correction cut.

This is due to the fact that the assumption that the force-displacement relation is linear is not completely true (especially close to the part center), the steady state has not been reached completely after 5 cuts, and the value of  $p(x)$  can only be determined with an accuracy which is limited by that of the on-line profile measurement ( $\approx 0.1 \mu\text{m}$ ).

The correction will therefore in practice not be perfect, and it is interesting to investigate the magnitude of the profile errors that can be expected after applying corrections in practical situations.

In the simulation program, several correction schemes were implemented to investigate the achievable accuracy that can be expected in practice, in view of how close a steady state has been approached and the non-linearity of the wheel compliance.

Simulations were carried out:

- Considering different moduli of elasticity  $E_w$ .
- Considering line- and elliptical contact situations.
- Using a correction scheme where  $\tilde{e}_{im}(x)$  was approximated by a polynomial, and using a non-parametric correction scheme.
- Performing corrections on the first and fourth simulated profile, generated by simulating successive cuts with equal infeed, to investigate the influence of how close a steady state has been approached.

Fig. 4.38 shows examples of simulated profiles. The results of the various simulations listed above can be summarized as follows:

- Assuming nominal grinding conditions, a line contact situation,  $E_w=8 \text{ GPa}$ ,  $W=1 \text{ mm}$ , and applying the correction after the steady state has been approached for 85%, the simulated residual profile error after non-parametric correction was 12 nm.
- For a comparable elliptical contact situation, the residual error is only marginally larger (15 nm).

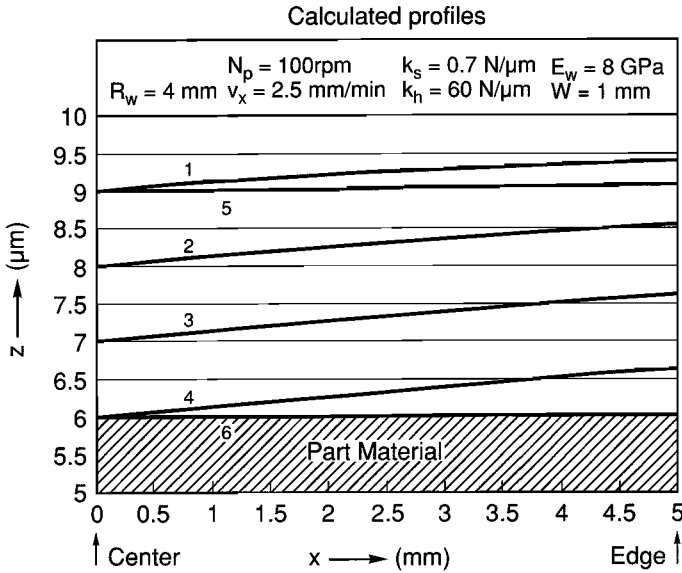


**Fig. 4.38** Profiles simulated with equal infeeds of  $1 \mu\text{m}$  (curves 1 through 4), and using the non-parametric correction scheme to correct the first and fourth profile (curves 5 and 6).

- The difference in profile errors calculated after correction with a non-parametric correction scheme compared to a polynomial scheme ( $\tilde{e}_{\text{lim}}$  fitted with second order polynomial), is also marginal.
- If the same correction is applied after the first simulated cut, where the steady state was only approached to 40%, the calculated profile error after correction is  $75 \text{ nm}$ .

The profile error  $e_{\text{lim}}$  is currently measured on the machine using a contacting inductive probe (LVDT). The accuracy of such a measurement is limited to about  $0.1 \mu\text{m}$ . Such metrology errors lead to inaccuracies in the correction terms in eq. {4.32} and limit the form accuracy that can be achieved with the correction scheme to about  $100 \text{ nm}$ . A better measurement of the part profile on the machine would enable us to improve the contour grinding accuracy further with the correction scheme proposed.



## 4.8. Conclusions.

- The form accuracy in contour grinding has been studied both experimentally and theoretically.
- After variance due to environmental effects was reduced to sub-micron level, the condition of the wheel after (re)conditioning is the major source of variance in the ground surface profiles.
- Monitoring the force signal during the dressing operation provides useful information regarding the condition of the grinding wheel.
- Once a grinding wheel has been conditioned well, its compliance behaviour is stable and repeatable, not affected significantly by wear, for quite a number of cuts, on relatively small parts.
- In view of the above conclusion, the deterministic nature of the compliance effects observed can be used to predict the profile errors that will be generated if a profile is to be ground with a particular wheel (as long as it is not reconditioned).
- For the small, high speed air bearing spindle used, in conjunction with resin bond wheels, the deflection of the grinding wheel is comparable to that of the grinding spindle.
- A stiffer grinding spindle (and the use of stiffer wheels) will enhance the form accuracy of the precision grinding operation significantly.
- A model, including relations for the most important effects observed, was built up and used to simulate the profile grinding process. Due to the uncertainty in the numerical value of some of the model parameters, the simulations yielded qualitative information only. However, the simulations were very useful to understand the relative importance of the variables and to reveal the nature of the memory effect observed in the grinding experiments.
- Especially with relatively resilient resin bond wheels, the use of varying part speed and feed rate to keep the material removal rate constant can be expected to result in more uniform profile errors.
- A quite general linear theory describing the development of the ground profile and the profile error in successive cuts has been developed.
- Based on this theory, predictions can be made about the achievable accuracy for a given combination of machine tool, grinding wheel stiffness and process variables.
- The number of spark-out passes needed to reduce a given profile error to an acceptable level can be predicted using the linear theory.

- The linear theory shows how the motion copying ability (p factor) depends on the process variables and the machine and grinding wheel compliances. This relation shows ways to improve the accuracy of the grinding operation.
- The linear theory developed makes it possible to calculate a feed forward correction to compensate for compliance effects. Especially if resilient wheels have to be used, for instance to achieve form accuracy and good surface finish at the same time, the correction schemes discussed can be used to enhance the contour accuracy significantly.
- The correction scheme presented makes contour grinding accuracy in the 10 nm range feasible.
- To reach this form accuracy in practice, as a first step, the metrology systems used on the grinding machine to measure the part profile and to control the slide motions have to be improved.

#### References for chapter 4.

Archard J.F., 1980, "Wear Theory and Mechanisms", in *Wear Control Handbook*, edited by Peterson E.D. and Winer W.O., ASME, New York, pp. 35 ev.

Blaedel K.L., 1980, "Error Reduction", Rep. Machine Tool Task Force, Vol.5, UCRL-52960-5.

Franse, J., 1990, "Manufacturing Techniques for Complex Shapes with Sub-Micron Accuracy", Rep. Prog. Phys., Vol. 53, pp. 1049-1094.

Gibbings J.C., 1986, "The Systematic Experiment", Cambridge Un. Press, Cambridge, UK.

Giridharan T., Dix R.C. and Nair S., 1986, "Wheel-Wear Compensation for Numerical Form Grinding", *Trans ASME, J. Eng. for Ind.*, Vol.108, pp. 16-21.

Greenwood J.A., Johnson K.L. and Matsubara E., 1984, "A surface roughness parameter in Hertz contact", *Wear*, Vol. 100, pp. 93 ev.

Gross W.A., Matsch L.A., Castelli V., Eshel A., Vohr J.H. and Wildmann M., 1980, "Fluid Film Lubrication", New York, Wiley.

- Halling J., 1983, "Toward a Mechanical Wear Equation", *Trans. ASME, J. Lub. Techn.*, Vol. 105, pp. 213 ev.
- Holz R. and Sauren J., 1986, "Schleiftechnisches Handbuch", published by Ernst Winter & Sohn, Hamburg, Germany.
- Johnson K.L., 1985, "Contact Mechanics", Cambridge Un. Press, Cambridge, UK.
- Kagami J., Yamada K. and Hatazawa T., 1983, "Contact between a Sphere and Rough Plates", *Wear*, Vol. 87, pp. 93 ev.
- McClure E.R., 1969, "Manufacturing Accuracy Through the Control of Thermal Effects", PhD thesis, UCRL-50636.
- Preston F.W., 1927, *Journ. Glass Technology*, Vol.11., pp. 124 ev.
- Rabinowicz E., 1965, "Friction and Wear of Materials", John Wiley, New York.
- Schellekens P.H.J., 1986, "Absolute Meetnauwkeurigheid van Technische Interferometers", PhD thesis, Techn. Un. Eindhoven, The Netherlands. (in Dutch).
- Snoeys R., and Wang I.C., 1968, *Proc. 9<sup>th</sup> Int. M.T.D.R. Conf.*, Part 2, sept. 1986, Un. of Birmingham, Birmingham, UK., pp. 1133-1148.
- Tangena A.G., 1987, "Tribology of Thin Film Systems", PhD thesis, Techn. Un. Eindhoven, The Netherlands.
- Teeuwssen J.W.C.M., 1989, "Performance Evaluation and a Quality Control System for Three Coordinate Measuring Machines", PhD thesis, Techn. Un. Eindhoven, The Netherlands.
- Thusty, J. 1972, "Grinding Machine Ability to Reduce Workpiece Form Error", in "New Developments in Grinding", edited by M.C. Shaw, Carnegie, Pittsburg Pa, USA., pp. 366-380.

Wadsworth H.M., 1990, "Statistical Methods for Engineers and Scientists", McGraw-Hill.

Zum Gahr K.H., 1983, "Reibung und Verschleiss, Mechanismen, Pruftechnik, Werkstoffeigenschaften", Deutsche Gesellschaft fur Metallkunde.

### Appendix 4.1. Geometry of the contact area.

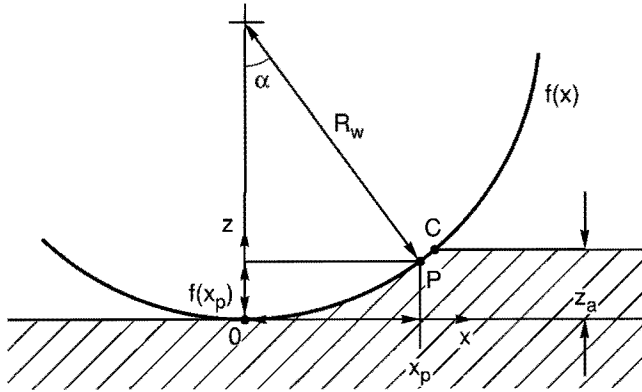


Fig. 4.39 The contact situation in precision contour grinding.

Referring to Fig. 4.39, the first step in the derivation of the expression for the (projected) immersed area  $A$  as a function of the radius of the grinding wheel  $R_w$ , the feed rate  $f$  and the cutting depth  $z_a$  is to describe the immersed arc segment denoted by  $OC$ .

Taking  $O$  as origin of the cartesian coordinates  $x$  and  $z$ , bearing in mind that  $R_w \gg z_a$  and so  $\sin(\alpha) \approx \alpha$  it follows from the geometry of Fig. 4.39 that

$$\sin(\alpha) = \frac{x}{R_w} \approx \alpha \quad \{\text{A4.1.1}\}$$

$$f(x) = R_w \cdot \left( 1 - \cos\left(\frac{x}{R_w}\right) \right) \quad \{\text{A4.1.2}\}$$

and by substitution of the Taylor's series approximation for  $\cos(\alpha)$

$$\cos(\alpha) \approx 1 - \frac{\alpha^2}{2!} + \dots \quad \{\text{A4.1.3}\}$$

the so-called parabolic approximation for the arc segment OC is found:

$$f(x) = \frac{x^2}{2 \cdot R_w} \quad \{A4.1.4\}$$

The immersed area A at an arbitrary point in time is now determined as the area bounded by (Fig. 4.13):

- The curve  $f(x)$ . This curve describes the position of the cutting edge in the former revolution of the part with respect to the origin O which is located as indicated in Fig. 4.13. The maximum cutting depth is  $z_a$ .
- The curve  $g(x)$ , which describes the immersed arc at this particular time with respect to the origin O chosen.
- The part surface.

These curves are described by:

$$f(x) = \frac{x^2}{2 \cdot R_w} \quad \{A4.1.5\}$$

$$g(x) = \frac{(x-f)^2}{2 \cdot R_w} \quad \{A4.1.6\}$$

$$\text{Part surface} : z = z_a \quad \{A4.1.7\}$$

The total area A is the sum of the areas BCE and CDE in Fig. 4.13. To evaluate these areas by definite integration of the appropriate describing functions, it is necessary to find expressions for the x coordinates of the points B, C, and D to establish the integration boundaries.

$$B : f(x) = g(x) \rightarrow x_B = \frac{f}{2} \quad \{A4.1.8\}$$

$$C : f(x) = z_a \rightarrow x_C = \sqrt{2 \cdot R_w \cdot z_a} \quad \{A4.1.9\}$$

$$D : g(x) = z_a \rightarrow x_D = f + \sqrt{2 \cdot R_w \cdot z_a} \quad \{A4.1.10\}$$

The areas BCE and CDE can now be determined as

$$\text{Area BCE} = \int_{x_B}^{x_C} [f(x) - g(x)] \cdot dx \quad \{\text{A4.1.11}\}$$

$$\text{Area CDE} = \int_{x_C - x_B}^{x_D} [z_a - g(x)] \cdot dx \quad \{\text{A4.1.12}\}$$

The evaluation of these integrals is straightforward, and the final result is

$$A = f \cdot z_a - \frac{f^3}{24 \cdot R_w} \quad \{\text{A4.1.13}\}$$

Equation {A4.1.13} is valid until the feed rate  $f$  becomes so high or  $z_a$  is so small that no more overlap between the arc segments OC and AD occurs. This condition (region where {A4.1.13} is valid) can be stated as

$$f \leq 2 \cdot \sqrt{2 \cdot R_w \cdot z_a} \quad \{\text{A4.1.14}\}$$

In case  $f$  falls outside this region the immersed area is independent of  $f$ :

$$A = \frac{4}{3} \cdot z_a \cdot \sqrt{2 \cdot R_w \cdot z_a} \quad \{\text{A4.1.15}\}$$

## Appendix 4.2. Summary of variables and equations used in simulations and linear process model.

### *List of variables used.*

- A : Immersed area, also called interfering section ( $\text{mm}^2$ ).
- C : Constant used in Preston's equation.
- $C_2$  : Constant used in the linear approximation of the force-compliance relation.
- $dV/dt$  : Material removal rate ( $\text{mm}^3/\text{s}$ ).
- e : Profile error (residue).
- $e_{\text{lim}}$  : Limit value of the profile error.
- $E_w$  : Modulus of elasticity of the grinding wheel.
- f : Feed-rate in mm/part rev.
- F : Grinding force.
- $F_{\text{max}}$  : Maximum value of grinding force during a cut.
- H : Hardness of the part.
- i : Integer, used to index discrete x values.
- k : Integer, used to indicate a particular cut number.
- $k_h$  : Stiffness of headstock spindle (in z-direction).
- $k_s$  : Stiffness of grinding spindle (at center height, in z-direction).
- n : Integer, used as counter (spark-out cuts for instance).
- $N_p$  : Part speed (rpm).
- $N_w$  : Wheel speed (rpm).
- p : Ratio of actual and cumulative cutting depth  $z_w/z_{pc}$  ( $0 < p < 1$ ).
- $R_p$  : Radius of the cylindrical part. (Distance from center to edge).
- $R_w$  : Grinding wheel radius in x-z plane.
- $R_y$  : Grinding wheel radius in y-z plane (elliptical contact situation).
- $u_m$  : Machine displacement due to compliance.
- $u_w$  : Grinding wheel deflection.
- $u_t$  : Total (machine + grinding wheel) displacement due to compliance.
- $v_t$  : Tangential part speed (at any x position).
- $v_w$  : Cutting speed (speed of cutting edge).
- $v_x$  : Feed-rate (speed of x-slide).
- W : Contact width in y direction, for a line contact situation.
- z : Profile height, machine coordinate.



- $z_a$  : Actual depth of cut.  
 $z_{ac}$  : Cumulative actual depth of cut.  
 $z_{ideal}$  : Desired profile.  
 $z_s$  : Infeed of machine slide in z-direction.  
 $z_{sc}$  : Cumulative machine infeed.  
 $z_{pc}$  : Cumulative depth of cut (as experienced by the material).  
 $\nu$  : Poisson's ratio of the grinding wheel.

*Set of equations used in the simulations.*

The variables  $R_w$ ,  $W$ ,  $R_p$ ,  $v_x$ ,  $E_w$ ,  $\nu$ ,  $H$ ,  $C$ ,  $k_s$ ,  $k_b$ ,  $N_p$ ,  $N_w$ , and  $R_p$  and the infeed profiles  $z_i(k,x)$  for the cutting sequence are specified as input for the simulation.

Referring to Fig. 4.1, discrete positions  $x_i$  are considered, spaced a distance  $f$  apart.

$$f = \frac{60 \cdot v_x}{N_p} \quad \{\text{A4.2.1}\}$$

The wheel speed (cutting speed) is

$$v_w = \frac{2 \cdot \pi \cdot N_w \cdot R_w}{60} \quad \{\text{A4.2.2}\}$$

The set of equations considered simultaneous for each cut  $k$  and  $x$  position  $x_i$  in the non-linear simulation consists of the following equations:

The infeed during any pass number  $k$  at  $x$  position  $x_i$  is given as  $z_i(k,x_i)$  and the cumulative infeed is

$$z_{sc}(k,x_i) = \sum_{n=1}^k z_s(n,x_i) \quad \{\text{A4.2.3}\}$$

The cumulative depth of cut (experienced by the material) is

$$z_{pc}(k,x_i) = z_{sc}(k,x_i) - \sum_{n=1}^{k-1} z_o(n,x_i) \quad \{\text{A4.2.4}\}$$

The machine displacement (due to the grinding force)  $u_m(k,x_i)$  is given by

$$u_m(k, x_i) = \frac{F(k, x_i)}{k_h} + \frac{F(k, x_i)}{k_s} \quad \{A4.2.5\}$$

The wheel deflection due to the cutting force  $u_w(k, x_i)$  is given by

$$\text{a : } \begin{cases} u_w(k, x_i) = \frac{2 \cdot F(k, x_i) \cdot (1-v^2)}{\pi \cdot E_w \cdot W} \cdot \left[ \ln \left( \frac{2 \cdot R_w}{a(k, x_i)} \right) - \frac{v}{2 \cdot (1-v)} \right] \\ a(k, x_i) = 2 \cdot \sqrt{\frac{R_w \cdot F(k, x_i) \cdot (1-v^2)}{\pi \cdot E_w \cdot W}} \end{cases} \quad \{A4.2.6\}$$

$$\text{b : } u_w(k, x_i) = \left( \frac{9 \cdot F(k, x_i)^2}{16 \cdot \sqrt{R_w \cdot R_y}} \right)^{1/3} \cdot \left( \frac{1-v^2}{E_w} \right)^{2/3}$$

depending on whether a line contact (eq. {4.2.6 (a)}) or an elliptical contact situation (eq. {4.2.6 (b)}) is considered.

The total displacement of the structural loop  $u_i(k, x_i)$  is calculated as

$$u_i(k, x_i) = u_w(k, x_i) + u_m(k, x_i) \quad \{A4.2.7\}$$

The immersed area  $A$  is given by

$$A(k, x_i) = f \cdot z_a(k, x_i) = \frac{f^3}{24 \cdot R_w} \quad \{A4.2.8\}$$

The tangential part speed  $v_t$  at position  $x_i$  is

$$v_t(k, x_i) = \frac{2 \cdot \pi \cdot N_p \cdot x_i}{60} \quad \{A4.2.9\}$$

The grinding force  $F(k, x_i)$  is calculated using the wear equation {4.11}

$$F(k, x_i) = \frac{H \cdot A(k, x_i) \cdot v_t(k, x_i)}{C \cdot v_w} \quad \{A4.2.10\}$$

the actual depth of cut  $z_a(k, x_i)$  is

$$z_a(k, x_i) - z_{pc}(k, x_i) - u_i(k, x_i) \quad \{A4.2.11\}$$

After these equations are solved for  $F(k, x_i)$ ,  $A(k, x_i)$ ,  $u_i(k, x_i)$  and  $z_a(k, x_i)$ , the profile height  $z(k, x_i)$  is found from

$$z(k, x_i) - z(k-1, x_i) - z_a(k, x_i) \quad \{A4.2.12\}$$

### *Equations for the linear model.*

Since the following discussion is quite general in the sense that the cut number  $k$  is irrelevant and  $x$  is considered as a continuous variable, the indices  $(k, x_i)$  are omitted.

From the considerations in section 4.6.1 regarding the force-deflection relation of grinding wheels, it has become apparent that the non-linearities in these relations are small. Equations {A4.2.5}, {A4.2.6} and {A4.2.7} are therefore replaced by

$$u_i = C_2 \cdot F \quad \{A4.2.13\}$$

Practical values for  $C_2$  can be estimated from the force-total compliance relation.  $C_2$  typically assumes values around  $1 \mu\text{m}/\text{N}$  for the combination of resin bond wheels and the stiffness of the machine components used in this study.

The non-linear term in eq. {A4.2.8} is also neglected. This can be justified by looking at the order of magnitude of  $f$  ( $1 \mu\text{m}$ ),  $z_a$  ( $1 \mu\text{m}$ ) and  $R_w$  (order  $1000 \mu\text{m}$ ). The first term will thus always be an order of  $10^4$  larger than the second.

$$A = f \cdot z_a \quad \{A4.2.14\}$$

Other than these, the set of equations remains the same. From {A4.2.11} and {A4.2.13} follows

$$z_a = z_{pc} - C_2 \cdot F - z_{pc} \cdot \left( 1 - \frac{C_2 \cdot F}{z_{pc}} \right) \quad \{A4.2.15\}$$

which can be reformulated as

$$z_a = P \cdot z_{pc} \quad \{A4.2.16\}$$

and  $p$  is a crucial factor in the applications of the linear theory. The numerical value of  $p$  can be determined from simple experiments, and this takes into account the parameters that are otherwise difficult to determine ( $C$  and  $C_2$ ).

It is interesting to see how  $p$  depends on these quantities and the controlled parameters, since this shows how the process may be optimized.

The first step is to replace  $A$  in eq. {A4.2.10} by

$$A = f z_a - f(z_{pc} - u_i) - f(z_{pc} - C_2 \cdot F) \quad \{A4.2.17\}$$

and to substitute {4.2.2} and {4.2.9} in {4.2.10} so that the following expression for  $F$  is found

$$F = \frac{f(z_{pc} - C_2 \cdot F) \cdot N_p \cdot x \cdot H}{N_w \cdot R_w \cdot C} \quad \{A4.2.18\}$$

rearranging eq. {A4.2.18} gives

$$F = \frac{f z_{pc} \cdot N_p \cdot x \cdot H}{N_w \cdot R_w \cdot C + f \cdot C_2 \cdot N_p \cdot x \cdot H} \quad \{A4.2.19\}$$

combining eq. {4.2.19} with {A4.2.15} and {A4.2.16} and solving for  $p$  gives the relation between  $p$  (the motion copying ability) and the process variables:

$$p = 1 - \frac{C_2 \cdot f \cdot N_p \cdot x \cdot H}{N_w \cdot R_w \cdot C + C_2 \cdot f \cdot N_p \cdot x \cdot H} = \frac{N_w \cdot R_w \cdot C}{N_w \cdot R_w \cdot C + C_2 \cdot f \cdot N_p \cdot x \cdot H} \quad \{A4.2.20\}$$

For values of  $p$  close to 1,  $p$  becomes practically linear in  $x$  and the expression for  $p$  can be simplified further to

$$p = \frac{1}{1 + q \cdot x} = 1 - q \cdot x \quad \{A4.2.21\}$$

where  $q$  is also a suitable number to indicate the process quality, since it only depends on the machine, the process variables and the part material, not on the part size.

$$q = \frac{C_2 \cdot f \cdot N_p \cdot H}{N_w \cdot R_w \cdot C} \quad \{A4.2.22\}$$

**Curriculum****Vitae**

- 12 Jan 1958 : Geboren te Djakarta.
- 1964-1970 : Jan Campertschool te Driehuis (NH).
- 1970-1976 : Vissering Scholengemeenschap te IJmuiden (Atheneum)  
(Diploma 1976).
- 1976-1984 : Technische Universiteit Delft, afd. Metaalkunde  
(Ir. diploma 1984).
- 1984-1987 : Wetenschappelijk medewerker bij Philips Natuurkundig  
Laboratorium te Eindhoven, groep Mechanica, Tribologie en  
Systeem- en Regeltechniek.
- 1987-1988 : Als wetenschappelijk medewerker in dienst van Philips  
International uitgezonden naar Lawrence Livermore  
National Laboratory, California, USA.
- 1988-heden : Wetenschappelijk medewerker bij Philips Natuurkundig  
Laboratorium te Eindhoven, groep Mechanica, Tribologie en  
Systeem- en Regeltechniek.

---

## Dankwoord.

Deze thesis is het resultaat van bijna vier jaar intensieve samenwerking.

Met Gerrit Jan de Jong, die de ESDO opbouwde, die vele proeven voor en met mij uitvoerde, en mee (en tegen) worstelde bij de interpretatie.

Met Cor Roelandse, die de ESDO klimatiseerde en meedacht over betere instrumentatie en de volgende generatie slijpspindels.

Met Johan Wijn, Cor Naus, Jo Oomen, Wichert Mesman en al die andere vaklieden in de bedrijfsdienst die hielpen bij het vervaardigen van opstellingen, het uitvoeren van experimenten en het maken en meten van sub-microns.

Met Ton Tangena, op het gebied van de fundamentele wrijvings en slijtage-aspecten van het onderzoek en eindige elementen berekeningen.

Met Henk van Dijk en Evert Jan Donkelaar, tijdens de indrukproeven en het onderzoek naar de invloed van het milieu op het scheurgedrag van glas.

Met Joost Versteijlen en Herman van der Kall, op het gebied van de dynamica van precisie-verspaningsmachines.

Met Willem Potze, die meedacht over simulaties, limieten van rijen en reeksen en andere wiskundige aspecten van hoofdstuk 4.

Voor het bereikte resultaat was ook van belang de samenwerking met mensen van andere instituten, zoals met Jeff Roblee (LLNL), tijdens mijn verblijf bij Lawrence Livermore National Laboratories en speciaal bij het werk aan de dynamica van machines en het ontwerp van de couveuse voor de ESDO.

Met Ken Blaedel (LLNL), tijdens de modelvorming van de bros-ductiel overgang middels breuk-mechanica.

Met de vele HTS afstudeerders die elk een deel van de software voor hun rekening namen waarmee de ruwheid van geslepen oppervlakken gekarakteriseerd kon worden.

Met Monique, die de condities schiep die het mogelijk maakten aan deze thesis te werken zonder al mijn vrienden en kennissen kwijt te raken. Die aanvaardde dat ik geen huis schilderde, gras maaide en al wat dies meer zij. Die haar leven voor mij ontregelde om met mij naar de USA te gaan.

Die mij aanmoedigde door te gaan, telkens weer, ook als een veelbelovend stuk theorie na enig experimenteren gefalsificeerd werd en ik terug moest naar af.

Al deze mensen wil ik bedanken voor hun bijdragen en hun inzet.

Stellingen  
behorende bij het proefschrift

**Aspects of Precision Grinding**

van  
Jelm Franse

1. **Onderzoek van aspecten van precisie bewerkingsmethoden, met als doel de bewerkingsnauwkeurigheid te verhogen, heeft pas zin na een grondige analyse van het totale systeem.**  
*Dit proefschrift, hoofdstuk 1.*
2. **Aan de hand van ruwheidsparameters, gebaseerd op statistische kentallen welke de totale informatie in een ruwheidsprofiel in enkele getallen weergeven, zijn precies geslepen oppervlakken moeilijk te beoordelen.**  
*Whitehouse D.J., 1978, Proc. Inst. Mech. Eng., Vol. 15, No.1, pp. 179-188.*  
*Dit proefschrift, hoofdstuk 2.*
3. **Eindige elementen berekeningen vormen een betere basis dan analytische modellen, voor het bepalen van spanningsprofielen en spannings-intensiteitsfactoren om het scheurgedrag van glas bij indrukproeven te voorspellen.**  
*Chiang S.S., Marshall D.B. and Evans A.G., 1982, J. Appl. Phys., Vol.53, pp. 298-317.*  
*Dit proefschrift, hoofdstuk 3.*
4. **Om het optreden van scheurvorming in glas bij het slijpen te voorspellen, dient de interactie tussen residuele spanningsvelden om opeenvolgende krassen, gemaakt door verschillende slijpkorrels, in rekening gebracht te worden.**  
*Dit proefschrift, hoofdstuk 3.*
5. **De snijsnelheid van slijpkorrels in glas beïnvloedt de kritische belasting voor scheurvorming nauwelijks, zolang thermische effecten geen drastische veranderingen van het materiaalgedrag veroorzaken.**
6. **Vergeleken met proeven in water-arme milieus, worden scheurverschijnselen in glas versneld in waterige milieus. Het is raadzaam slijpproeven waarbij geen scheurvorming achteraf mag optreden uit te voeren in waterige milieus.**  
*Inagaki M., Urishima K. et. al., 1985, J. Am. Cer. Soc., Vol. 68, pp. 704-706.*  
*Dit proefschrift, hoofdstuk 3.*
7. **Methoden voor proef opzetten die in massafabricage en kwaliteitscontrole worden toegepast zijn minder geschikt bij het precisie verspanen, waar het gaat om het verkrijgen van modelkennis om foutenbronnen te identificeren en te elimineren.**  
*Wadsworth H.M., 1990, "Statistical Methods for Engineers and Scientists", McGraw-Hill.*  
*Dit proefschrift, hoofdstuk 4.*



8. De discussie tussen specialisten op het gebied van slijpen en polijsten over "kracht gesloten bewerkingen" versus "weggestuurde processen" kan afgesloten worden.  
*Dit proefschrift, hoofdstuk 4.*
9. Veel discussies over "fundamentele verschillen" tussen bewerkingsmachines en processen zijn het gevolg van onvoldoende systeem overzicht en het uit z'n (systeem)verband beschouwen van slechts enkele aspecten.  
*Dit proefschrift, hoofdstuk 4.*
10. De éénwording van Europa zal resulteren in een grotere uniformiteit van produkten, diensten en uiteindelijk cultuurpatronen. Verder zijn uitgebreide regelgeving, bureaucratie en gevoelens van onmacht bij bewoners van kleine naties te voorzien.
11. Als reactie op de europese éénwording zullen in de volgende eeuw fenomenen als individualisering, nostalgie, traditie, ceremonie en nationalisme belangrijker worden.
12. Eénzijdige invoering van een snelheidsbegrenzer in nederlandse auto's is vergelijkbaar met het wetmatig beperken van de maximale rekensnelheid van computers. In beide gevallen zou de vaart uit de nederlandse economie gehaald worden.
13. Zolang in sommige delen van de wereld het moedwillig veroorzaken van milieurampen tot de heldendaden wordt gerekend is het bedenken van "groene" stellingen door nederlandse promovendi zinloos.
14. Als het maken van kinderen net zoveel kennis en technologie zou vergen als het vervaardigen van zelfs eenvoudige robots zou overbevolking een minder groot probleem zijn.
15. Een overeenkomst tussen technische specialisten en tweejarige meisjes is hun taalgebruik; voor niet-intimi zijn ze net zo onbegrijpelijk. Een verschil tussen beide categorieën is dat alleen bij kleine meisjes kennisgroei gepaard gaat met beter taalgebruik.
16. Bij zwangere vrouwen en promovendi is vaak een zekere mate van absentie waarneembaar. In beide gevallen gaat het na de bevalling beter.